Investigation of novel advanced ceramic materials having hydrogen affinity based on in-situ local structural analyses

In-situ 局所構造解析に基づく新規セラミック系
水素親和性材料の創製

Shotaro Tada

Nagoya Institute of Technology

2021

Table of Contents

Chapter 1 Introduction

Chapter 2 Low temperature in-situ formation of cobalt in silicon nitride toward functional nitride nanocomposites

Chapter 3 Hydrogen transport property of polymer-derived cobalt-doped amorphous silica

Chapter 4 Reversible Redox Property of Co(III) in Amorphous Co-doped SiO_2/γ-Al_2O_3 Layered Composites

Chapter 5 Novel hydrogen chemisorption properties of amorphous ceramic compounds consisting of p-block elements: exploring Lewis acid-base Al–N pair site formed in-situ within polymer-derived silicon-aluminum-nitrogen-based system

Chapter 1

Introduction

1.1 Motivation

Nowadays, production and usage of fossil fuels is continuously increasing and is changing the Earth's climate: the concentration of CO_2 reached approximately 420 parts per million (ppm) in 2020 (Fig. 1-1) [1], and this increase would result in a global temperature rise of at least 2°C of pre-industrial levels by 2100 [2]. As the average temperatures rise, natural disasters like forest fires and floods grow in frequency and become enormous. In addition, the impacts of climate change in some case—such as melting glacier—are irreversible. Therefore, many countries promote a vision of "Carbon Neutrality" which is one of sustainable development goals (SDGs) [3] adopted by all United Nations Member States in 2015. The world's commitment to get net zero emissions requires us a significant development in technology.

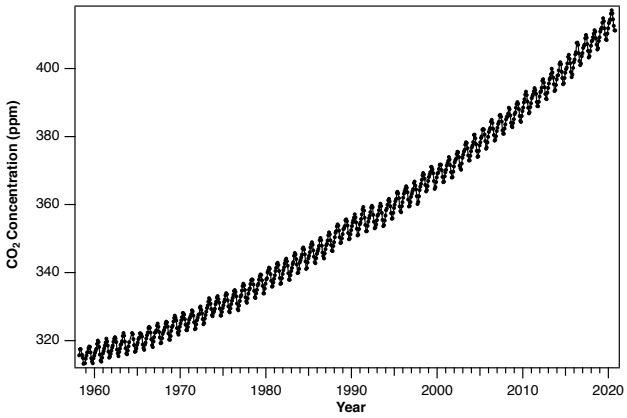

Fig.1-1 Monthly average CO_2 concentration observed at Mauna Loa, Hawaii [1].

One possible goal for our sustainable development using remaining natural resources is that establishment of hydrogen-based society. Hydrogen atom (H) is the simplest element on earth, and it is an efficient energy carrier: hydrogen molecule (H_2) can be used in fuel cells to generate electric power via chemical reactions, producing only water and heat as byproducts—H_2 is recognized as a CO_2 emission-free clean fuel.

Currently, H_2 is industrially produced by steam-reforming of fossil fuels such as natural gas and naphtha, for instance, methane (CH_4, main constituent of natural gas) is converted to

H_2 and carbon monoxide (CO) through this method,

$$CH_4 + H_2O \rightarrow 3H_2 + CO \quad (\Delta E = -206 \text{ kJ mol}^{-1}) \qquad (1\text{-}1)$$

This reaction is endothermic, so that the steam-reforming reaction is performed at high temperature, approximately 800 ˚C. The synthesis gas then proceeds to a CO shift reaction which can convert steam and CO into more H_2 and carbon dioxide (CO_2).

$$CO + H_2O \rightarrow CO_2 + H_2 \qquad (1\text{-}2)$$

Finally, high purity H_2 can be extracted from the syngas mixture through the Pressure Swing Adsorption (PSA) process.

Recently, many researchers have dedicated their efforts to develop novel materials for establishing environmental-friendly hydrogen production methods which are expected to replace the current one from fossil fuels, typically via solar water splitting [4,5]. Moreover, materials discovery is also one of key elements to realize the innovative energy conversion, transmission and storage processes for hydrogen-based fuels [2]. In this regard, hydrogen separation and purification technologies are becoming more and more important in the novel hydrogen energy cycle, for example, to establish highly efficient processes for dehydrogenation/hydrogenation of chemical hydrides such as methylcyclohexane/toluene [4–7].

Apart from the variety of applications and their importance, one of the most interesting subjects in the field of materials chemistry is that the chemical interaction with molecular H_2. The chemical interactions between material's surface and H_2 cover fundamental surface phenomena such as adsorption, diffusion, transformation, and desorption. The chemical process of H_2 dissociative adsorption is essentially challenging due to its high dissociation energy of approximately 432 kJ mol^{-1}—only available at high temperatures [8]. If the activation energy barrier is lower than the barrier of the non-catalytic pathway, then significant enhancement in the reaction rate is achievable. In addition, the materials which can easily dissociate H_2 is also able to proceed other difficult chemical reactions—via the bond activation such as σ-C–H and σ-Si–H [9, 10]—at ambient conditions. This provides us a motivation for developing novel materials which have well-controlled local structures for H_2 dissociation and adsorption.

In the field of materials science, an amorphous solid is defined as a solid that is the absence

of long-range order—which is found in crystalline solids. Thus, the properties of the material in the amorphous state—mechanical, thermal, electrical as macroscopic scale—is generally independent of the direction (isotropic). On the other hand, the amorphous solid possesses short-range order—that is, regularity in the position of neighboring atoms (at the atomic length scale) due to the nature of chemical bonding. The short-range order is also characteristic of liquids. However, there is rapid exchange of positions between the neighboring atoms; this exchange decreases as the viscosity of the liquid increases. For this reason, amorphous solids can be regarded as liquids with very high viscosity [11]. The amorphous solid at a high temperature results in the decrease of their viscosity, then it acquires the long-range order due to the structural relaxation and phase separation (crystallization), i.e., the amorphous solid is metastable state. Furthermore, the surface and interfacial effects distort the atomic positions (decreasing the structural order), thus, these sites can interact with other atoms which composing substances such as metal nanoparticles and gas molecules.

In these regards, these properties give us insights as follows: (i) local structural design of amorphous solids at the atomic scale is attractive for developing novel functional materials, (ii) the surface or interfacial sites in the amorphous solids are effective for gas adsorption and dissociation. In this thesis, various Si-based amorphous ceramic materials were synthesized based on molecular precursor approach then were investigated the relationships between their local structures and hydrogen affinity identified by in-situ local structural analyses aiming to develop novel functional materials for the hydrogen energy cycles.

1.2 The basis of "hydrogen affinity"

Before jumping into the particular research, it is worthwhile introducing the concepts and basis that underlie the "hydrogen affinity" of the materials.

1.2.1 Homolytic hydrogen dissociation on transition or noble metals

As mentioned above, the adsorption and subsequent dissociation of H_2 molecule is a critical step for utilizing into an important chemical process (e.g., catalytic hydrogenation) due to its high activation energy. The activation steps and the types of dissociated H species—atomic H, proton (H^+) and hydride ion (H^-)— also have an influence on the selectivity in the hydrogenation reactions. For example, the H^+/H^- pairs preferentially reduce the polar bond rather than the nonpolar one [12].

For decades, the H_2 adsorption and dissociation process has been performed on transition

metals (TMs) or noble metals (NMs) such as Pt, Pd and Rh [12] because of their electronic properties which allow H_2 to easily adsorb and dissociate onto the metallic surface: such the metals have partially occupied *d*-orbitals, which can accept σ electrons of H_2 (σ-donation), while donating the *d*-electrons to σ^* antibonding orbital of H_2 (Back-donation). Consequently, the H–H bond is weakened and cleaved, forming two M–H bonds (M = TM or NM metal)—the so called homolytic dissociation of H_2 (Fig.1-2). This process is analogous to oxidative addition of H_2—by forming two M–H bonds, the oxidation state of metal is raised by two—requiring the donation of *d*-elections of metals to H_2. Therefore, a high electron density of active metal sites is preferential for hydrogenation reaction.

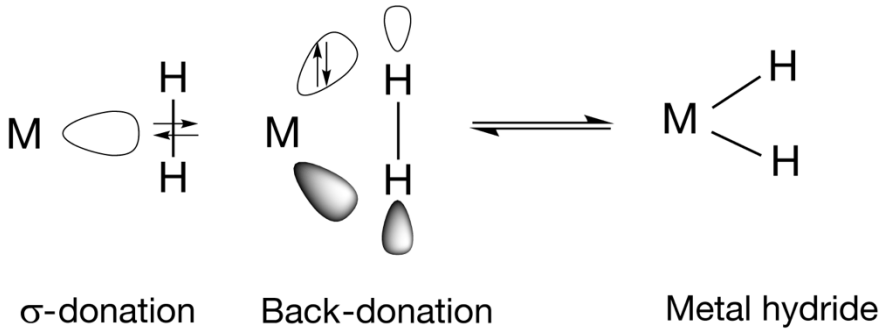

Fig. 1-2 Homolysis of H_2 molecule on a d-block metals (TM or NM).

1.2.2 Heterolytic hydrogen dissociation on supported metals [12]

Molecular H_2 can also be heterolytically dissociated into H^- and H^+ assisted by nucleophilic atoms or in strong electric field, which then binds to metal and proton acceptor (e.g., N atom), respectively. As mentioned above, a high electron density is required for the homolytic dissociation of H_2 on metals. At the metal–support interface, in contrast, the metal atoms are generally electron deficient which bonded to ligand atoms such as O and N atoms.

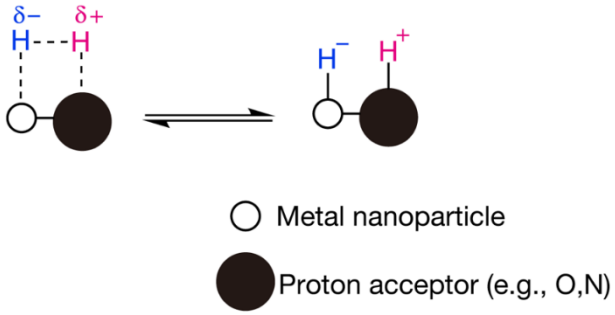

Fig.1-3 Schematic representation of heterolysis of H_2 molecule on proton acceptor supporting metal nanoparticle which serve as hydride ion acceptor.

Therefore, they are more favorable to cleave the H_2 in a heterolytic manner. The heterolytic dissociation of H_2 requires the contribution of support or additive/promoter— the electropositive d-block metals (TMs or NMs) serve as the H^- ion acceptor, while the electronegative heteroatom (X) from the support or promoter as H^+ ion acceptor (Fig.1-3).

1.2.3 Hydrogen dissociation on inorganic compounds consisting of p-block elements

Apart from the d-block metals, the H_2 dissociation and adsorption on nonmetallic materials across Lewis acidic boron and Lewis basic phosphorous sites was discovered in 2006 [11]. Lewis acid and Lewis base pair can form a dative bond, namely, Lewis acid-base adduct (Fig. 1-4a). The dative bond is generally inactive component for H_2 activation. In contrast, a system called "Frustrated Lewis Pair (FLP)" that derived from a simple combination of electron donor and acceptor but is precluded the Lewis acid-base adduct by the steric demands can heterolytically dissociates a H_2 molecule at ambient temperature (Fig. 1-4b) [14]. According to the theoretical study on the PR_3 / $B(C_6F_5)_3$ pair (R = *t*Bu and $C_6H_2Me_3$) [15], the reaction between the FLP and H_2 starts via the polarization of a H_2 molecule induced by coordination of a H_2 molecule along the B–P axis between the PR_3 and $B(C_6F_5)_3$. Molecular H_2 polarization along the FLP occurs in the direction of P→B ($P\cdots H^{\delta+}\cdots H^{\delta-}\cdots B$). The binary polarization effect acts associated with reduction of the repulsion forces on both sides of the H_2 molecule. The electron transfer occurs through simultaneous P→$\sigma^*(H_2)$ and $\sigma(H_2)$→B donation in a push-pull manner and implies a progressive weakening of the H–H bond and following heterolytic H_2 dissociation into proton (H^+) and hydride ion (H^-) (Fig. 1-4b).

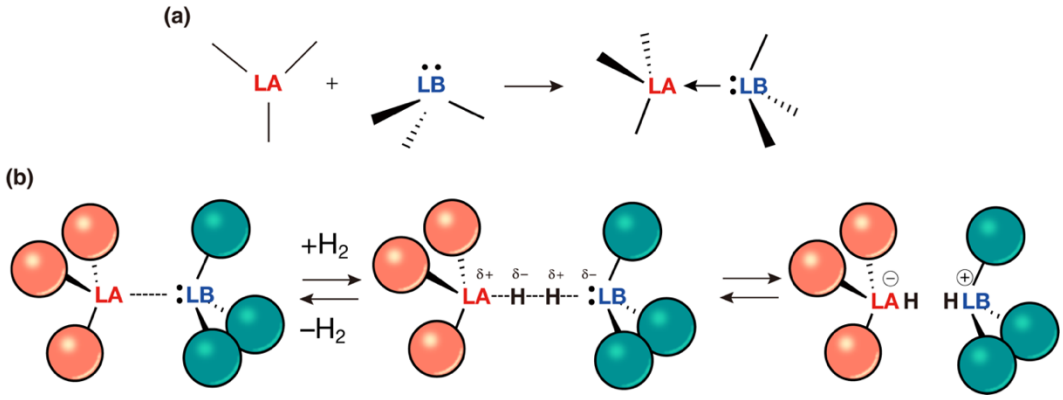

Fig. 1-4 Schematic illustration of (a) a dative bond formation between a Lewis acid-base pair, and (b) reversible H_2 dissociative adsorption on a Frustrated Lewis Pair.

1.3 Ceramics processing through polymer-derived ceramics (PDCs) route

A ceramic processing route based on molecular engineering and precursor approach called polymer-derived ceramics (PDCs) route allows to control the chemical composition of the Si-based ceramics as well as their phase distribution and nanostructure [16, 17]: typically, a polymeric precursor is liquid or meltable solid having a backbone of Si–C–Si, Si–O–Si, or Si–N–Si with cross-linkable functional groups (e.g., Si–H, Si–OH, Si–NH and Si-vinyl group). Therefore, the PDCs route is free-forming and can produce a wide variety of ceramic material which is not only binary SiC and Si_3N_4, but also ternary SiOC, SiCN via polymer-to-ceramic conversion of such the Si-based polymers (Fig. 1-5a). In addition, a chemical modification of preceramic polymer with metal or nonmetallic compounds (Fig. 1-5b) gives a quaternary system such as SiMCN (M = metal or non-metallic element such as B). The ternary SiCN or quaternary system such as SiBCN exhibits excellent thermo-mechanical properties with respect to creep and oxidation, crystallization or phase separation resistance [18]. In addition, this molecular approach offers novel functional properties such as catalytic properties of materials which have been recently highlighted in metal/Si-based (oxy)carbonitride matrix composites such as M/SiC [19], M/SiOC[20], M/SiCN[20-29] derived from metal modified polycarbosilanes, polysiloxianes, and polysilazanes, respectively.

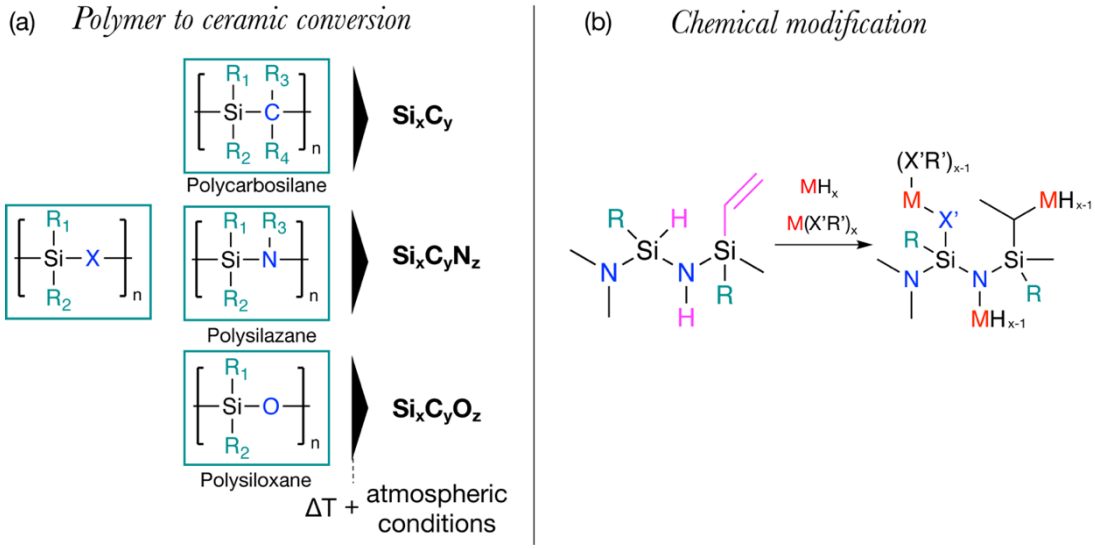

Fig. 1-5 General representation of (a) polymer to ceramic conversion process from Si-based polymers and (b) chemical modification of Si-based polymer incorporating M elements.

1.4 Outline of the thesis

Chapter 1 describes motivation, a brief introduction of hydrogen affinity in material chemistry, and a ceramic processing method through PDCs route. Figure 1-6 describes flowcharts of material synthesis via the novel PDCs routes investigated in this thesis and conventional sol-gel route and outline of this thesis.

In Chapter 2, Co nanocrystallites embedded Si_3N_4 composite system has been designed aiming to develop novel hydrogenation catalyst and synthesized from Co-coordinated polysilazane (PSZ). A unique mechanism for low temperature in-situ formation of Co nanocrystallites has been proposed and discussed.

In Chapter 3, Co(II) cation-doped amorphous silica materials with Co/Si atomic ratios ranging from 0.01 to 0.18 have been synthesized from the Co-modified PHPS with a certain amount of Si–O–Co bonds. Then, the hydrogen transport property of Co-doped silica has been discussed from a viewpoint to develop highly efficient ceramic membranes for high-temperature separation of hydrogen.

In Chapter 4, Co(II/III)-doped amorphous silica/γ-Al_2O_3 layered composites have been synthesized through a conventional sol-gel method. The use of H_2O_2 as an acid catalyst in the sol-gel process proceeded Fenton reaction which resulted in the partial formation of Co(III) within the sol gel-derived SiO_2/γ-Al_2O_3 layered composites. A unique reversible reducing and oxidizing (redox) property of the Co(II/III) in the layered composites has been discussed based on the result obtained by several in-situ characterizations on the oxidation state of the Co cations during cyclic hydrogen/argon heat treatments at 300 to 500 ºC. Moreover, a novel H_2-triggered chemical valve property of the layered composite membranes has been discussed.

Then, we demonstrate novel hydrogen chemisorption properties of amorphous ceramic compounds consisting of p-block elements namely silicon, aluminum and nitrogen elements in Chapter 5.

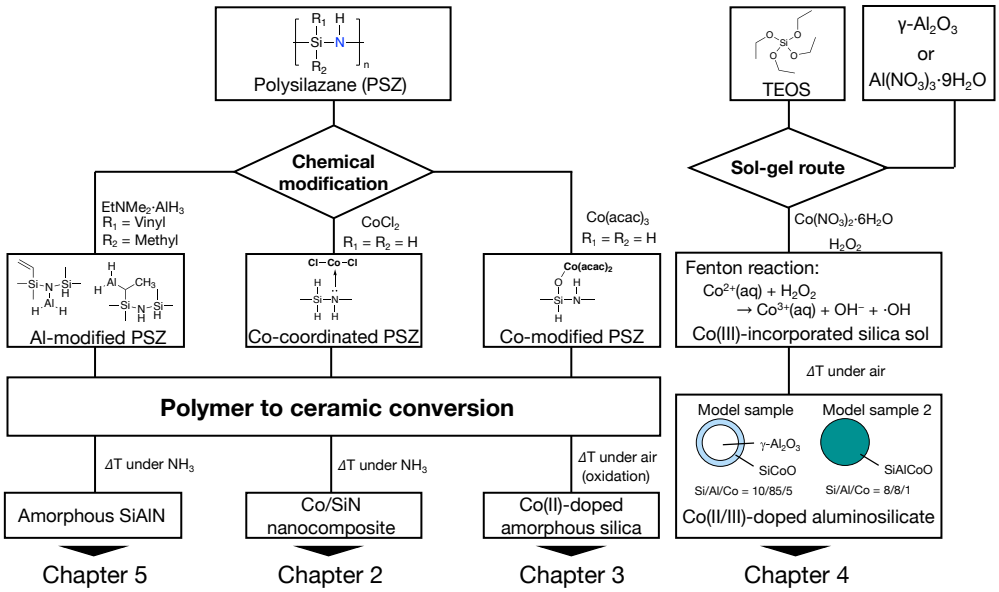

Fig. 1-6 Outline of the thesis and flowcharts of material synthesis using molecular precursor approach.

References

[1] In-situ CO_2 Data from Scripps CO_2 Program website. https://scrippsco2.ucsd.edu/data/atmospheric_co2/primary_mlo_co2_record.html

[2] D. Gielen, F. Boshell and D. Saygin, Climate and energy challenges for materials science, *Nat. Mater.*, 2016, **15**, 117–120.

[3] The United Nations website. https://sustainabledevelopment.un.org/partnership/?p=807 (Carbon Neutrality).

[4] Q. Wang, T. Hisatomi, Q. Jia, H. Tokudome, M. Zhong, C. Wang, Z. Pan, T. Takata, M. Nakabayashi, N. Shibata, Y. Li, I. D. Sharp, A. Kudo, T. Yamada and K. Domen, Scalable water splitting on particulate photocatalyst sheets with a solar-to-hydrogen energy conversion efficiency exceeding 1%, *Nat. Mater.*, 2016, **15**, 611–615.

[5] Y. Goto, T. Hisatomi, Q. Wang, T. Higashi, K. Ishikiriyama, T. Maeda, Y. Sakata, S. Okunaka, H. Tokudome, M. Katayama, S. Akiyama, H. Nishiyama, Y. Inoue, T. Takewaki, T. Setoyama, T. Minegishi, T. Takata, T. Yamada and K. Domen, A Particulate Photocatalyst Water-Splitting Panel for Large-Scale Solar Hydrogen Generation, *Joule*, 2018, **2**, 509–520.

[6] K. Akamatsu, T. Tago, M. Seshimo and S. I. Nakao, Long-term stable H_2 production from methylcyclohexane using a membrane reactor with a dimethoxydiphenylsilane-derived silica membrane prepared via chemical vapor deposition, *Ind. Eng. Chem. Res.*, 2015, **54**, 3996–4000.

[7] X. L. Zhang, K. Akamatsu and S. I. Nakao, Hydrogen Separation in Hydrogen-Methylcyclohexane-Toluene Gaseous Mixtures through Triphenylmethoxysilane-Derived Silica Membranes Prepared by Chemical Vapor Deposition, *Ind. Eng. Chem. Res.*, 2016, **55**, 5395–5402.

[8] W. E. Dasent, Inorganic Energetics: An Introduction., *Cambridge Texts in Chemistry and Biochemistry*,1982, pp. 103.

[9] J. M. Asensio, D. Bouzouita, P. W. N. M. van Leeuwen and B. Chaudret, σ-H–H, σ-C–H, and σ-Si–H Bond Activation Catalyzed by Metal Nanoparticles, *Chem. Rev.*, 2020, **120**, 1042–1084.

[10] Y. Feng, L. Liu, J.-T. Wang, H. Huang and Q.-X. Guo, Assessment of Experimental Bond Dissociation Energies Using Composite ab Initio Methods and Evaluation of the Performances of Density Functional Methods in the Calculation of Bond Dissociation Energies, *J. Chem. Inf. Comput. Sci.*, 2003, **43**, 2005–2013.

[11] L. R. Hilden and K. R. Morris, Physics of amorphous solids, *J. Pharm. Sci.*, 2004, **93**, 3–12.

[12] L. Zhang, M. Zhou, A. Wang and T. Zhang, Selective Hydrogenation over Supported Metal Catalysts: From Nanoparticles to Single Atoms, *Chem. Rev.*, 2020, **120**, 683–733.

[13] R. M. Kellogg, Reversible metal-free hydrogen activation, *Chemtracts*, 2007, **19**, 152–156.

[14] D. W. Stephan, The broadening reach of frustrated Lewis pair chemistry, *Science*, 2016, **354**, aaf7229.

[15] D. M. Camaioni, B. Ginovska-Pangovska, G. K. Schenter, S. M. Kathmann and T. Autrey, Analysis of the activation and heterolytic dissociation of H_2 by frustrated Lewis pairs: NH_3/BX_3 (X = H, F, and Cl), *J. Phys. Chem. A*, 2012, **116**, 7228–7237.

[16] P. Colombo, G. Mera, R. Riedel and G. D. Sorarù, Polymer-derived ceramics: 40 Years of research and innovation in advanced ceramics, *J. Am. Ceram. Soc.*, 2010, **93**, 1805–1837.

[17] E. Ionescu, H. J. Kleebe and R. Riedel, Silicon-containing polymer-derived ceramic nanocomposites (PDC-NCs): Preparative approaches and properties, *Chem. Soc. Rev.*, 2012, **41**, 5032–5052.

[18] M. Zaheer, T. Schmalz, G. Motz and R. Kempe, Polymer derived non-oxide ceramics modified with late transition metals, *Chem. Soc. Rev.*, 2012, **41**, 5102.

[19] D. Schumacher, M. Wilhelm and K. Rezwan, Porous SiOC monoliths with catalytic

activity by in situ formation of Ni nanoparticles in solution-based freeze casting, *J. Am. Ceram. Soc.*, 2020, **103**, 2991–3001.

[20] D. Forberg, T. Schwob and R. Kempe, Catalytic condensation for the formation of polycyclic heteroaromatic compounds, *Nat. Commun.*, 2018, **9**, 1751.

[21] D. Forberg, T. Schwob, M. Zaheer, M. Friedrich, N. Miyajima and R. Kempe, Single-catalyst high-weight% hydrogen storage in an N-heterocycle synthesized from lignin hydrogenolysis products and ammonia, *Nat. Commun.*, 2016, **7**, 13201.

[22] G. Glatz, T. Schmalz, T. Kraus, F. Haarmann, G. Motz and R. Kempe, Copper-Containing SiCN Precursor Ceramics (Cu@SiCN) as Selective Hydrocarbon Oxidation Catalysts Using Air as an Oxidant, *Chem. - A Eur. J.*, 2010, **16**, 4231–4238.

[23] M. Zaheer, T. Schmalz, G. Motz and R. Kempe, Polymer derived non-oxide ceramics modified with late transition metals, *Chem. Soc. Rev.*, 2012, **41**, 5102.

[24] D. Forberg, J. Obenauf, M. Friedrich, S.-M. Hühne, W. Mader, G. Motz and R. Kempe, The synthesis of pyrroles via acceptorless dehydrogenative condensation of secondary alcohols and 1,2-amino alcohols mediated by a robust and reusable catalyst based on nanometer-sized iridium particles, *Catal. Sci. Technol.*, 2014, **4**, 4188–4192.

[25] T. Schwob and R. Kempe, A Reusable Co Catalyst for the Selective Hydrogenation of Functionalized Nitroarenes and the Direct Synthesis of Imines and Benzimidazoles from Nitroarenes and Aldehydes, *Angew. Chemie Int. Ed.*, 2016, **55**, 15175–15179.

[26] M. Kamperman, A. Burns, R. Weissgraeber, N. van Vegten, S. C. Warren, S. M. Gruner, A. Baiker and U. Wiesner, Integrating Structure Control over Multiple Length Scales in Porous High Temperature Ceramics with Functional Platinum Nanoparticles, *Nano Lett.*, 2009, **9**, 2756–2762.

[27] S. M. Sachau, M. Zaheer, A. Lale, M. Friedrich, C. E. Denner, U. B. Demirci, S. Bernard, G. Motz and R. Kempe, Micro-/Mesoporous Platinum-SiCN Nanocomposite Catalysts (Pt@SiCN): From Design to Catalytic Applications, *Chem. - A Eur. J.*, 2016, **22**, 15508–15512.

[28] T. Schwob and R. Kempe, A Reusable Co Catalyst for the Selective Hydrogenation of Functionalized Nitroarenes and the Direct Synthesis of Imines and Benzimidazoles from Nitroarenes and Aldehydes, *Angew. Chemie Int. Ed.*, 2016, **55**, 15175–15179.

[29] C. Bäumler and R. Kempe, The Direct Synthesis of Imines, Benzimidazoles and Quinoxalines from Nitroarenes and Carbonyl Compounds by Selective Nitroarene Hydrogenation Employing a Reusable Iron Catalyst, *Chem. - A Eur. J.*, 2018, **24**, 8989–8993.

Chapter 2

Low temperature in-situ formation of cobalt in silicon nitride toward functional nitride nanocomposites

2.1 Introduction

This chapter describes the first demonstration of a low-temperature in-situ formation of Co nanocrystallites embedded within an amorphous silicon nitride matrix through a careful control of the chemistry behind material design [1–4] using perhydropolysilazane (PHPS) as a Si_3N_4 precursor—further coordinated with $CoCl_2$—and ammonia (NH_3) as a pyrolysis atmosphere.

As mentioned in Chapter 1, polymer derived ceramics (PDCs) route can precisely control the chemical composition of the final ceramic materials at molecular scale as well as their phase distribution and nanostructure [5,6]. This offers enhanced or novel functional properties via the rational design of materials through the PDCs route which have been recently highlighted in metal/Si-based (oxy-)carbide and carbonitride matrix composites such as Ni/SiC [7], Ni/SiOC [8], Ni/SiCN(O) [9] and M/SiCN (M = Pd [10], Ru [10], Pd_2Ru [11], Cu [12, 13], Ir [10, 14] , Ni [15], Pt [16, 17], Co [18], Fe [19]) derived from metal-modified polycarbosilanes, polysiloxanes and polysilazanes, respectively. Especially, as reported by Kempe et al, the polymer-derived M/SiCN nanocomposites are attractive as robust and reusable catalyst which can be applied to various catalytic reactions by changing the metal nanoparticle component: dehydrogenation by Pd [10]; hydrogenation and dehydrogenation of N-heterocycles by Pd_2Ru [11]; selective hydrocarbon oxidation by Cu [12, 13]; dehydrogenative condensation of secondary alcohols and 1,2-amino alcohols by Ir [14]; chemoselective hydrogenation of nitroarenes by Ni [15], Co [18] and Fe [19], and hydrolysis of sodium borohydride by Pt [17].

In contrast, the design of metal/Si-based composites in nitride matrix systems (*i.e.*, M/Si_3N_4) has never been demonstrated and remains highly challenging while nitrides can be particularly interesting for catalysis as a support and/or as a catalyst itself [20–25]. This is mainly caused by the reactivity of the central metal cations distributed in the polysilazane network with NH_3 (used as atmosphere to form Si_3N_4 from polysilazanes) forming a metal nitride nanophase distributed in the Si_3N_4 matrix. This observation is well illustrated in the

recent reports on Si_3N_4-based nanocomposites including TiN/Si_3N_4 [26,27] and VN/Si_3N_4 [28] compounds. Among them, the TiN/Si_3N_4 nanocomposites exhibited strong synergy with Pt nanoparticles, which were homogeneously deposited in a second synthesis step onto the nanocomposite support. This resulted in excellent catalytic performances for dehydrogenation of sodium borohydride in water [27]. Thus, this report confirmed the attractivity of nitrides for catalysis. To simplify this two-step process, avoid the use of precious metals such as Pt while forming Si_3N_4 supporting the catalytically active phase (*i.e.*, M/Si_3N_4) in a one-step process, we describe the coordination of a polysilazane (PHPS) with cobalt chloride ($CoCl_2$) allowing the in-situ formation of Co during the further thermo-chemical conversion of the PHPS into Si_3N_4 in flowing NH_3. The unique low-temperature in-situ formation of Co within the Si_3N_4 matrix is discussed based on a complete set of characterization techniques including elemental analyses, X-ray diffraction (XRD), thermogravimetric - mass spectrometric (TG-MS) analyses, infrared spectroscopy, ultraviolet-visible (UV-Vis) spectroscopy and transmission electron microscopy (TEM) observations. The basis of our approach comes first from the design of a suitable highly pure synthetic precursor in which uniform chemical composition is established at molecular scale. Thus, we mixed $CoCl_2$ with PHPS—which only contains Si, N and H elements—in a controlled Co/Si molar ratio of 0.2 to form a compound labeled **Co-PHPS**. The synthesis is performed in toluene and directed to keep a homogeneous distribution of $CoCl_2$ throughout the PHPS network without direct reaction. Then, the precursor is heat-treated under NH_3 to form a thermally unstable metal nitride phase at low temperatures, while avoiding the formation of free Si at higher temperatures as known using PHPS [29, 30]; thus, leading to Co/Si_3N_4 compounds at low and intermediate temperatures as discussed below.

2.2 Experimental procedure

2.2.1 Sample synthesis

A flowchart of synthesis of **Co-PHPS** and subsequent pyrolysis under NH_3 is shown in Fig. 2-1. Perhydropolysilazane (PHPS, NN110-20, 20 wt% in butyl ether solution) was provided by Merck KGaA, Darmstadt, Germany. The butyl ether was substituted by super-anhydrous toluene (99.5 % purity, Wako Pure Chemical Industries, Ltd., Osaka, Japan). $CoCl_2$ (97% purity, Sigma-Aldrich Japan, Tokyo, Japan) was used as-received. The handling of the chemicals and reagents was performed using standard Schlenk techniques. The synthesis of the cobalt-modified PHPS labeled **Co-PHPS** was performed according to a Co/Si molar ratio of 0.2. A 100 mL two-neck round-bottom flask equipped with a magnetic stirrer was charged with

the solvent-substituted PHPS (10 mL, 4.25 mmol, 19 wt% in toluene) and anhydrous toluene (50 mL). $CoCl_2$ (1.137 g, 0.85 mmol) was added to the solution at room temperature (RT), and refluxed for 12 h. Then, the solvent was removed under vacuum at RT. The **Co-PHPS** sample was subsequently pyrolyzed under flowing NH_3 at specific temperatures of 400, 500, 800 and 1000 °C for 2 h with a heating rate of 5 °C min^{-1}. The as-pyrolyzed samples were labelled as **Co/SiNX** (**X** being the temperature at which the material has been heat-treated).

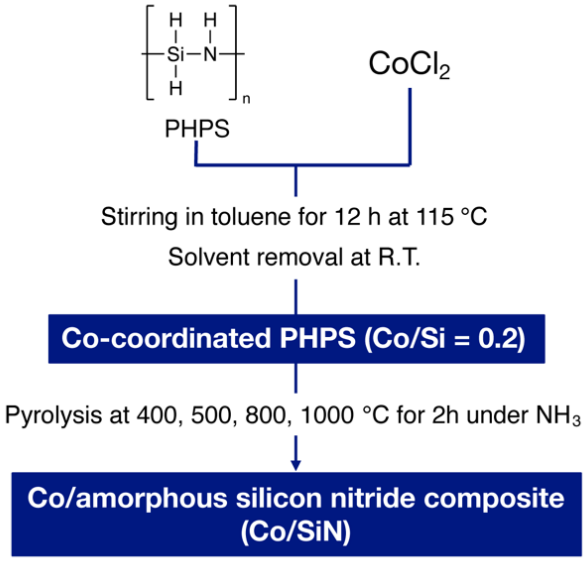

Fig. 2-1 A flowchart of synthesis of **Co-PHPS** and subsequent pyrolysis under NH_3.

2.2.2 Characterizations

The chemical modification performed in this study was monitored by attenuated total reflection flourier transform infra-red (ATR-FTIR) spectroscopy using FTIR spectrometer (FT/IR-4200IF, JASCO Corporation, Tokyo, Japan) with attachment of ATR equipment (ATR PRO 550S-S/570S-H, JASCO Corporation, Tokyo, Japan) at a resolution of 4 cm^{-1}.

Elemental analyses were performed for oxygen and nitrogen (inert-gas fusion method, Model EMGA-930, HORIBA, Ltd., Kyoto, Japan), and carbon (non-dispersive infrared method, Model CS844, LECO Co., St Joseph, MI, USA). Then, the composition of **Co/SiNX** samples was calculated as:

$$wt\%(Si+Co) = 100\% - wt\%(C) - wt\%(N) - wt\%(O) \qquad (2\text{-}1)$$

The Co content in the **Co/SiNX** samples was analyzed by the energy dispersive X-ray spectroscopy (EDS) mounted on a scanning electron microscope (SEM, Model JSM-6010LA, JEOL Ltd., Tokyo, Japan), and evaluated as Co/Si atomic ratio.

XRD measurements were performed on powder samples using CoKα radiation (Model Miniflex 600NB, Rigaku Co., ltd., Tokyo, Japan). The average crystallite size, L was obtained from Scherrer equation,

$$L = K\lambda/\beta\cos\theta \qquad (2\text{-}2)$$

where l is the X-ray wavelength in nanometer, β is the peak width of the diffraction peak at half maximum height in radian and K is a constant related to crystallite shape, normally taken as 0.9.

TEM observations were performed on the **Co/SiN800** sample using an atomic-resolution analytical microscope (Model JEM-ARM200F, JEOL Ltd., Tokyo, Japan) operated at an accelerating voltage of 200 kV.

The simultaneous TG-MS analyses up to 1000 °C under flowing helium (He) was performed on **Co-PHPS** sample by TG-DTG (Model STA7200, Hitachi High-Tech Science Corporation, Tokyo, Japan, heating rate of 10 °C min^{-1}) coupled with a quadrupole mass-spectrometry (Model JMS-Q1500GC, JEOL Ltd., Tokyo, Japan).

Ultraviolet-Visible (UV-Vis) absorption spectra in the range of 200–800 nm were recorded on **Co-PHPS** sample and pure $CoCl_2$ using an ultraviolet-visible near-infrared spectrometer (Model: V-670SP, JASCO Corporation, Tokyo, Japan) with integrating sphere attachment (Model: ISN-723, JASCO Corporation, Tokyo, Japan).

2.3 Results and discussion

Chemical compositions of the **Co/SiNX** samples (Table 2-1) are discussed in relation to their XRD patterns (Fig. 2-2), TG-MS experiments (Fig. 2-3) and FTIR spectroscopy (Fig. 2-6). The **Co/SiN400** sample exhibits three characteristic diffraction peaks assigned to α-Co (JCPDS No. 00-015-0806—at 2θ = 48.6, 52.0, and 55.6 °) along with a residual component of $CoCl_2$ (JCPDS No. 01-085-0446) and NH_4Cl (JCPDS No. 01-073-0365). Additionally, two small diffraction peaks appear at 2θ angles of 46.5 and 50.4 °, indicating the formation of cobalt nitride (Co_2N, JCPDS No. 04-004-4638). Then, at 500 °C (**Co/SiN500** sample), the Co_2N disappears while the metallic α-Co forms. At 800 °C (**Co/SiN800** sample), two distinct

diffraction peaks appear at 51.8 and 60.7 °, which are assigned to β-Co (JCPDS No. 01-089-4308) along with α-Co, and several minor peaks related to both α- and β-Si_3N_4 were also identified. The NH_4Cl XRD peaks disappeared because of its vaporization when heated above 500 °C, this was confirmed by its condensation in the cool parts (extremities) of the furnace tube. Finally, the **Co/SiN1000** sample exhibits formation of thermodynamically favorable cobalt silicide (Co_2Si, JCPDS No. 01-089-4181) in addition to the α- and β-Si_3N_4 phases. Thus, Co/Si_3N_4 (amorphous and crystalline) composites are generated at temperatures below 800 °C.

Table 2-1 Chemical composition of **Co/SiNX**

Name	Composition / wt%					Composition / at%
	EDS (Co/Si ratio)		Elemental analysis / wt%			Atomic ratio to Si
	Si	Co	C	N	O	
Co/SiN400	44.83	35.23	0.80	16.84	2.30	$Si_1\ Co_{0.37}\ C_{0.04}\ N_{0.75}\ O_{0.09}$
Co/SiN500	57.40	22.32	0.93	16.36	2.99	$Si_1\ Co_{0.19}\ C_{0.04}\ N_{0.57}\ O_{0.09}$
Co/SiN800	52.89	16.70	0.50	23.73	6.18	$Si_1\ Co_{0.15}\ C_{0.02}\ N_{0.90}\ O_{0.21}$
Co/SiN1000	53.84	16.08	0.01	26.09	3.98	$Si_1\ Co_{0.14}\ C_{0.00}\ N_{0.97}\ O_{0.13}$

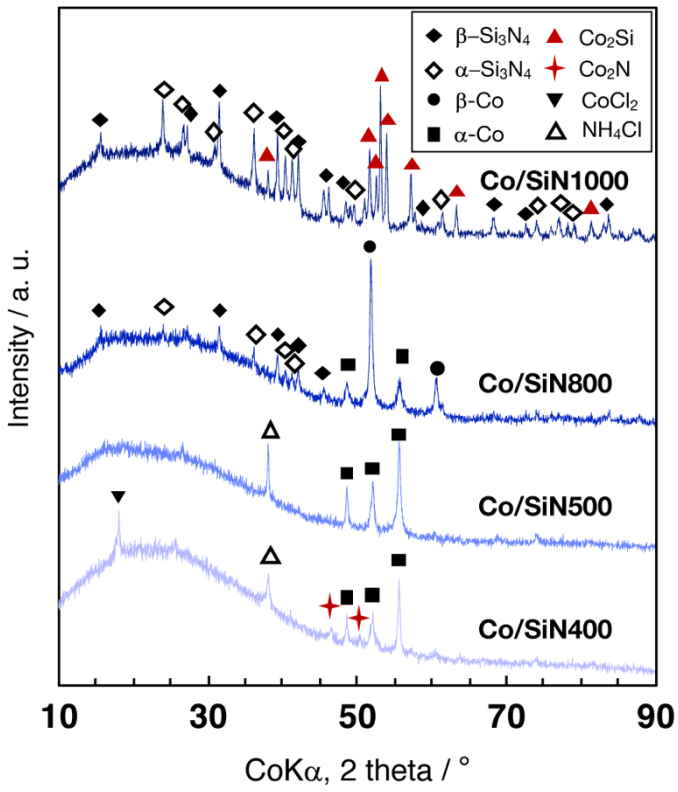

Fig. 2-2 XRD patterns of **Co/SiNX** samples.

In order to investigate this low-temperature in-situ formation of α/β-Co, TG-MS analyses have been performed. The TG-curve (Fig. 2-3a) exhibits two main weight loss regions at 50–220 °C and 220–350 °C. The coupled MS analysis reveals that the main evolved component at 50–220 °C is toluene ($C_6H_5CH_3$, m/z = 91, Fig. 2-3b) used as the reaction solvent, while at 220–350 °C, the dominant gaseous species provide chloride fragments, such as hydrochloric acid (HCl, m/z = 36 and 38, Fig. 2-3c), monochlorosilane (m/z = 64 and 66, Fig. 2-3d) and dichlorosilane (m/z = 99 and 101, Fig. 2-3e) species.

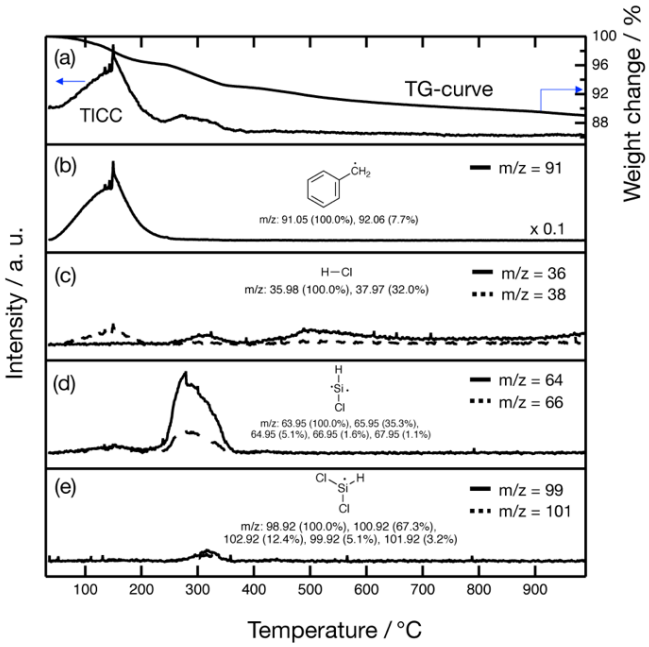

Fig. 2-3 TG-MS analyses under flowing He of the **Co-PHPS** sample: (a) a TG-curve and a total ion current chromatogram (TICC), (b)~(e) the simultaneous monitoring of gaseous products formed in-situ.

As shown in Fig. 2-4, a color change from blue to gray was observed for the $CoCl_2$-dispersed PHPS toluene solution after reflux at 110 °C for 12h. The visible color change was also monitored by the UV-Vis absorption spectroscopy (Fig. 2-5): as-received $CoCl_2$ exhibits a broad peak around 600 nm attributed to octahedral coordination of $CoCl_2$ [31, 32], while the **Co-PHPS** sample recovered after the 110 °C-refluxing in toluene presents additional absorption bands at 670 and 700 nm assigned to typical bands of tetrahedral coordination which attributed to the formation of $CoCl_2L_2$ (L = ligands) [31, 32].

In addition, according to the FTIR spectrum of the **Co-PHPS** shown in Fig. 2-6, the characteristic bands at 3370 cm^{-1} (νN–H) [30] of PHPS slightly shift toward lower wavenumber of 3365 cm^{-1}, suggesting the $CoCl_2$ coordination to the NH group of PHPS. We therefore suggest that the reaction between PHPS and $CoCl_2$ better proceeded during the

pyrolysis, and the NH_4Cl species detected in the XRD patterns of the **Co/SiN400** and **Co/SiN500** samples (Fig.2-2) are by-products resulting from the nucleation reaction between HCl formed in-situ and the gaseous NH_3 [33].

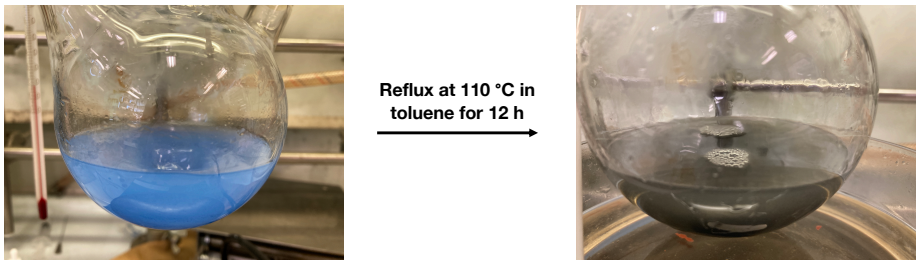

Fig. 2-4 A color change of $CoCl_2$-dispersed PHPS toluene solution observed after reflux at 110 °C for 12h.

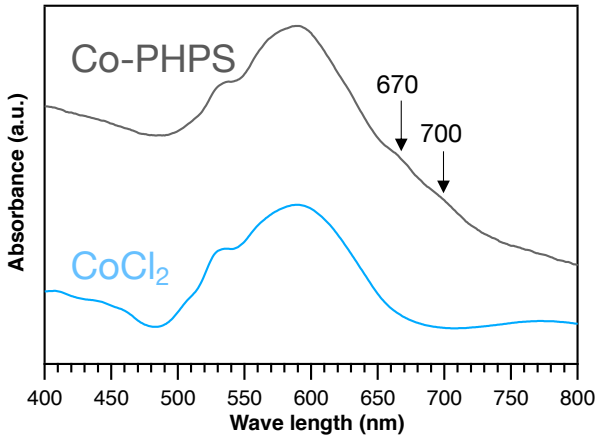

Fig. 2-5 UV-Vis absorption spectra of **Co-PHPS** sample and pure $CoCl_2$.

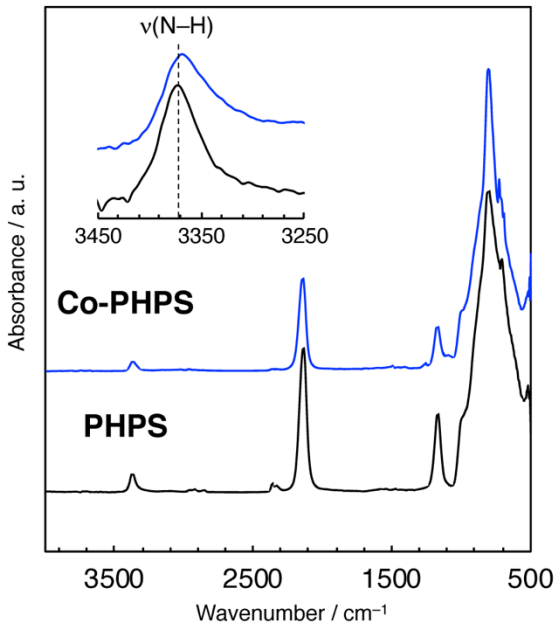

Fig. 2-6 ATR-IR spectra for as-received PHPS and Co-modified PHPS.

As shown in Table 2-1, the Co/Si ratio of **Co/SiN400** sample (0.37) was apparently higher than the nominal Co/Si ratio of **Co-PHPS** (0.2), which can be explained by the elimination of chlorosilanes at 220–350 °C (Figs. 2-3(d) and (e)), *i.e.*, the number of Si–H group decreases. Furthermore, from 400 to 500 °C, the N/Si atomic ratio decreased from 0.75 to 0.57 (**Co/SiN500**). This corresponds to the reported thermal decomposition of Co_2N at 350–450 °C [34]. Consequently, these results indicate that the following reactions proceed stepwise as shown in Fig. 2-7:

i) At 220–350 °C, Si–N cleavages in Co-PSZ sample proceed via reaction of the silicon center and N–H group of PHPS with $CoCl_2$ associated with the elimination of chlorosilanes and HCl to afford Co_2N, respectively.

ii) At 350–450 °C, Co_2N thermally decomposes to yield metallic-Co.

The N/Si ratio of **Co/SiNX** samples in Table 2-1 increased during pyrolysis from 500 to 1000 °C, indicating the occurrence of nitridation of the evolutive polymer under NH_3 above 500 °C [35]. Moreover, the crystallization of Si_3N_4 started at 800 °C, which was approximately 400 °C lower than that of Co-free PHPS-derived amorphous silicon nitride [30]. Table 2-2 presents the relationship between the pyrolysis temperature and the average crystallite sizes evaluated for α-Co (101) and β-Co (111). The initial low-temperature crystallization (400 °C) of α-Co yields crystallites of approximately 106 nm. Then, consistently with the pyrolysis

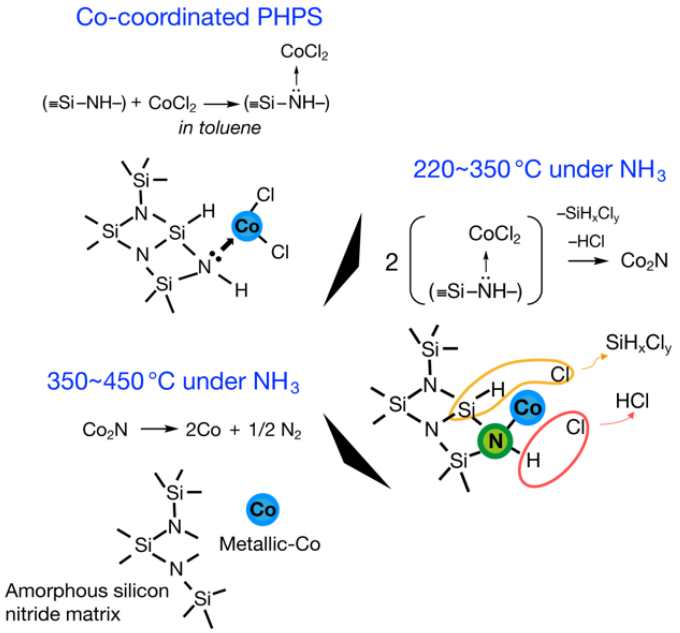

Fig. 2-7 Possible mechanism of in-situ formation of Co nanocrystallite embedded on Si_3N_4 matrix derived from **Co-PHPS**.

Table 2-2 Relationship between the pyrolysis temperature and the average crystallite sizes evaluated for α-Co (101) and β-Co (111).

	Co/SiN400	Co/SiN500	CoSiN800
α-Co (101)	106	76	29
β-Co (111)	-	-	74

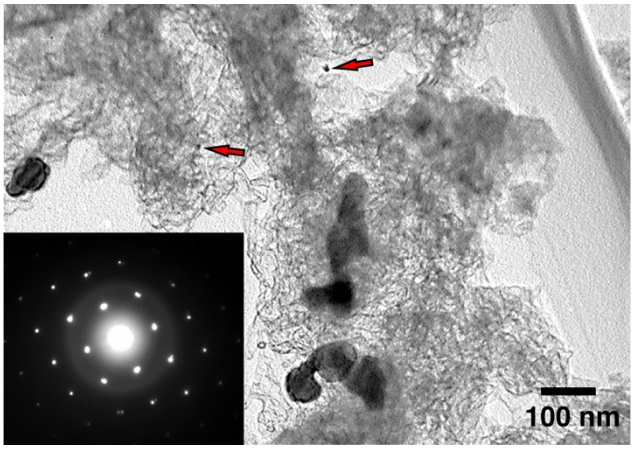

Fig. 2-8 TEM image of **Co/SiN800** sample, and corresponding SAED patterns obtained from the aggregated nanocrystallites with dark contrast, and the arrows pointing out to several nanometer sized Co crystallites.

temperature, the α-Co nanocrystallites decrease their size via phase transformation to thermally favorable β-Co, and the Scherrer analysis indicated an average β-Co nanocrystallite size of 74.4 nm for the **Co/SiN800** sample.

To gather micro- and nanostructural information, TEM investigations were performed on the **Co/SiN800** sample (Fig. 2-8). The TEM image of **Co/SiN800** sample shows aggregated nanocrystallites with dark contrast and diameter of about 40–80 nm which are embedded in a network with the typical phase contrast of amorphous materials. The corresponding selected area electron diffraction (SAED) patterns confirm the indexation of both α- and β-Co (inset in Fig. 2-8). Neither silicon segregations nor inclusions along grain boundaries are observed, while dark spots with several nanometers in size (typical ones are indicated by arrows) are observed which suggested the crystallite size distribution of Co embedded within the silicon nitride matrix are bimodal: several nanometers and 40 to 80 nm.

2.4 Conclusions

The addition of cobalt chloride ($CoCl_2$) to toluene solution of PHPS in a 1/5 molar ratio generated a cobalt-coordinated PHPS that was heat-treated in flowing NH_3 in the temperature

range of 400 to 800 °C to favor the in-situ growth of Co nanoparticles within an amorphous silicon nitride matrix. The highlights can be summarized as follows:

(1) Formation of Co_2N formed in-situ by the reaction of $CoCl_2$ with the Si center and NH group of PHPS at 220–350 °C.
(2) Co started growing at temperature as low as 400 °C via the thermal decomposition of Co_2N.
(3) Crystallization of the amorphous silicon nitride matrix proceeded at 800 °C.

Further investigations on the molecular structure of the single-source precursors and subsequent pyrolysis conditions at the low temperatures are still in progress. Therefore, this study paves the way for the rational one-step synthesis of metal/nitride nanocomposites that may be applied in a wide range of catalysis-assisted reactions for energy-related fields. These opportunities are now being addressed. It is anticipated that this will lead to host of structural and functional applications for a new generation of advanced ceramics.

References

[1] C. Sanchez, C. Boissiere, S. Cassaignon, C. Chaneac, O. Durupthy, M. Faustini, D. Grosso, C. Laberty-Robert, L. Nicole, D. Portehault, F. Ribot, L. Rozes and C. Sassoye, Molecular engineering of functional inorganic and hybrid materials, *Chem. Mater.*, 2014, **26**, 221–238.

[2] S. Clément and A. Mehdi, Sol-Gel Chemistry: From Molecule to Functional Materials, *Molecules*, 2020, **25**, 2538.

[3] C. Sanchez, L. Rozes, F. Ribot, C. Laberty-Robert, D. Grosso, C. Sassoye, C. Boissiere and L. Nicole, "Chimie douce": A land of opportunities for the designed construction of functional inorganic and hybrid organic-inorganic nanomaterials, *Comptes Rendus Chim.*, 2010, **13**, 3–39.

[4] A. Lale, M. Schmidt, M. D. Mallmann, A. V. A. Bezerra, E. D. Acosta, R. A. F. Machado, U. B. Demirci and S. Bernard, Polymer-Derived Ceramics with engineered mesoporosity: From design to application in catalysis, *Surf. Coatings Technol.*, 2018, **350**, 569–586.

[5] P. Colombo, G. Mera, R. Riedel and G. D. Sorarù, Polymer-derived ceramics: 40 Years of research and innovation in advanced ceramics, *J. Am. Ceram. Soc.*, 2010, **93**, 1805–1837.

[6] E. Ionescu, H. J. Kleebe and R. Riedel, Silicon-containing polymer-derived ceramic nanocomposites (PDC-NCs): Preparative approaches and properties, *Chem. Soc. Rev.*, 2012, **41**, 5032–5052.

[7] M. Zaheer, J. Hermannsdörfer, W. P. Kretschmer, G. Motz and R. Kempe, Robust Heterogeneous Nickel Catalysts with Tailored Porosity for the Selective Hydrogenolysis of Aryl Ethers, *ChemCatChem*, 2014, **6**, 91–95.

[8] D. Schumacher, M. Wilhelm and K. Rezwan, Porous SiOC monoliths with catalytic activity by in-situ formation of Ni nanoparticles in solution-based freeze casting, *J. Am. Ceram. Soc.*, 2020, **103**, 2991–3001.

[9] M. Seifollahi Bazarjani, H.-J. Kleebe, M. M. Müller, C. Fasel, M. Baghaie Yazdi, A. Gurlo and R. Riedel, Nanoporous Silicon Oxycarbonitride Ceramics Derived from Polysilazanes In-situ Modified with Nickel Nanoparticles, *Chem. Mater.*, 2011, **23**, 4112–4123.

[10] D. Forberg, T. Schwob and R. Kempe, Catalytic condensation for the formation of polycyclic heteroaromatic compounds, *Nat. Commun.*, 2018, **9**, 1751.

[11] D. Forberg, T. Schwob, M. Zaheer, M. Friedrich, N. Miyajima and R. Kempe, Single-catalyst high-weight% hydrogen storage in an N-heterocycle synthesized from lignin hydrogenolysis products and ammonia, *Nat. Commun.*, 2016, **7**, 13201.

[12] G. Glatz, T. Schmalz, T. Kraus, F. Haarmann, G. Motz and R. Kempe, Copper-Containing SiCN Precursor Ceramics (Cu@SiCN) as Selective Hydrocarbon Oxidation Catalysts Using Air as an Oxidant, *Chem. - A Eur. J.*, 2010, **16**, 4231–4238.

[13] M. Zaheer, T. Schmalz, G. Motz and R. Kempe, Polymer derived non-oxide ceramics modified with late transition metals, *Chem. Soc. Rev.*, 2012, **41**, 5102.

[14] D. Forberg, J. Obenauf, M. Friedrich, S.-M. Hühne, W. Mader, G. Motz and R. Kempe, The synthesis of pyrroles via acceptorless dehydrogenative condensation of secondary alcohols and 1,2-amino alcohols mediated by a robust and reusable catalyst based on nanometer-sized iridium particles, *Catal. Sci. Technol.*, 2014, **4**, 4188–4192.

[15] T. Schwob and R. Kempe, A Reusable Co Catalyst for the Selective Hydrogenation of Functionalized Nitroarenes and the Direct Synthesis of Imines and Benzimidazoles from Nitroarenes and Aldehydes, *Angew. Chemie Int. Ed.*, 2016, **55**, 15175–15179.

[16] M. Kamperman, A. Burns, R. Weissgraeber, N. van Vegten, S. C. Warren, S. M. Gruner, A. Baiker and U. Wiesner, Integrating Structure Control over Multiple Length Scales in Porous High Temperature Ceramics with Functional Platinum Nanoparticles, *Nano Lett.*,

2009, **9**, 2756–2762.

[17] S. M. Sachau, M. Zaheer, A. Lale, M. Friedrich, C. E. Denner, U. B. Demirci, S. Bernard, G. Motz and R. Kempe, Micro-/Mesoporous Platinum-SiCN Nanocomposite Catalysts (Pt@SiCN): From Design to Catalytic Applications, *Chem. - A Eur. J.*, 2016, **22**, 15508–15512.

[18] T. Schwob and R. Kempe, A Reusable Co Catalyst for the Selective Hydrogenation of Functionalized Nitroarenes and the Direct Synthesis of Imines and Benzimidazoles from Nitroarenes and Aldehydes, *Angew. Chemie Int. Ed.*, 2016, **55**, 15175–15179.

[19] C. Bäumler and R. Kempe, The Direct Synthesis of Imines, Benzimidazoles and Quinoxalines from Nitroarenes and Carbonyl Compounds by Selective Nitroarene Hydrogenation Employing a Reusable Iron Catalyst, *Chem. - A Eur. J.*, 2018, **24**, 8989–8993.

[20] Y. Han, X. Yue, Y. Jin, X. Huang and P. K. Shen, Hydrogen evolution reaction in acidic media on single-crystalline titanium nitride nanowires as an efficient non-noble metal electrocatalyst, *J. Mater. Chem. A*, 2016, **4**, 3673–3677.

[21] M.-S. Balogun, W. Qiu, W. Wang, P. Fang, X. Lu and Y. Tong, Recent advances in metal nitrides as high-performance electrode materials for energy storage devices, *J. Mater. Chem. A*, 2015, **3**, 1364–1387.

[22] W. Yang, S. Rehman, X. Chu, Y. Hou and S. Gao, Transition Metal (Fe, Co and Ni) Carbide and Nitride Nanomaterials: Structure, Chemical Synthesis and Applications, *ChemNanoMat*, 2015, **1**, 376–398.

[23] M.-S. Balogun, Y. Huang, W. Qiu, H. Yang, H. Ji and Y. Tong, Updates on the development of nanostructured transition metal nitrides for electrochemical energy storage and water splitting, *Mater. Today*, 2017, **20**, 425–451.

[24] J. S. J. Hargreaves, Heterogeneous catalysis with metal nitrides, *Coord. Chem. Rev.*, 2013, **257**, 2015–2031.

[25] S. Dong, X. Chen, X. Zhang and G. Cui, Nanostructured transition metal nitrides for energy storage and fuel cells, *Coord. Chem. Rev.*, 2013, **257**, 1946–1956.

[26] M. C. Bechelany, V. Proust, A. Lale, P. Miele, S. Malo, C. Gervais and S. Bernard, Nanocomposites through the Chemistry of Single-Source Precursors: Understanding the Role of Chemistry behind the Design of Monolith-Type Nanostructured Titanium Nitride/Silicon Nitride, *Chem. - A Eur. J.*, 2017, **23**, 832–845.

[27] A. Lale, M. D. Mallmann, S. Tada, A. Bruma, S. Özkar, R. Kumar, M. Haneda, R. A.

Francisco Machado, Y. Iwamoto, U. B. Demirci and S. Bernard, Highly active, robust and reusable micro-/mesoporous TiN/Si3N4 nanocomposite-based catalysts for clean energy: Understanding the key role of TiN nanoclusters and amorphous Si3N4 matrix in the performance of the catalyst system, *Appl. Catal. B Environ.*, 2020, **272**, 118975.

[28] C. Zhou, A. Ott, R. Ishikawa, Y. Ikuhara, R. Riedel and E. Ionescu, Single-source-precursor synthesis and high-temperature evolution of novel mesoporous SiVN(O)-based ceramic nanocomposites, *J. Eur. Ceram. Soc.*, 2020, **40**, 6280–6287.

[29] M. Biesuz, P. Bettotti, S. Signorini, M. Bortolotti, R. Campostrini, M. Bahri, O. Ersen, G. Speranza, A. Lale, S. Bernard and G. D. Sorarù, First synthesis of silicon nanocrystals in amorphous silicon nitride from a preceramic polymer, *Nanotechnology*, 2019, **30**, 255601.

[30] Y. Iwamoto, K. I. Kikuta and S. I. Hirano, Synthesis of poly-titanosilazanes and conversion into Si_3N_4-TiN ceramics, *J. Ceram. Soc. Japan*, 2000, **108**, 350–356.

[31] C. L. Hussey and T. M. Laher, Electrochemical and spectroscopic studies of cobalt(II) in molten aluminum chloride-n-butylpyridinium chloride, *Inorg. Chem.*, 1981, **20**, 4201–4206.

[32] I. Sava, M.-D. Damaceanu and G. Lisa, Insights into the physico-chemical behavior of $CoCl_2$/polyimide hybrid materials, *J. Polym. Res.*, 2016, **23**, 130.

[33] S. Thompson, P. D. Shipman, S. P. Shipman and T. J. Zurlinden, The counterdiffusion of HCl and NH 3 : An experimental and modeling analysis of topochemistry, diffusion, reaction, and phase transitions, *J. Chem. Phys.*, 2019, **150**, 154306.

[34] L. Maya, M. Paranthaman, J. R. Thompson, T. Thundat and R. J. Stevenson, Ferromagnetic nanocomposite films of cobalt in a ceramic matrix formed by thermal decomposition of cobalt nitride, CoN, precursor, *J. Appl. Phys.*, 1996, **79**, 7905–7910.

[35] G. T. Burns and G. Chandra, Pyrolysis of Preceramic Polymers in Ammonia: Preparation of Silicon Nitride Powders, *J. Am. Ceram. Soc.*, 1989, **72**, 333–337.

Chapter 3

Hydrogen transport property of polymer-derived cobalt-doped amorphous silica

3.1 Introduction

This chapter demonstrates the effect of local structure of Co-doped amorphous silica (SiO_2) on hydrogen transport property aiming to improve high-temperature hydrogen-permselectivity of microporous amorphous SiO_2-based membranes for high-temperature hydrogen separation.

In the previous chapter, Co-coordinated PHPS—without a certain covalent bond formation—has been synthesized, in contrast, a series of Co-modified PHPS with a certain amount of Si–O–Co bonds was synthesized through the PDCs route, which then Co cation-doped SiO_2 materials with Co/Si atomic ratios ranging from 0.01 to 0.18 were successfully converted from the Co-modified PHPS precursors. Then, hydrogen transport property of the Co-doped amorphous SiO_2 materials was discussed.

Microporous SiO_2 membranes with molecular sieve-like properties have relatively high gas permeances, and better thermal stability in comparison with polymer membranes [1-5]. Thus, they are attractive for application to membrane reactors such as in the steam-reforming reactions of natural gas [5-7] and in the dehydrogenation of chemical hydrides [8-11]. The SiO_2 membrane component is also attractive for developing novel mixed matrix membranes combined with polymer membrane component such as polysulfone [12] which show better membrane performance with improved mechanical properties. Moreover, SiO_2 membranes can be further modified as SiO_2-based organic-inorganic hybrid membranes for other applications such as liquid-phase separation [13]. The high H_2-selectivity has been recognized to be achieved by molecular sieve property of amorphous SiO_2 network having micropores approximately 0.3 nm in size [3-5]. The microporosity can be formed in-situ with respect to the branched fractal dimensions having high amount of silanol (Si–OH) groups [14]. Accordingly, microporous SiO_2 membranes are moisture sensitive [15] and lack of hydrothermal stability [16]. In this regard, amorphous SiO_2-based composite membranes including composite membranes with an oxide system such as zirconium (Zr)-doped SiO_2 (Si-Zr-O) [17], nickel (Ni)-doped SiO_2 (Si-Ni-O) [18] and cobalt-doped SiO_2 (Si-Co-O) [19] have

been investigated in order to enhance their thermal and hydrothermal stabilities of SiO_2 membranes for practical applications. In this category of materials, doping SiO_2 with Co was found as effective for enhancing hydrogen permeance at 500 °C [20]. Nanostructural characterization of the Co-doped amorphous SiO_2-based composite membranes revealed that fine particles having a size range of approximately 5 to 20 nm were formed in-situ within an amorphous SiO_2 matrix [20]. The selected area electron diffraction ring patterns derived from the nanoparticles were mainly assigned to CoO and Co_3O_4; and metallic Co was a minor phase [20]. These results suggested that cobalt cation in the amorphous SiO_2 matrix play an important role for the enhancement of the hydrogen transport.

More recently, amorphous SiO_2-based composite membranes were designed and synthesized through an alternative synthesis approach based on inorganic/organometallic polymers, namely polymer-derived ceramics (PDCs) route, and their gas permeation properties were investigated. As an illustration, Co-doped ethoxy polysiloxane-derived SiO_2 membranes have been reported to show reversible gas molecular sieving property for high temperature gas separation [21]. As the polysiloxanes were partly condensed SiO_2 precursor, Co-doped SiO_2 membrane was prepared by a sol-gel method without any extended hydrolysis time and acidic catalyst such as nitric acid or hydrogen peroxide. Consequently, condensation proceeds the cluster-cluster growth to form very open fractal structures in the polysiloxane sol-gel process [21]. Thus, the proposed reversible gas molecular sieving property was derived from the alternating volume shrinkage/expansion governed by the reducing/oxidizing (redox) state change of the Co oxide particles ($Co(OH)_2$ and CoO /Co_3O_4) dispersed within the amorphous SiO_2 matrix derived from ethoxy polysiloxane [21]. The results also revealed that the oxidation state of Co remained II or III under the reducing conditions which is most probably related to the use of polysiloxanes as polymeric precursors. As reported previously [19, 20], phase separation and subsequent crystallization of Co oxides from the ternary Si-Co-O system easily proceeds during the thermal conversion of precursors prepared through the conventional sol-gel route. This encouraged us to design Co-doped SiO_2 membrane materials via the i) chemical modification of a non-oxidic preceramic polymer as a SiO_2 precursor with a Co source, ii) detailed characterization of the material at each step of the process (Co-modified precursors, pyrolysis intermediates, …), iii) investigation of the local structure located at the hetero interface between amorphous SiO_2 and Co oxide particles, iv) study of the relationships between the atomic and/or molecular structure of the ternary amorphous Si-Co-O system and its hydrogen transport property. Thus, in this study, a series of ternary Si-Co-O amorphous

compounds with measured Co/Si atomic ratios ranging from 0.01 to 0.18 were successfully synthesized through PDCs route using polysilazanes as non-oxidic precursors of the SiO_2 phase and acetylacetonate precursors as Co source. The Co-modified polysilazane was characterized in detail and then, thermo-chemically converted into Co-doped SiO_2. As-pyrolyzed Co-doped SiO_2 samples were chemically and structurally analyzed and hydrogen/deuterium isotope exchange behavior on the surface silanol groups of the amorphous Si-Co-O compounds was monitored in-situ. The contribution of the dopant Co within amorphous SiO_2 network in hydrogen transport property was discussed.

3.2 Experimental procedure

3.2.1 Synthesis of Co-modified polysilazanes for Co-doped amorphous silica

Commercially available PHPS (NN110-20, 20 wt% in xylene solution) was provided by AZ Electronic Materials Co., Ltd., Japan. ^{1}H NMR (300 MHz, C_6D_6, δ/ppm): 1.6-0.3 (br, N–H), 5.8-4.3 (br, Si–H); IR (CsI windows/cm^{-1}): νN–H = 3374 (m), νSi–H = 2125 (vs), δN–H = 1173 (m), δN–Si–N = 1020-840 (vs). Cobalt(III)-acetylacetonate ($Co(acac)_3$, purity > 98.0 %, Tokyo Chemical Industry Co., Ltd., Tokyo, Japan), and super-anhydrous toluene (99.5 % purity, Wako Pure Chemical Co., Ltd., Osaka, Japan) were used as-received without further purification. The chemical modification of PHPS with $Co(acac)_3$ was carried out under dry argon (Ar) atmosphere using Schlenk line and glovebox techniques. The synthesis of Co-modified PHPS samples was performed according to various atomic ratios of Co in $Co(acac)_3$ to Si in PHPS (Co/Si) = 1/8; 1/20; 1/40 and 1/80. The resulting synthesized precursors were labeled as CoPHPS1/8; CoPHPS1/20; CoPHPS1/40 and CoPHPS1/80, respectively. The flowchart of synthesis of Co-modified PHPS and subsequent oxidation and pyrolysis is shown in Fig. 3-1. Here, we describe the synthesis of the CoPHPS1/8 sample which is well representative of the synthesis process applied to prepare all polymeric samples. In a typical experiment, a 100 mL two-neck round-bottom flask equipped with a magnetic stirrer was charged with as-received PHPS (5 mL, 20 wt% xylene solution) and toluene (10 mL). $Co(acac)_3$ (1.099 g, Co/Si = 1/8) was added to the solution at room temperature. The mixture was then stirred at room temperature for 2 h followed by heating at 110 °C for additional 12 h to give the single source precursor of Co-modified PHPS (CoPHPS1/8 sample) as a gelatinous compound.

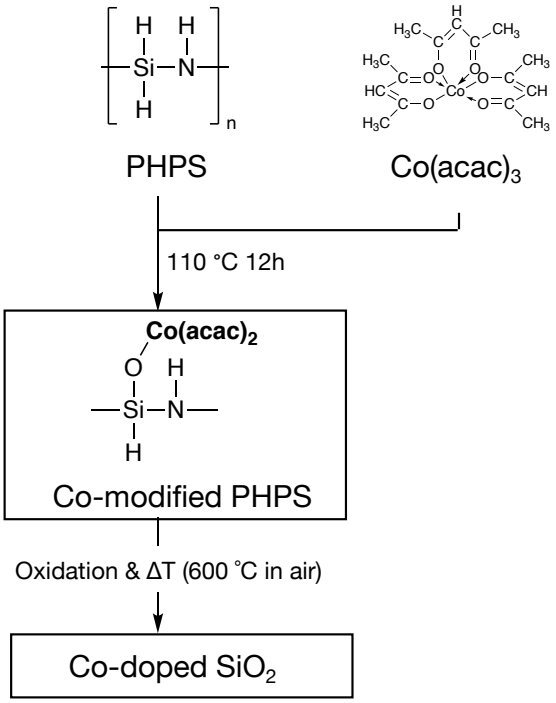

Fig. 3-1 A flowchart of synthesis of Co-modified PHPS and subsequent oxidation at 600 °C in Air.

3.2.2 Conversion to Co-doped amorphous silica

To avoid the vigorous oxidation reaction during the pyrolysis at high temperature, the Co-modified PHPS samples were oxidized at room temperature as follows: after cooling down to room temperature, the reaction mixture was poured into an aluminum tray, and rinsed with acetone, then dried at room temperature. To proceed further oxidation, the dried residue was exposed to a vapour from aqueous NH_3 at room temperature for 24 h according to the previously reported procedure [22, 23]. The resulting solid precursor was ground to a fine powder using a mortar and pestle, then placed in a quartz boat and heat-treated in an electric muffle furnace (Model FUW220PA, Advantec Toyo Kaisha, Ltd., Chiba Japan) under flowing air by heating from room temperature to 600 °C in 6 h, maintaining the temperature at 600 °C for an additional 1 h, and finally furnace cooling down to room temperature to afford Co-doped amorphous SiO_2 samples labeled as **CoSiO1/8**; **CoSiO1/20**; **CoSiO1/40** and **CoSiO1/80**, respectively.

3.2.3 Characterizations

The Attenuated Total Reflection-Infrared (ATR-IR) spectra were recorded on the as-received $Co(acac)_3$, as-received PHPS and chemically modified PHPSs (CoPHPS1/8, CoPHPS1/20, and CoPHPS1/40) with a diamond prism under an incidence angle of 45° (Model Spectrum 100, Perkin Elmer, Waltham, MA, USA).

To study the effect of Co^{2+}-doping on hydrogen transport property at the amorphous SiO_2 surface, hydrogen (H) / deuterium (D) isotope exchange in the surface silanol groups (Si–OH/OD conversion) of the polymer-derived Co-doped amorphous SiO_2 was monitored in-situ by measuring IR absorption spectroscopy adopted diffuse reflectance infrared Fourier transform spectroscopy (DRIFTS) technique (Model Spectrum 100, Perkin Elmer, Waltham, MA, USA) according to the following procedure: the Co-doped SiO_2 sample was placed within a diffuse reflection cell (Model STJ900C Diffuse IR Heat Cham, S.T. JAPAN Inc., Tokyo, Japan), and subjected to pre-drying to remove adsorbed water at 500 °C for 20 h under flowing argon (Ar, 4 mL min^{-1}). The sample was subsequently heat-treated at 500 °C for an additional 3 h under flowing hydrogen (H_2, 4 mL min^{-1}), then the initial IR spectrum was recorded. Then, under flowing 10% deuterium (D_2) /Ar (4 mL min^{-1}) at 500 °C, the Si–OH/OD conversion was monitored in-situ by measuring DRIFT spectra at a specific time interval of 1, 5, 10, 20, 30, 60, 90, 120, 150 and 180 min. After the background noise removal, the normalized absorption band intensity in each DRIFT spectrum was calculated by shifting the whole spectrum to make the peak intensity at 4000 cm^{-1} zero. Then, the time dependence on the absorption band intensities of free deuteroxyl (Si–OD) and D-bonded Si–OD in DRIFT spectra were examined.

Elemental analyses for oxygen, nitrogen and hydrogen (inert-gas fusion method, Model EMGA-930, HORIBA, Ltd., Kyoto, Japan), and carbon (non-dispersive infrared method, Model CS844, LECO Co., St Joseph, MI, USA) were performed for the Co-doped and non-doped SiO_2 samples. The Co content in the Co-doped SiO_2 samples were analyzed by the energy dispersive X-ray spectroscopy (EDS) mounted on a scanning electron microscope (SEM, Model JSM-6010LA, JEOL Ltd., Tokyo, Japan), and evaluated as Co/Si atomic ratio.

Particle size distribution of the samples after heat-treatment in air at 600 °C was characterized by the laser diffraction/scattering method (Model 7995-10 SPA, Nikkiso Co., Ltd., Tokyo, Japan).

X-ray diffraction (XRD) measurement was performed on the 600 °C heat-treated samples (Model X'pert Pro α1, Philips Ltd., Amsterdam, The Netherlands).

X-ray photoelectron spectroscopic (XPS) analysis was performed on the heat-treated

samples (Model PHI-5000, Ulvac-phi, Kanagawa, Japan). The photoelectron binding energy was referenced to the C 1s peak (at 284.8 eV) of unavoidable carbon. The peak intensity was normalized by dividing all intensity at each spectrum to the peak intensity of oxygen 1s in the spectrum.

Transmission electron microscope (TEM) observations and high-angle annular dark-field-scanning transmission electron microscope (HAADF-STEM) observations were performed on the heat-treated powder samples (**CoSiO1/20** and **CoSiO1/8**) in a JEOL JEM-ARM200F operated at an accelerating voltage of 200 kV. The size of the electron probe was approximately 0.1 nm. The convergent angle and the detector collection angle were 22 mrad and 68-280 mrad, respectively. Analytical investigations were carried out by electron energy loss spectroscopy (EELS) using a Gatan Quantum ERS with an incident-electron beam-energy of 200 keV.

Table 3-1 D_{50} of polymer-derived non-doped and Co-doped SiO_2 samples.

Sample	SiO_2	SiCo801	SiCo401	SiCo201	SiCo81
D_{50} [mm]	20.10	21.50	20.44	23.46	23.30

3.3 Results and Discussion

3.3.1 Synthesis of cobalt cation-doped amorphous silica

3.3.1.1 Chemical structure of Co-modified PHPS

Typical ATR-IR spectra of Co-modified PHPS samples (CoPHPS1/8, CoPHPS1/20 and CoPHPS1/40) were compared with those recorded for PHPS and $Co(acac)_3$ shown in Fig. 3-2. As-received PHPS exhibits absorption bands at 2152 cm^{-1} (νSi–H), 1175 cm^{-1} (δN–H) and 832 cm^{-1} (δSi–N–Si) [24]. As-received $Co(acac)_3$ presented absorption bands correspond to the ligand acetylacetonate (acac) at 1573 cm^{-1} (C=O) and 1518 cm^{-1} (C=C) [25]. In addition to the characteristic absorption bands attributed to the Si–H, N–H and Si–N–Si of PHPS, Co-modified PHPS samples exhibit a new absorption band around 930 cm^{-1} assigned to Si–O–Co (Fig. 3-2b) [26]. Moreover, the following changes in the spectra are detected: A new absorption band appears around 1110 cm^{-1} assigned to C–N bond [27], the C–N band intensity increased with increasing the Co/Si atomic ratio. Oppositely, the Si–H band intensity decreased with increasing the Co/Si atomic ratio. The CoPHPS1/8 sample presented absorption bands attributed to the C=O and C=C of the acac ligand. However, the detected C=O band became broader and shifted toward higher wavenumber, which suggested that the electron density of a

certain number of the C=O double bond increased as a result of Si–O–Co bond formation.

Based on the results obtained by the FTIR spectroscopic analysis, a possible reaction scheme for the present chemical modification of PHPS with $Co(acac)_3$ has been suggested as shown in Fig. 3-3: the nucleophilic conjugate addition of N–H group in PHPS to acac ligand of $Co(acac)_3$ led to the formation of enamine derivative (**1**) associated with elimination of $(acac)_2Co$-OH (**2**). Subsequently, Si–O–Co bond formation proceeded via dehydrocoupling reaction between Si–H group in PHPS and the $(acac)_2Co$–OH formed in-situ to give the Co-modified PHPS represented by a series of four precursors labeled as CoPHPS1/8, CoPHPS1/20, CoPHPS1/40 and CoPHPS1/80.

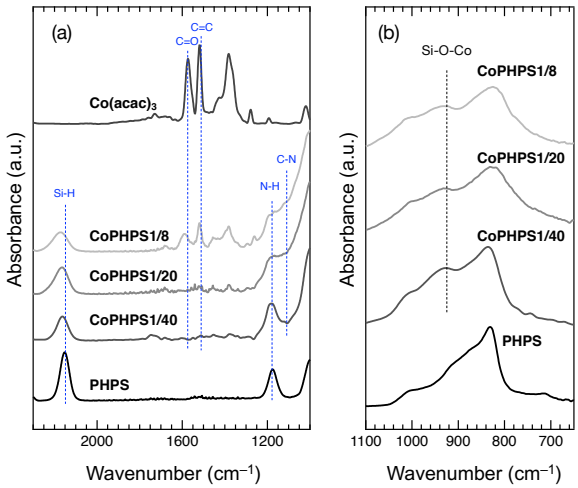

Fig. 3-2 ATR-IR spectra for as-received PHPS, $Co(acac)_3$ and typical Co-modified PHPS samples (CoPHPS1/8, CoPHPS1/20 and CoPHPS1/40 samples): 2300 to 1000 cm^{-1} and (b) 1100 to 650 cm^{-1}.

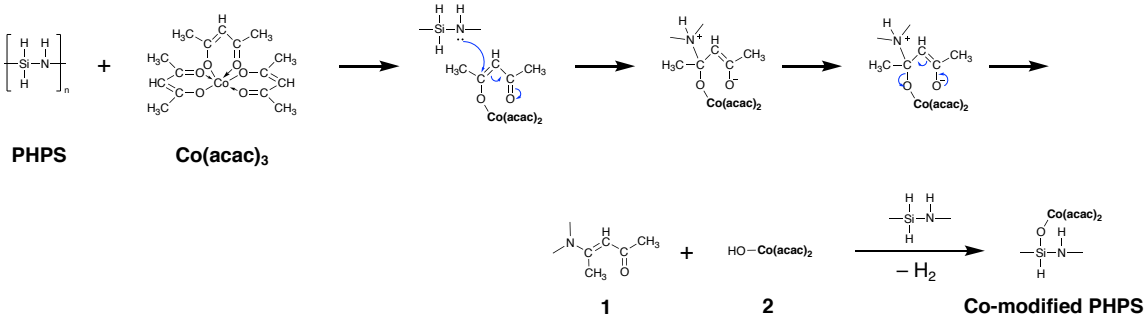

Fig. 3-3 Possible reaction scheme suggested for the chemical modification of PHPS with $Co(acac)_3$.

3.3.1.2 Conversion to Co-doped amorphous silica

As-synthesized precursors were heat-treated at 600 °C in air to form the titled samples labeled as **CoSiO1/8**, **CoSiO1/20**, **CoSiO1/40** and **CoSiO1/80**. Table 3-1 lists the chemical compositions of the polymer-derived samples after the heat-treatment in air at 600 °C. The measured Co/Si atomic ratios of the heat-treated samples were well controlled as fixed at the polymer level, except for the **CoSiO1/8** sample, which is measured to be 0.18, higher than the calculated value (0.13) used for the single source precursor synthesis. One possible reason for the higher Co/Si ratio is due the side reaction [28]: with increasing amount of alcohol derivative to modify PHPS, Si–N bond cleavage tends to proceed which lowers the polymer to inorganic compound conversion yield due to the volatilization of low molecular weight silazane species formed by the Si–N cleavage during pyrolysis up to 600 °C. As a result, Si content in the Co-doped SiO_2 decreased, i.e., Co/Si ratio became larger than the nominal one. The residual C and N in the pyrolyzed samples were less than 0.2 and 0.3 wt%, respectively. The combination of the FTIR and elemental analysis results revealed that i) the chemical modification of PHPS occurred via the formation of Si–O–Co bridges in the derived polymers composed of Si, C, N, O, H and Co and ii) the heat-treatment in air at 600 °C completed the oxidative cross-linking of the polymer to form ternary ceramics only composed of Si, O and Co elements.

Table 3-1 Chemical composition of polymer-derived samples after heat-treatment at 600 °C in air.

Sample	Co/Si ratio (-)		Content (wt%)		
	Calc.	Obs.	Carbon	Nitrogen	Oxygen
CoSiO1/80	0.01	0.01	0.15	0.07	45.46
CoSiO1/40	0.03	0.03	0.07	0.00	37.74
CoSiO1/20	0.05	0.05	0.00	0.20	41.95
CoSiO1/8	0.13	0.18	0.07	0.24	32.37

Heat-treated samples were found as X-ray amorphous as shown through the XRD patterns of the four investigated ceramic samples (Fig. 3-4(a)). In order to investigate the oxidation state of the Co-doped SiO_2 samples, XPS has been applied. The results are shown in Fig. 3-4(b). Consistently with the analytical Co/Si atomic ratio from 0.01 (**CoSiO1/80** sample) to 0.05 (**CoSiO1/20** sample), a broad peak centered at 782 eV increased in intensity. This peak was assigned to Co^{2+} [29]. At the Co/Si atomic ratio of 0.18 (**CoSiO1/8** sample), another broad peak appeared at around 788 eV correspond to a Co^{2+} satellite peak (labeled * in the graph), while those due to Co^{3+} (779.9 eV) and metallic-Co (777.8 eV) [30] were not observed. In this study,

the Co modification to PHPS has been performed at the molecular level via the formation of Si–O–Co bridge. Thus, Co species are highly dispersed within the Co-doped amorphous SiO_2 as shown in XRD patterns (Fig. 3-4(a)). These results reveal that crystallization of Co species is suppressed to afford Co^{2+}-modified amorphous SiO_2 through the PDCs route investigated in this study.

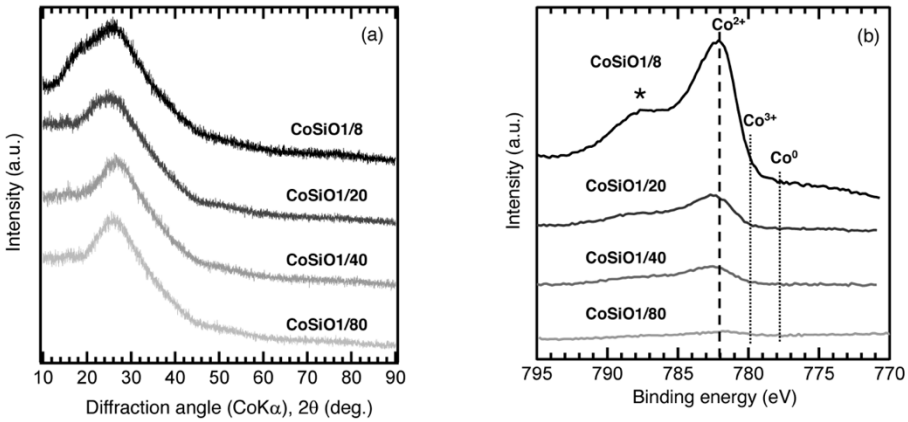

Fig. 3-4 (a) XRD patterns and (b) XPS spectra of polymer-derived Co-doped amorphous silica samples.

To investigate the bonding state of the sample surface, DRIFT spectra were recorded and shown in Fig. 3-5. As shown in Fig. 3-5(a), the DRIFT spectrum of as-synthesized amorphous SiO_2 presented a very broad absorption band around 3400 cm^{-1} due to adsorbed water. In order to remove the adsorbed water and to construct the surface conditions of hydrogen transport at high temperature (500°C) [20], an additional heat treatment was performed at 500 °C for 20 h under an Ar flow within the DRIFTS chamber. When the adsorbed water was removed, the spectrum presented one distinct peak at 3732 cm^{-1} assigned to Si–OH group (Fig. 3-5(b)) [31, 32]. As a typical result, the DRIFTS of **CoSiO1/80** sample after the dehydration treatment at 500 °C is shown in Fig. 3-5(c). In addition to the sharp adsorption band assigned to free Si–OH at 3733 cm^{-1}, the spectrum exhibited a broad absorption band around 3690 cm^{-1} attributed to hydrogen (H)-bonded Si–OH groups [33, 34]. Such a broad absorption band was observed for all the Co-doped amorphous SiO_2 samples (Fig. 3-6). This indicates that the divalent Co^{2+} cation modifies the amorphous SiO_2 network to form H-bonded silanol as shown in Fig. 3-5(d).

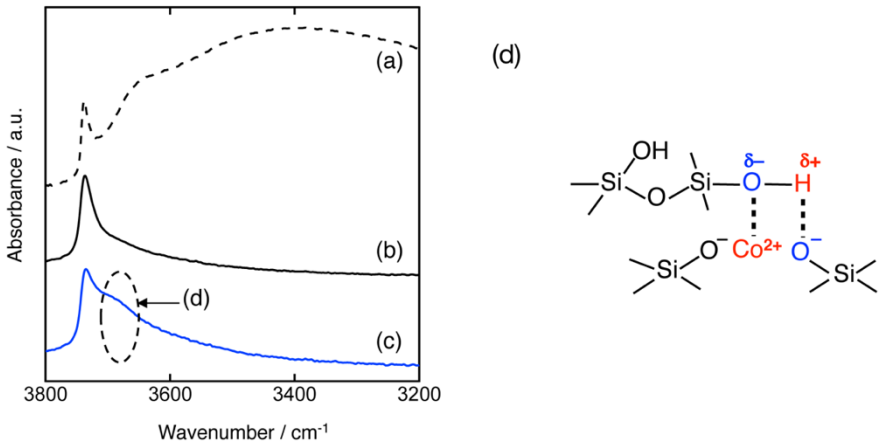

Fig. 3-5 DRIFT spectra measured in-situ for PHPS-derived amorphous SiO_2, (a) as-synthesized, (b) after dehydration treatment at 500 °C in vacuum, and (c) Co-doped amorphous SiO_2 (**CoSiO1/20** sample) after dehydration treatment at 500 °C in Ar, which suggested (d) formation of hydrogen bond in the Co^{2+}-doped amorphous silica around 3690 cm^{-1}.

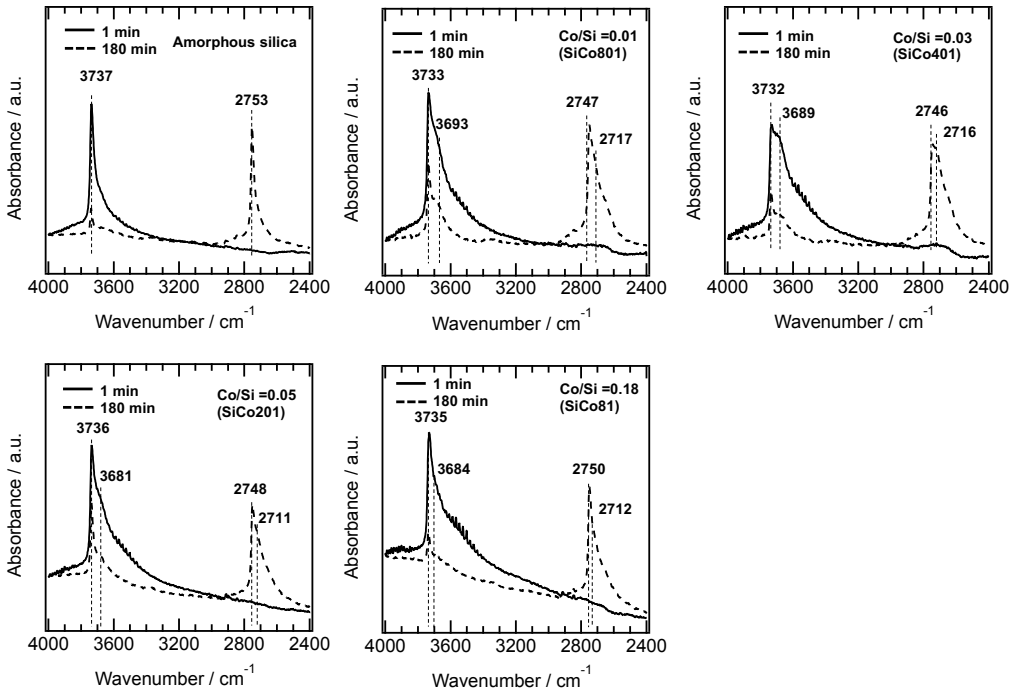

Fig. 3-6 Si–OH/OD conversion of amorphous silica and Co-doped amorphous silica monitored in-situ by measuring DRIFT spectra under 10%D_2/Ar flow at 500 ºC.

3.3.2 Si–OH/OD conversion behaviors

To study the hydrogen transport property, OH/OD conversion behaviors were studied for free Si–OH and H-bonded Si–OH, respectively. After the dehydration treatment at 500 °C, DRIFT spectra were recorded for all the samples at 500 °C under a 10%-D_2/Ar flow at the specific time interval from 1 to 180 min. Figure 3-7(a) shows DRIFT spectra for the non-doped amorphous SiO_2 measured as a reference sample. Consistently with the D_2 exposure time, the intensity of the absorption band due to the free Si–OH at 3732 cm^{-1} decreased, while a new band at 2752 cm^{-1} increased in intensity. After 180 min, the new band became dominant.

Based on the detected wavenumbers of ν_{OH} and ν_{new} as ν_{OD}, the isotope shift factor (i) was evaluated:

$$i = \frac{\nu_{\mathrm{OH}}}{\nu_{\mathrm{new}}} = \frac{\nu_{\mathrm{OH}}}{\nu_{\mathrm{OD}}} \qquad (3\text{-}1)$$

The experimental i value was 1.356 and well consistent with the literature data (1.35-1.36) [35]. Thus, the new band was assigned to deuteroxyl (Si–OD). In addition to the free Si–OH, the OH/OD conversion for H-bonded Si–OH was successfully monitored for all the Co-doped samples (Fig. 3-6). As a typical result, the DRIFT spectra for **CoSiO1/20** sample were shown in Fig. 3-7(b). As listed in Table 3-3, the i values evaluated for the free Si–OH and the H-bonded Si–OH were in the range of 1.356 to 1.360, and they were also compatible with the above-mentioned literature data [35].

The OH/OD conversion behaviour was further assessed by the self-diffusion coefficient of deuterium evaluated according to the procedure reported by Fishman et al. [36, 37]. The following equation based on Fick's second law has been derived in order to estimate the diffusion coefficient for the ^{18}O and ^{16}O exchange in oxide-ion conductors:

Table 3-3 OH/OD isotopic shift factor and wavenumber conversion for non-doped and Co-doped amorphous SiO_2 synthesized in this study.

Co-doped SiO_2 Analytical Co/Si ratio (-)	Wavenumber (cm^{-1})				Isotopic shift factor, i	
	Free OX		X-bonded OX		Free	H-bonded
	OH	OD	OH	OD		
0	3737	2753	-	-	1.357	-
0.01	3733	2747	3693	2717	1.359	1.359
0.03	3732	2746	3689	2716	1.359	1.358
0.05	3736	2748	3681	2711	1.360	1.358
0.18	3735	2750	3684	2712	1.358	1.358

$$c(t,r) = c_0\left(1 - \frac{6}{\pi^2}\sum_{n=1}^{\infty}\frac{1}{n^2}\cdot\exp\left(-\left(\frac{n\pi}{r}\right)^2\cdot D\cdot t\right) + 3\cdot\frac{\Delta}{r}\right) \qquad (3\text{-}2)$$

where D (m^2 s^{-1}) is self-diffusion coefficient; r (m) is the particle radius; c (at%) is the ^{18}O concentration, c_0 (at%) is the ^{18}O concentration of the sample oxide equilibrium to the ^{18}O atmosphere; Δ(m) is the monolayer thickness; t (s) is the isothermal annealing time.

In general, the surface diffusion coefficient of oxygen is much higher than the volume diffusion coefficient. For instance, in the case of $LaMnO_{3+\delta}$ perovskite, it was found that surface diffusion coefficient and volume diffusion coefficient were in the order of ~10^{-17} m^2 s^{-1} and ~10^{-24} m^2 s^{-1}, respectively [37]. In this modelling expressed by the Eq. (3-2), the summation was performed for running indices up to n = 5. This model can be applied for a very fast exchange on the surface of an oxide particle, whereby Δ is around 0.5 nm for typical oxides [38].

Present study as well, self-diffusion coefficient (D) was adopted as an index of Si–OH/OD conversion rate on the non-doped and Co-doped amorphous SiO_2 surface. The D values were evaluated for the free Si–OH and the H-bonded Si–OH and were denoted as D(Free) and D(H-bonded), respectively. The D values were estimated by detecting OD generated by exchange

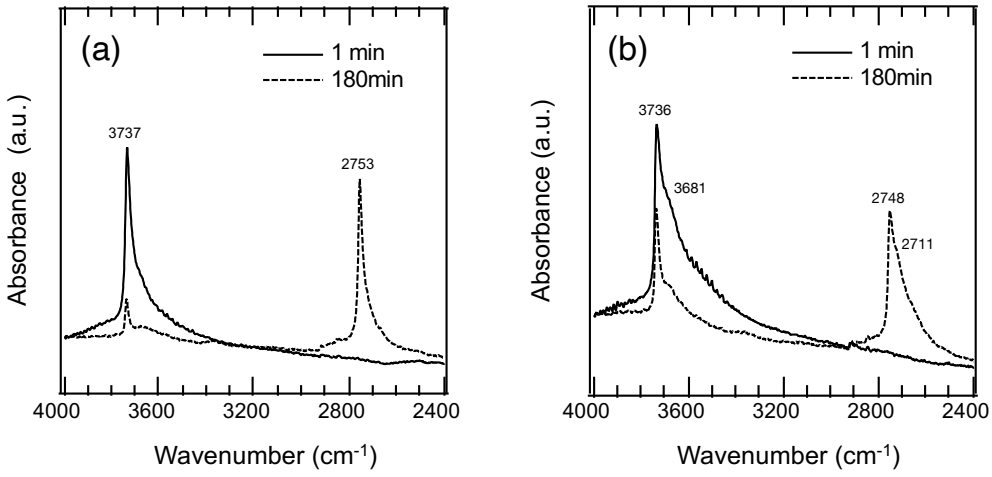

Fig. 3-7 Si–OH/OD conversion behavior of (a) non-doped and (b) Co-doped amorphous SiO_2 with analytical Co/Si = 0.05 (**CoSiO1/20** sample) monitored in-situ by measuring DRIFT spectra under 10%D_2/Ar flow at 500 °C.

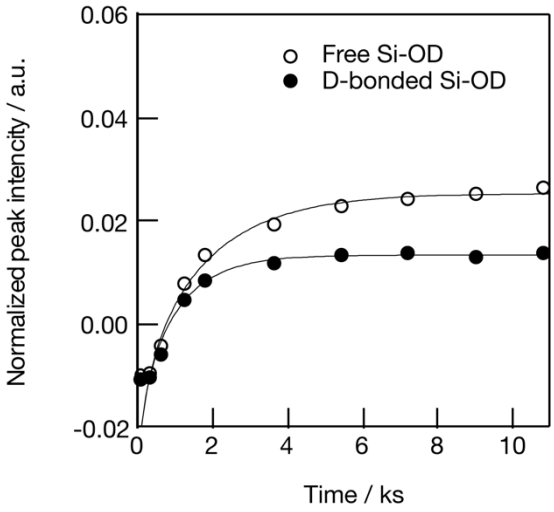

Fig. 3-8 Si–OH/OD conversion of Co-doped amorphous silica with analytical Co/Si =0.05 (**CoSiO1/20** sample).

Table 3-4 Deuterium diffusion coefficient at the surface (D) and $c_{D\,eq}$ for polymer-derived amorphous silica and Co-doped amorphous silica synthesized in this study.

Co-doped SiO_2 Analytical Co/Si ratio (-)	D (10^{-15} m^2 s^{-1})		$c_{D\,eq}$ (10^{-2} at%)	
	Free	H-bonded	Free	H-bonded
0	6.1	-	9.5	-
0.01	3.2	4.8	4.9	3.5
0.03	5.3	7.9	4.0	3.7
0.05	7.6	15.6	5.8	6.3
0.18	5.5	9.1	5.1	4.1

on the surface Si–OH group by DRIFTS analysis, and c_0 in this study was renamed as $c_{D\,eq}$ (the equilibrium deuterium concentration of the sample). Moreover, in this isotope exchange reaction, the monolayer (Δ) had a nanometer scale thickness, while the radius of the sample particle synthesized in this study had an approximately 10 μm (one half of D_{50} in Table 3-1), thus the Eq. (3-3) with assuming $r >> 3\,\Delta$ in the Eq. (3-2) was employed:

$$c(t,r) = c_{D\,eq}\left(1 - \frac{6}{\pi^2}\sum_{n=1}^{5}\frac{1}{n^2}\cdot\exp\left(-\left(\frac{n\pi}{r}\right)^2\cdot D\cdot t\right)\right) \qquad (3\text{-}3)$$

Time dependence on the absorption band intensities of free Si–OD and D-bonded Si–OD in DRIFT spectra were fitted to the non-linear curve by the Eq. (3-3) using r as one half of D_{50} listed in Table 3-1 with two free parameters, D and $c_{D\,eq}$.

As typical results, Fig. 3-8 presents the D_2 gas exposure time dependence of the absorption band intensity evaluated for the free Si–OD and the D-bonded Si–OD in **CoSiO1/20** sample.

Each fitted line described the experimental data very well, which suggesting OH/OD conversions for both the free and H-bonded Si–OH investigated in this study were diffusion controlled. Under the same manner, the D and $c_{\mathrm{D\,eq}}$ were evaluated for both free and H-bonded Si–OH in the Co-doped amorphous SiO_2 samples (Fig. 3-9), and the results are listed in Table 3-4. As shown in Fig. 3-10, the D(H-bonded) exponentially increased with the Co/Si atomic ratio and reached maximum at the Co/Si = 0.05, then decreased with increasing the Co/Si atomic ratio. The D(Free) also exhibited a similar dependency on the Co/Si atomic ratio, however, at all the Co/Si atomic ratios, the D(H-bonded) was higher than D(Free). This suggests that the polar H-bonded Si–OH bonds formed with the doped Co^{2+} accelerate OH/OD conversion rate.

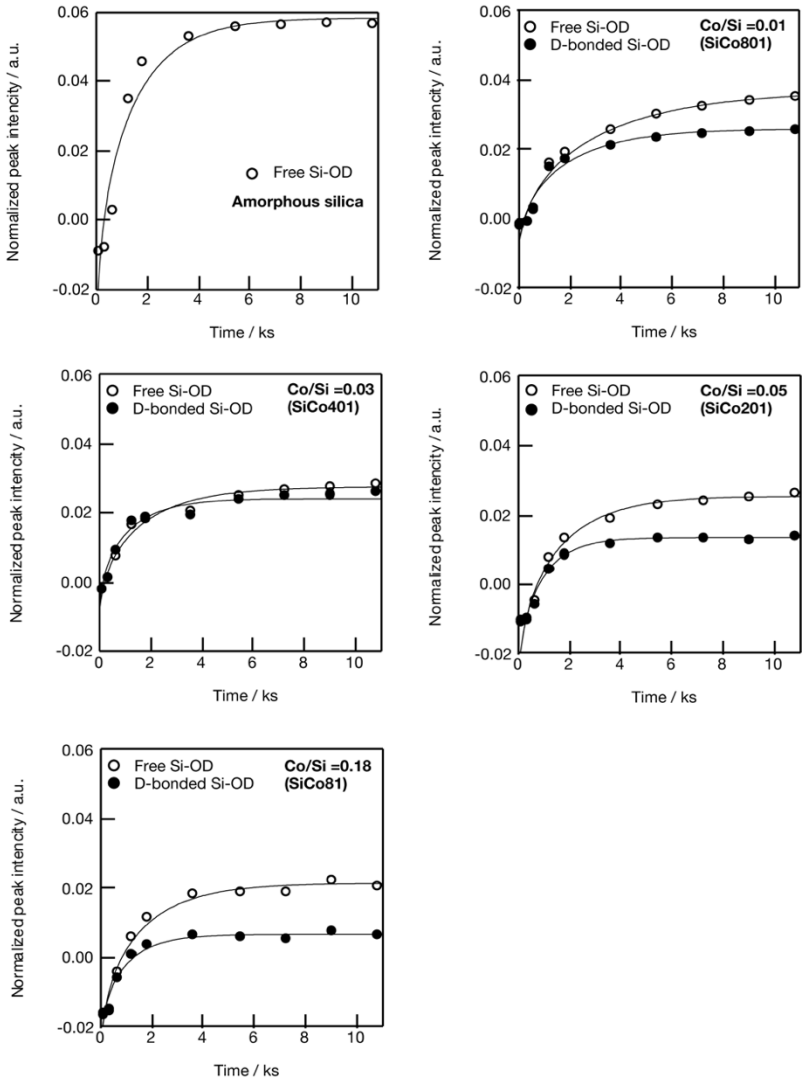

Fig. 3-9 OH/OD conversion for surface silanol groups of non-doped and Co-doped amorphous silica.

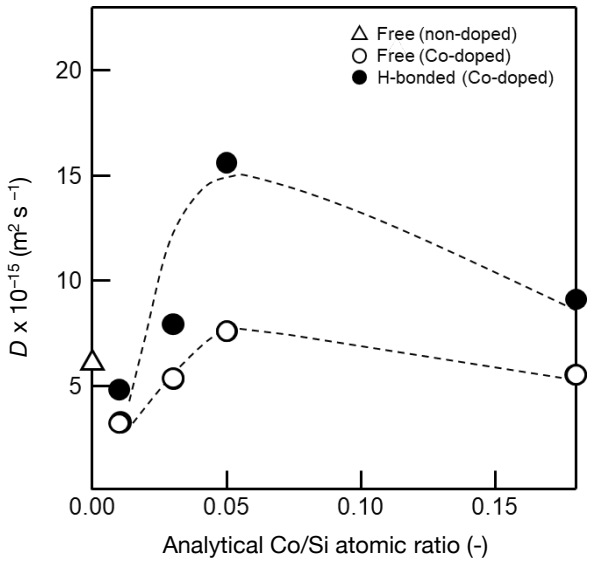

Fig. 3-10 Co/Si atomic ratio dependence of the deuterium surface diffusion coefficient, *D*.

To examine the Co/Si atomic ratio dependency of the *D* in more details, TEM observations were performed on the samples with measured Co/Si = 0.05 (**CoSiO1/20** sample) and 0.18 (**CoSiO1/8** sample). The results are shown in Figs. 3-11 and 3-12, respectively. **CoSiO1/20** and **CoSiO1/8** samples were X-ray amorphous (Fig. 3-4(a)), and the selected area electron diffraction patterns shown in Figs. 3-11(a) and 3-12(a) supported the amorphous state of these materials. However, **CoSiO1/20** samples sample exhibited some spots with darker contrast less than approximately 2 nm in size (Fig. 3-12(b)), and the size of the spots observed for the **CoSiO1/8** sample was larger (Fig. 3-12(b)). As shown in Fig. 3-13(a), the **CoSiO1/20** sample exhibited a narrow and unimodal spot size distribution, and the mean size was determined as 1.8 nm. On the other hand, the **CoSiO1/8** sample showed a wider size distribution with a larger mean size of 3.4 nm (Fig. 3-13(b)). Then, STEM observation was performed for further analysis of the spots. The darker spots observed in the bright field (BF)-images (Figs. 3-11(c) and 3-12(c)) were highlighted with bright contrast in the annular dark-field (ADF)-STEM images (Figs. 3-11(d) and 3-12(d)), and the simultaneous electron energy loss spectroscopy (EELS) analysis for the spots shown in Fig. 3-12(d) resulted in the detection of Co^{2+} as indicated by the Co L_{III}/L_{II} EELS ratio of ~2 (Fig. 3-12(e)). This oxidation state of Co was well consistent with the result obtained by the XPS analysis (Fig. 3-4(b)).

To study on the Co(II)-cluster formation in more details, HRTEM observation was performed on the samples with lower Co/Si ratio below 0.05. However, these samples exhibited featureless nanostructures. Then, intensive STEM observation was performed. As a result, **CoSiO1/80** sample exhibited a trace amounts of bright spots with a size of about 1-2 nm under the ADF-STEM imaging mode (Fig. 3-14). In the case of **CoSiO1/40** sample, it was also rare to find some spots suggested as Co(II)-cluster approximately 2 nm in size (Fig. 3-15).

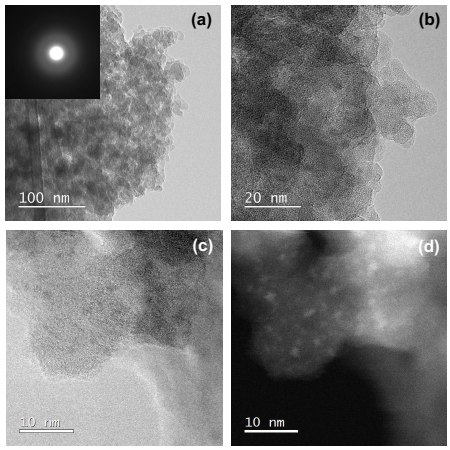

Fig. 3-11 Nanostructure observation of Co-doped amorphous silica with measured Co/Si = 0.05 (**CoSiO1/20** sample). (a) TEM image and SAED pattern obtained from the image, (b) high-magnification TEM image (c) BF-STEM image and (d) ADF-STEM image.

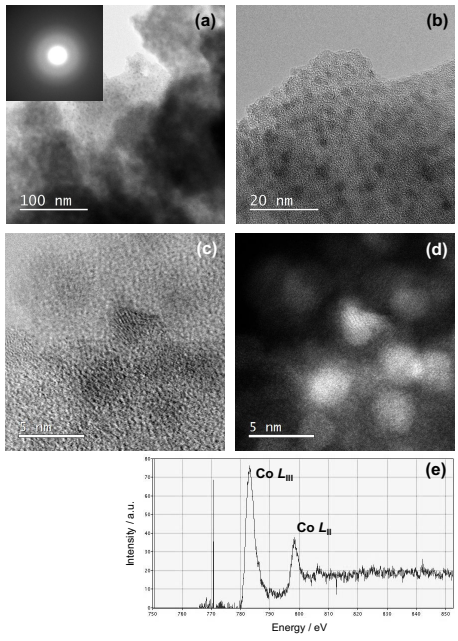

Fig. 3-12 Nanostructure observation of Co-doped amorphous silica with measured Co/Si = 0.18 (**CoSiO1/8** sample). (a) TEM image and SAED pattern obtained from the image, (b) high-magnification TEM image (c) BF-STEM image, (d) ADF-STEM image and (e) EELS characterization for the spot with bright contrast in (d).

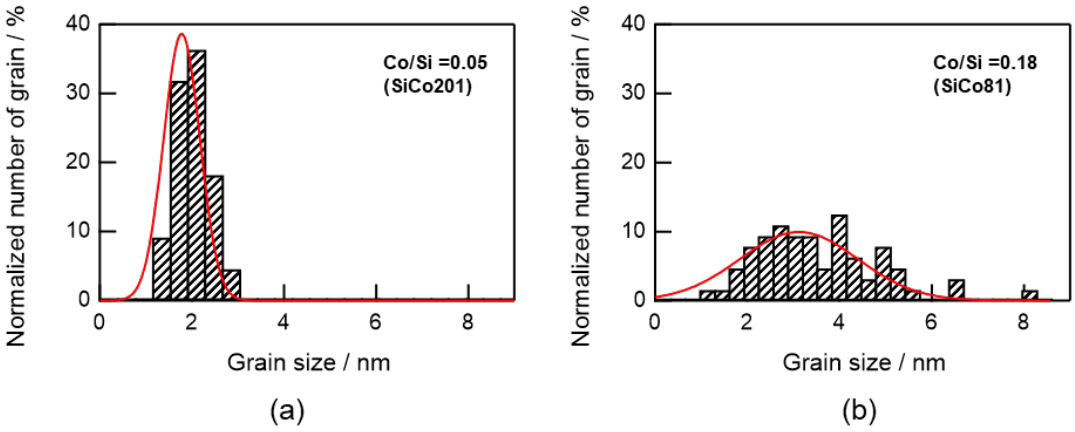

Fig. 3-13 The size distribution of Co-species within the amorphous silica-based matrix characterized for the Co-doped amorphous silica with the analytical Co/Si atomic ratio of (a) 0.05 (**SiCo201** sample) and (b) 0.18 (**SiCo81** sample).

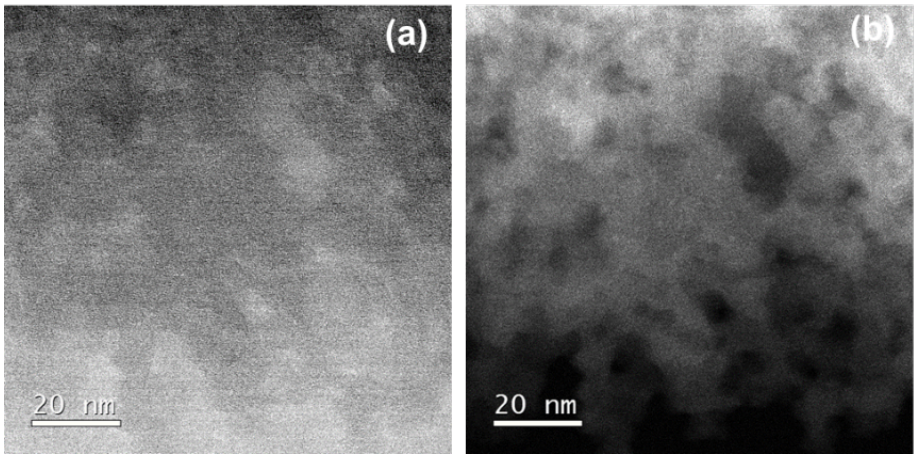

Fig. 3-14 Nanostructure observation of Co-doped amorphous silica with Co/Si = 0.01 (**CoSiO1/80** sample). (a) BF-STEM image and (b) ADF-STEM image.

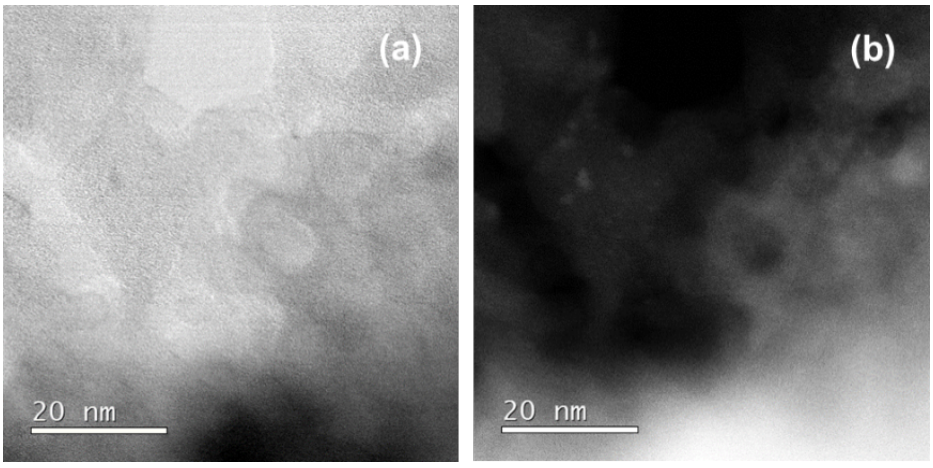

Fig. 3-15 Nanostructure observation of Co-doped amorphous silica with Co/Si = 0.03 (**CoSiO1/40** sample). (a) BF-STEM image and (b) ADF-STEM image.

As shown in Fig.3-10, H-bonded Si–OH groups played key role for the acceleration of the OH/OD conversion rate. Since the parameter of $c_{D\,eq}$ reflects the number of the Si–OH which is converted to the Si–OD at the sample surface, D values are plotted as a function of $c_{D\,eq}$ (Fig. 3-16). Consistently with the $c_{D\,eq}$, the D(H-bonded) apparently increased, which indicated that the increase of the number of H-bonded Si–OH accelerated the OH/OD conversion rate of Co^{2+}-doped amorphous SiO_2. Moreover, as shown in Fig. 3-17, the wavenumber of the H-bonded OH (ν(OH)/cm^{-1}) in the Co-doped SiO_2 samples detected by the IR spectroscopic analysis (Table 3-3) decreased consistently with $c_{D\,eq}$, i.e., the acidity (polarity) of the H-bonded OH increased with $c_{D\,eq}$.

As mentioned above, in the case using conventional sol-gel technique for the synthesis of Co-doped SiO_2, Co_3O_4 crystallization easily proceeds to afford binary Co_3O_4-SiO_2 composite [19, 20]. In the present study, amorphous Co(II)-nanocluster formation proceeds to some extent, however, at the Co/Si ratios ranging from 0.01 to 0.05, the concentration of Co^{2+} which modified amorphous SiO_2 matrix network increases, i.e., the number of hydrogen bonds by the doped-Co^{2+} (Si-$O^{\delta-}H^{\delta+}$···O-Co^{2+} shown in Fig. 3-5) increases consistently with the Co/Si ratio. This relation has been successfully achieved through the present PDCs route: during the

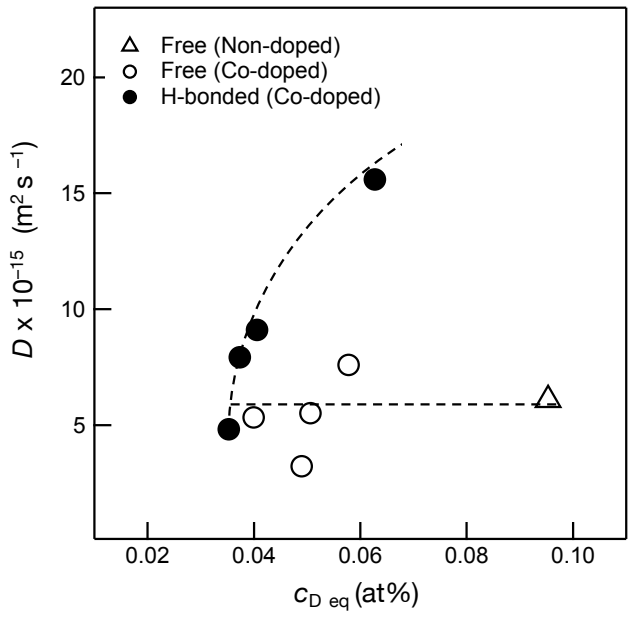

Fig. 3-16 $c_{D\,eq}$ dependence of deuterium surface diffusion coefficient, D.

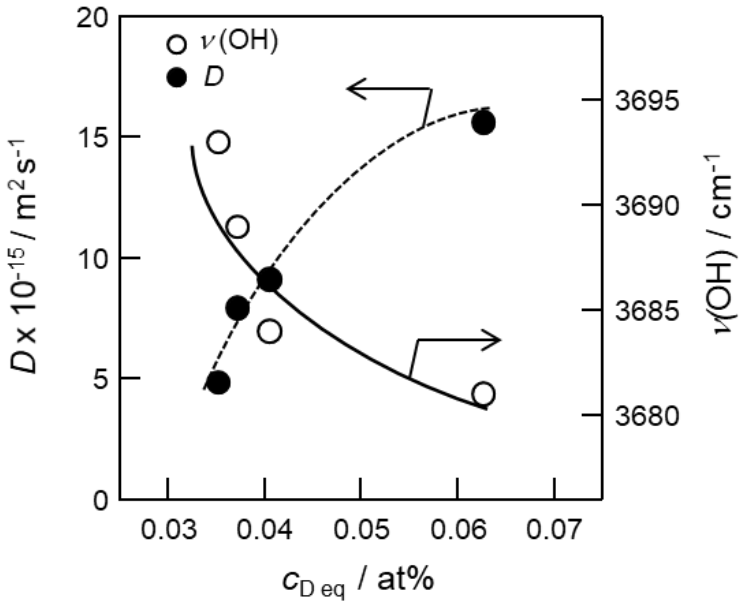

Fig. 3-17 $c_{D\,eq}$ dependence of ν(OH) of the H-bonded Si–OH detected by FTIR spectroscopic analysis in comparison with that of *D* (H-bonded).

thermal conversion of polymer to inorganic compound, the molecular structure having the Si-O-Co bond is preserved to afford Co^{2+}-induced H-bonded OH group within the amorphous SiO_2 matrix.

Recently, Nogami et al. reported the hydrogen diffusion coefficient through sodium aluminosilicate glasses (Na_2O-Al_2O_3-SiO_2) prepared by the melt-quenching technique [39]. The diffusion coefficients of hydrogen at 400-600 °C estimated for this glass with Al/Na atomic ratio < 1 were 10^{-16}-10^{-15} m^2 s^{-1} order, as a typical example, the diffusion coefficient at 500 °C estimated for $20Na_2O{\cdot}10Al_2O_3{\cdot}70SiO_2$ glass was 1.8×10^{-15} m^2 s^{-1} [39]. In this study, as listed in Table 4, the *D*(Free) at 500 °C estimated for non-doped amorphous SiO_2 was 6.1×10^{-15} m^2 s^{-1}. This value was compatible with the reported value, while the *D*(H-bonded) value of 15.6 $\times 10^{-15}$ m^2 s^{-1} was approximately one order of magnitude higher than the reported value. Generally, SiO_2-based materials for gas separation membranes are composed of microporous looser amorphous network which can exhibit molecular sieve property. Thus, hydrogen can permeate through the micropore channels within the amorphous SiO_2, which is recognized as activated diffusion [3]. The enhanced value of the *D*(H-bonded) estimated in this study suggests that Co^{2+}-doping can offer an additional hydrogen facilitate transport property at the surface of micropore channel wall composed of the Co-doped amorphous SiO_2, i.e., enhancing hydrogen permeance via the surface diffusion mechanism even at the high temperature of 500 °C. Alternatively, applications up to 300 °C will be also attractive., for instance, hydrogen

separation/purlificaton process for the dehyderogenation of chemical hydrides [40, 41] under the reduced condition in the novel hydrogen storage-transportation systems. Further study on the evaluation of membrane performance as well as lifetime of the Co-doped amorphous SiO_2 are under progress.

3.4 Conclusions

In this study, the effect of local structure of polymer-derived Co-doped amorphous SiO_2 on the hydrogen transport property was intensively studied and the results can be summarized as follows:

(1) Co^{2+}-doped amorphous SiO_2 materials with Co/Si atomic ratios ranging from 0.01 to 0.18 were successfully synthesized through the PDCs route.

(2) The doped Co^{2+} modified amorphous SiO_2 network to afford H-bonded Si–OH. The number of the H-bonded Si–OH increased consistently with the amount of the doped Co^{2+} and reached maximum at the Co/Si atomic ratio of 0.05, then decreased with increasing the Co/Si atomic ratio above 0.05.

(3) HRTEM and STEM analyses revealed that the segregation of Co^{2+} started at the Co/Si atomic ratio of 0.05, and the amount of Co^{2+} which modified amorphous SiO_2 network deceased with increasing the Co/Si atomic ratio above 0.05.

(4) The OH/OD conversion behavior for surface silanol groups was monitored in-situ by measuring the DRIFT spectra, and the self-diffusion coefficient of deuterium at the sample surface (D) was evaluated. The D(H-bonded) at 500 °C estimated in this study was 15.6×10^{-15} m^2 s^{-1}. This value was approximately one order of magnitude higher than the reported D value at 500 °C estimated for sodium aluminosilicate glass.

(5) It was found that the enhanced polarity of the H-bonded Si–OH formed by the Co^{2+}-doping accelerated the hydrogen transport at the amorphous SiO_2 surface network.

(6) The results obtained in this study suggest that rather small amount of Co^{2+}-doping, expressed as Co/Si atomic ratio of 0.05 is effective for enhancing hydrogen permeance through microporous amorphous SiO_2 membranes at $T \geq 500$ °C.

References

[1] S. Lawal, M. Kanezashi, H. Nagasawa and T. Tsuru, Development of an acetylacetonate-modified silica-zirconia composite membrane applicable to gas separation, *J. Memb. Sci.*, 2020, **599**, 117844.

[2] S. T. Oyama, H. Aono, A. Takagaki, T. Sugawara and R. Kikuchi, Synthesis of Silica Membranes by Chemical Vapor Deposition Using a Dimethyldimethoxysilane Precursor, *Membranes (Basel).*, 2020, **10**, 50.

[3] A. K. Prabhu and S. T. Oyama, Highly hydrogen selective ceramic membranes: Application to the transformation of greenhouse gases, *J. Memb. Sci.*, 2000, **176**, 233–248.

[4] J. C. Diniz Da Costa, G. Q. Lu, V. Rudolph and Y. S. Lin, Novel molecular sieve silica (MSS) membranes: characterisation and permeation of single-step and two-step sol-gel membranes, *J. Memb. Sci.*, 2002, **198**, 9–21.

[5] Y. Iwamoto, Precursors-Derived Ceramic Membranes for High-Temperature Separation of Hydrogen, *J. Ceram. Soc. Japan*, 2007, **115**, 947–954.

[6] S. Kurungot, T. Yamaguchi and S. I. Nakao, Rh/γ-Al_2O_3 catalytic layer integrated with sol-gel synthesized microporous silica membrane for compact membrane reactor applications, *Catal. Letters*, 2003, **86**, 273–278.

[7] K. Akamatsu, T. Murakami, T. Sugawara, R. Kikuchi and S. Nakao, Stable equilibrium shift of methane steam reforming in membrane reactors with hydrogen-selective silica membranes, *AIChE J.*, 2011, **57**, 1882–1888.

[8] K. Akamatsu, Y. Ohta, T. Sugawara, N. Kanno, K. Tonokura, T. Hattori and S. Nakao, Stable high-purity hydrogen production by dehydrogenation of cyclohexane using a membrane reactor with neither carrier gas nor sweep gas, *J. Memb. Sci.*, 2009, 330, 1–4.

[9] K. Akamatsu, Y. Ohta, T. Sugawara, T. Hattori and S. I. Nakao, Production of hydrogen by dehydrogenation of cyclohexane in high-pressure (1-8 atm) membrane reactors using amorphous silica membranes with controlled pore sizes, *Ind. Eng. Chem. Res.*, 2008, **47**, 9842–9847.

[10] K. Akamatsu, T. Tago, M. Seshimo and S. I. Nakao, Long-term stable H_2 production from methylcyclohexane using a membrane reactor with a dimethoxydiphenylsilane-derived silica membrane prepared via chemical vapor deposition, *Ind. Eng. Chem. Res.*, 2015, **54**, 3996–4000.

[11] X. L. Zhang, K. Akamatsu and S. I. Nakao, Hydrogen Separation in Hydrogen-Methylcyclohexane-Toluene Gaseous Mixtures through Triphenylmethoxysilane-Derived Silica Membranes Prepared by Chemical Vapor Deposition, *Ind. Eng. Chem. Res.*, 2016, **55**, 5395–5402.

[12] M. G. Miricioiu, C. Iacob, G. Nechifor and V.-C. Niculescu, High Selective Mixed Membranes Based on Mesoporous MCM-41 and MCM-41-NH2 Particles in a Polysulfone Matrix, *Front. Chem.*, 2019, **7**,332.

[13] Ren and Tsuru, Organosilica-Based Membranes in Gas and Liquid-Phase Separation, *Membranes (Basel).*, 2019, **9**, 107.

[14] Brinker, C.J.; Scherer, G.W. Sol-Gel Science, the Physics and Chemistry of Sol-Gel Processing; Academic Press: Boston, MA, USA, 1990; p. 908. ISBN 0-12-134970-5.

[15] K. Tanaka and Y. Sakata, Present and Future Prospects of Hydrogen Production Process Constructed by the Combination of Photocatalytic H2O Splitting and Membrane Separation Process, *Membrane*, 2011, **36**, 113–121.

[16] K. Miyajima, T. Eda, B. N. Nair, S. Honda and Y. Iwamoto, Hydrothermal stability of hydrogen permselective amorphous silica membrane synthesized by counter diffusion chemical vapor deposition method, *J. Ceram. Soc. Japan*, 2013, **121**, 992–998.

[17] K. Yoshida, Y. Hirano, H. Fujii, T. Tsuru and M. Asaeda, Hydrothermal Stability and Performance of Silica-Zirconia Membranes for Hydrogen Separation in Hydrothermal Conditions., *J. Chem. Eng. JAPAN*, 2001, **34**, 523–530.

[18] M. Kanezashi and M. Asaeda, Hydrogen permeation characteristics and stability of Ni-doped silica membranes in steam at high temperature, *J. Memb. Sci.*, 2006, **271**, 86–93.

[19] R. Igi, T. Yoshioka, Y. H. Ikuhara, Y. Iwamoto and T. Tsuru, Characterization of co-doped silica for improved hydrothermal stability and application to hydrogen separation membranes at high temperatures, *J. Am. Ceram. Soc.*, 2008, **91**, 2975–2981.

[20] S. Fujisaki, K. Hataya, T. Saito, S. Arai, Y. Iwamoto and K. Kuroda, Nanostructural characterizations of hydrogen-permselective Si–Co–O membranes by transmission electron microscopy, *J. Mater. Res.*, 2009, **24**, 372–378.

[21] C. R. Miller, D. K. Wang, S. Smart and J. C. Diniz da Costa, Reversible Redox Effect on Gas Permeation of Cobalt Doped Ethoxy Polysiloxane (ES40) Membranes, *Sci. Rep.*, 2013, **3**, 1648.

[22] T. Kubo and H. Kozula, Conversion of Perhydropolysilazane-to-Silica Thin Films by Exposure to Vapor from Aqueous Ammonia at Room Temperature, *J. Ceram. Soc. Japan*, 2006, **114**, 517–523.

[23] M. N. Mohd Sokri, T. Onishi, Y. Daiko, S. Honda and Y. Iwamoto, Hydrophobicity of amorphous silica-based inorganic-organic hybrid materials derived from perhydropolysilazane chemically modified with alcohols, *Microporous Mesoporous*

Mater., 2015, **215**, 183–190.

[24] M. Mohd Sokri, Y. Daiko, Z. Mouline, S. Honda and Y. Iwamoto, Formation of Micro and Mesoporous Amorphous Silica-Based Materials from Single Source Precursors, *Inorganics*, 2016, **4**, 5.

[25] C. Zhou, C. Fasel, R. Ishikawa, M. Gallei, Y. Ikuhara, S. Lauterbach, H. J. Kleebe, R. Riedel and E. Ionescu, One-pot synthesis of a C/SiFeN(O)-based ceramic paper with in-situ generated hierarchical micro/nano-morphology, *J. Eur. Ceram. Soc.*, 2017, **37**, 5193–5203.

[26] P. J. Launer, *Infrared Analysis of Organosilicon Compounds: Spectra-structureCorrelations, Laboratory for Materials*, Inc. Burnt Hills, New York, 1987.

[27] J. E. Stewart, Vibrational spectra of primary and secondary aliphatic amines, *J. Chem. Phys.*, 1959, **30**, 1259–1265.

[28] Y. Iwamoto, K. Kikuta and S. Hirano, Microstructural development of Si_3N_4 –SiC–Y_2O_3 ceramics derived from polymeric precursors, *J. Mater. Res.*, 1998, **13**, 353–361.

[29] M. A. Langell, M. D. Anderson, G. A. Carson, L. Peng and S. Smith, Valence-band electronic structure of Co3O4 epitaxy on CoO(100), *Phys. Rev. B*, 1999, **59**, 4791–4798.

[30] B.-A. F. Kengne, A. M. Alayat, G. Luo, A. G. McDonald, J. Brown, H. Smotherman and D. N. McIlroy, Preparation, surface characterization and performance of a Fischer-Tropsch catalyst of cobalt supported on silica nanosprings, *Appl. Surf. Sci.*, 2015, **359**, 508–514.

[31] R. W. Silverstein and G. C. Bassler, Spectrometric identification of organic compounds, *J. Chem. Educ.*, 1962, **39**, 546–553.

[32] Z. Mouline, K. Asai, Y. Daiko, S. Honda, S. Bernard and Y. Iwamoto, Amine-functionalized polycarbosilane hybrids for CO2-selective membranes, *J. Eur. Ceram. Soc.*, 2017, **37**, 5213–5221.

[33] C. Pazé, S. Bordiga, C. Lamberti, M. Salvalaggio, A. Zecchina and G. Bellussi, Acidic properties of H-β zeolite as probed by bases with proton affinity in the 118-204 kcal mol-1 range: A FTIR investigation, *J. Phys. Chem. B*, 1997, **101**, 4740–4751.

[34] E. Groppo, C. Lamberti, S. Bordiga, G. Spoto and A. Zecchina, The Structure of Active Centers and the Ethylene Polymerization Mechanism on the Cr/SiO_2 Catalyst: A Frontier for the Characterization Methods, *Chem. Rev.*, 2005, **105**, 115–184.

[35] K. Chakarova, N. Drenchev, M. Mihaylov, P. Nikolov and K. Hadjiivanov, OH/OD isotopic shift factors of isolated and H-bonded surface silanol groups, *J. Phys. Chem.*

C, 2013, **117**, 5242–5248.

[36] A. B. Gizhevskii, A. Y. Fishman, E. A. Kozlov, T. E. Kurennykh, S.A. Petrova, I. S. Trakhtenberg, E. V. Vykhodets, V. B. Vykhodets and R. G. Zakharov, Oxygen Isotope Exchange between Gaseous Phase Enriched with 18O Isotope and Nanocrystal Oxides LaMnO3+δ, obtained by severe plastic deformation, *Defect Diffus. Forum*, 2008, **233**, 273–276

[37] A. Y. Fishman, T. E. Kurennykh, S. A. Petrova, E. V. Vykhodets, V. B. Vykhodets and R. G. Zakharov, Oxygen isotope exchange in nanocrystal oxide powders, *J. Nano Res.*, 2009, **7**, 33–41.

[38] E. Ruiz-Trejo and J. A. Kilner, Oxygen diffusion and proton conduction in $La_{1-x}Sr_xYO_{3-\delta}$, *Solid State Ionics*, 1997, **97**, 529–534.

[39] M. Nogami, V. X. Quang, S. Ohki, K. Deguchi and T. Shimizu, Reduction Mechanisms of Cu^{2+}-Doped Na_2O-Al_2O_3-SiO_2 Glasses during Heating in H_2 Gas, *J. Phys. Chem. B*, 2018, **122**, 1315–1322.

[40] K. Oda, K. Akamatsu, T. Sugawara, R. Kikuchi, A. Segawa and S. I. Nakao, Dehydrogenation of methylcyclohexane to produce high-purity hydrogen using membrane reactors with amorphous silica membranes, *Ind. Eng. Chem. Res.*, 2010, **49**, 11287–11293.

[41] K. Kida, Y. Maeta, T. Kuno and K. Yogo, Hydrogen Purification from Chemical Hydride Using Pure Silica Zeolite Membranes, *Chem. Lett.*, 2017, **46**, 1724–1727.

Chapter 4

Reversible Redox Property of Co(III) in Amorphous Co-doped SiO_2/γ-Al_2O_3 Layered Composites

4.1 Introduction

This chapter describes a unique reversible reducing and oxidizing (redox) property of Co (III) in Co-doped amorphous SiO_2/γ-Al_2O_3 Layered Composites. In the previous chapter the effect of Co(II) in the Co-doped SiO_2 matrix. In this work, Co(III) cations was successfully introduced into SiO_2/γ-Al_2O_3 hetero interface by Fenton reaction during the H_2O_2-catalyzed sol-gel process, which then the effect of Co(III) cations at the SiO_2/γ-Al_2O_3 hetero interface has been discussed aiming to reveal the mechanism of effective enhancement of high-temperature hydrogen-permselectivity of microporous amorphous silica-based membranes. Both the redox property of Co cations and local structural changes at the SiO_2/γ-Al_2O_3 hetero interface are carefully examined based on the in-situ local structural analyses.

In addition to the effect of doped cations in amorphous SiO_2 that improving thermal and hydrothermal stability of amorphous silica as represented in Chapter 3, reactions between H_2 and various metal cations (M^{m+} = Ni^{2+} [1], Fe^{3+} [2], Ce^{4+} [2], Sn^{4+} [2], V^{+5} [3], Cu^{+1} [4], Ag^{+} [4]) in SiO_2 glass have been reported and those offer enhanced or novel functionalities such as tuning of optical or fluorescence properties.

In the SiO_2 glasses, the cations are reduced to lower valence state, whereas protons in the form of hydroxyl are introduced into SiO_2 glasses,

$$2(\text{Si–O–Si})_n\text{–O}^- + 2M^{m+} + H_2 \rightarrow 2(\text{Si–O–Si})_n\text{–OH} + 2M^{(m-1)+} \qquad (4\text{-}1)$$

$$2(\text{Si–O–Si})_n\text{–O}^- + Sn^{4+} + H_2 \rightarrow 2(\text{Si–O–Si})_n\text{–OH} + Sn^{2+} \qquad (4\text{-}2)$$

Analogous reactions have been reported for Cu^{2+} in zeolite derivatives [5], and other metal cations (M^{m+} = Eu^{3+} [6-9], Mn^{3+} [8], Ce^{4+} [10]) in Al_2O_3–SiO_2 glasses,

$$2(\text{Si–O–Al})_n\text{–O}^- + 2\text{M}^{m+} + \text{H}_2 \rightarrow 2(\text{Si–O–Al})_n\text{–OH} + 2\text{M}^{(m-1)+} \qquad (4\text{-}3)$$

In this study, Co cation-doped SiO_2/γ-Al_2O_3 composite materials were synthesized, then, the reversible redox properties of Co cations around the hetero interface in the composites were intensively studied. First, a Co cation-doped SiO_2 thin film was deposited on a mesoporous γ-Al_2O_3 layer and an equilibrium chemical composition of the Al, Si and Co within the mesoporous γ-Al_2O_3 layer was determined. Then, redox properties of Co cations in the Co-doped SiO_2/γ-Al_2O_3 composite as powders with a defined equilibrium chemical composition was investigated by cyclic heat treatment at 300 to 500 °C under alternative flow gas change of H_2 and Ar. Moreover, a unique H_2-triggered chemical valve property of the γ-Al_2O_3/Co-doped SiO_2/γ-Al_2O_3 three-layered composite membrane was discussed based on the unique reversible redox reactions of the Co cation for the purpose of developing novel hydrogen production, storage and transportation systems essential for the establishment of hydrogen-based society.

4.2 Experimental procedures

4.2.1 Sample synthesis

Tetraethoxysilane ($Si(OC_2H_5)_4$, purity > 99.0 %), aluminum nitrate nonahydrate ($Al(NO_3)_3 \cdot 9H_2O$, purity 98.0%), cobalt(II) nitrate hexahydrate ($Co(NO_3)_2 \cdot 6H_2O$, purity 98.0 %), ethanol (C_2H_5OH, purity > 99.5 % and hydrogen peroxide (H_2O_2, 30% aq.) were purchased from Kishida Chemical Co. Ltd., Osaka, Japan.

In this study, for the sample syntheses of Co-doped SiO_2/γ-Al_2O_3 composites and Co-doped aluminosilicate, Co-doped SiO_2 precursor solutions with Co/Si = 1/8, 1/4 and 1/2 were prepared. Here, as an illustration, we describe the preparation of the Co-doped SiO_2 sol with Co/Si = 1/8: a 10 mL round-bottom flask was charged with $Co(NO_3)_2 \cdot 6H_2O$ (0.343 g) and C_2H_5OH (4.2 mL). To this solution, 1.92 mL (8 mmol) of $Si(OC_2H_5)_4$ and H_2O_2 (2.3 mL, 30% aq) was added and maintained at RT with stirring for 1 h, then heated at 60 °C for 2 h.

Prior to the composite sample syntheses, the Co/Si ratio of the precursor-derived Co-doped SiO_2 was examined as follows: the Co-doped SiO_2 sols with different Co/Si ratio were heated with stirring to 80 °C and kept at this temperature overnight to give dried Co-doped SiO_2 gel powder samples. The dried gel powder sample were placed on a quartz boat in a quartz tube furnace (Model ARF-50KC, Asahi Rika Seisakusho Co. Ltd., Chiba, Japan), and heat-treated

in air at 600 °C for 3 h with a heating/cooling rate of 20 °C min^{-1} to afford Co-doped SiO_2 powder samples. Then, elemental analyses were performed for Si and Co (ICP spectrometry, Model ICPS-7510, Shimazu Co., Kyoto, Japan), and carbon (C, non-dispersive infrared method, Model CS844, LECO Co., St Joseph, MI, USA). The residual carbon in the powder samples were negligible (< 0.1 %), and as shown in Table 4-1, we confirmed that the Co/Si ratios in the range of 1/8 to 1/2 were well controlled through the present sol-gel route using H_2O_2.

Table 4-1 Chemical composition of 600 °C heat-treated Si-Co-O powder samples.

Sample Co/Si	Composition/ wt.%*			Co/Si Atomic Ratio	
	Si	Co	O	Cal.	Obs.
1/8	37.9	9.8	52.2	0.125	0.123
1/4	33.0	17.1	49.8	0.250	0.247
1/2	26.1	26.9	46.9	0.500	0.491

* Carbon content < 0.1 %

4.2.1.1 Co-doped SiO_2/γ-Al_2O_3 layered composite sample

Boehmite (γ-AlOOH) coating solution was prepared using the previously reported procedure [11], and spin-coated on a SiO_2 substrate (10 mm x 10 mm x 3 mm, Meijo science Co. Inc., Nagoya, Japan) at 3000 rpm using a spin coater (Model, MS-A100, Mikasa Co. Ltd., Tokyo, Japan). The γ-AlOOH-coated SiO_2 substrate was placed on an Al_2O_3 plate and loaded in an electric furnace (Model FUW220PA, Advantec Toyo Kaisha Ltd., Tokyo, Japan), then heat-treated in air at 600 °C for 3 h with a heating/cooling rate of 100 °C h^{-1} to afford the formation of a γ-Al_2O_3 thin layer over the SiO_2 substrate. Subsequently, Co-doped SiO_2 sol with Co/Si = 1/8 was spin-coated on the γ-Al_2O_3 layer on the SiO_2 substrate by using the same manner as described above. The spin-coated sample substrate was placed on a quartz boat and loaded in a quartz tube furnace (Model ARF-50KC, Asahi Rika Seisakusho Co. Ltd., Chiba, Japan), then heat-treated in air at 600 °C for 20 h with a heating/cooling rate of 20 °C min^{-1}. The sample was labelled **CoSiOAlcoat**.

4.2.1.2 Co-doped SiO_2/γ-Al_2O_3 composite powder sample

γ-Al_2O_3 powder was prepared from γ-AlOOH sol using a previously reported procedure [11]. γ-Al_2O_3 powder was mixed with Co-doped SiO_2 sol with Co/Si = 1/2 at the Al: Si: Co

ratio of 85 : 10 : 5. The resulting mixture was heated with stirring to 80 °C and kept at this temperature overnight to give a dried Co-doped SiO_2 gel/γ-Al_2O_3 powder sample. The dried powders were placed on a quartz boat and set in a quartz tube furnace (Model ARF-50KC, Asahi Rika Seisakusho Co. Ltd., Chiba, Japan), then heat-treated in air at 600 °C for 20 h with a heating/cooling rate of 20 °C min^{-1}. The sample was labelled **CoSiOAlpow**.

4.2.1.3 Hmogeneous Co-doped aluminosilicate powder sample

To study the redox behavior of the Co cation in amorphous aluminosilicate matrix, Co-doped aluminosilicate sol was prepared according to an atomic ratio of Al (in $Al(NO_3)_3 \cdot 9H_2O$):Si (in $Si(OC_2H_5)_4$):Co (in $CoNO_3 \cdot 6H_2O$) = 8:8:1. A 50 mL round-bottom flask equipped with a magnetic stirrer was charged with $Co(NO_3)_2 \cdot 6H_2O$ (0.343 g), $Al(NO_3)_3 \cdot 9H_2O$ (3.262 g) and C_2H_5OH (20 mL). To this solution, 1.92 mL (8 mmol) of $Si(OC_2H_5)_4$ and H_2O_2 (2.3 mL, 30% aq) was added and maintained at RT with stirring for 1 h, then heated at 60 °C for 2 h to give a Co-doped aluminosilicate sol. Then, the resulting sol was dried at 80 °C overnight to give the dried gel powder sample. The sample were placed on a quartz boat in a quartz tube furnace (Model ARF-50KC, Asahi Rika Seisakusho Co. Ltd., Chiba, Japan), and heat-treated in air at 600 °C for 3 h with a heating/cooling rate of 20 °C min^{-1}. This sample was labelled **CoSiOAlpow2**.

As reference data, the textural properties were characterized for the composite powder samples. The surface morphology of **CoSiOAlpow** and **CoSiOAlpow2** samples is shown in Fig. 4-1. The **CoSiOAlpow** sample kept the morphology of γ-Al_2O_3 polycrystallites (Fig. 4-1a), while the **CoSiOAlpow2** sample exhibited a featureless glassy surface (Fig. 4-1b). The N_2 adsorption and desorption isotherms of the **CoSiOAlpow** sample exhibited Type-IV isotherms according to the IUPAC classifications [12] and formed a hysteresis loop indicating

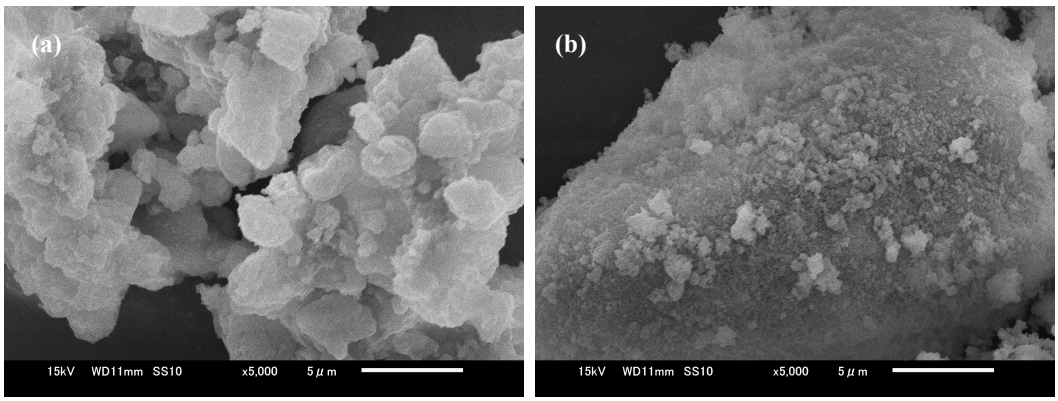

Fig. 4-1 SEM images of (a) **CoSiOAlpow** and (b) **CoSiOAlpow2** samples.

the presence of mesoporosity, while those of **CoSiOAlpow2** sample presented Type-II isotherms [12] without a distinct hysteresis loop (Fig. 4-2a). The PSD curve characterized by the BJH method [13] for each powder sample was consistent with the N_2 adsorption-desorption behavior: the **CoSiOAlpow** sample exhibited a PSD curve with a dominant peak at 8 nm, while **CoSiOAlpow2** sample showed a broad and weak peak ranging from 20 to 100 nm (Fig. 4-2b). The resulting Brunauer-Emmett-Teller (BET) surface areas of the **CoSiOAlpow** and **CoSiOAlpow2** samples were measured to be 249 and 94 $m^2\ g^{-1}$, respectively.

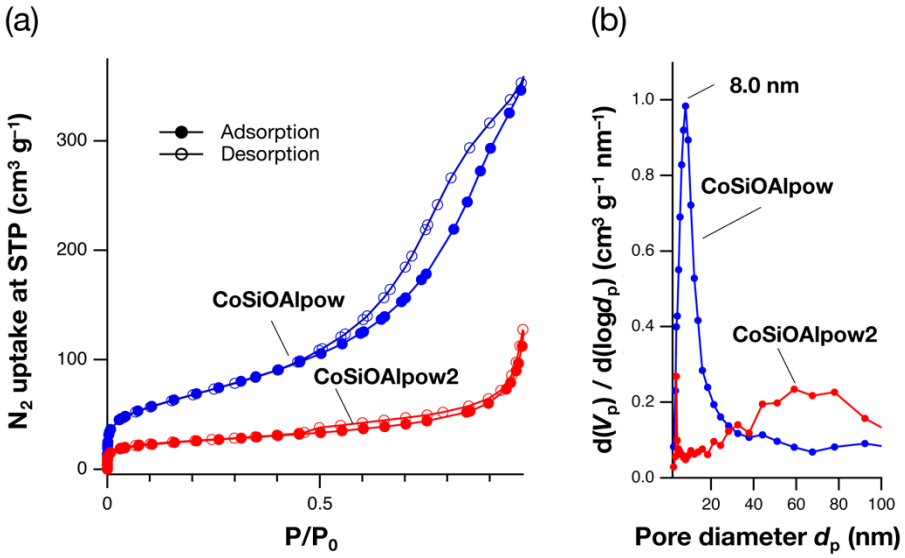

Fig. 4-2 (a) N_2 adsorption-desorption isotherms at –196 °C for the **CoSiOAlpow** and **CoSiOAlpow2** samples, and (b) the pore size distribution curves characterized by the BJH plot.

4.2.1.4 γ-Al_2O_3/Co-doped SiO_2/γ-Al_2O_3 layered composite membrane sample

A mesoporous γ-Al_2O_3 layer was formed on an outer surface of a macroporous α-Al_2O_3 support (tubular-type, 6 mm outer diameter, 2 mm thickness and 60 mm length, porosity 40 %, Noritake Co., Ltd., Aichi, Japan) according to a published procedure [11]. The mesoporous γ-Al_2O_3-modified tubular support was dipped into Co-doped SiO_2 sol with Co/Si = 1/4 at 10 mm s^{-1}, kept in the sol for 30 s, then pulled out at 1 mm s^{-1} before heat treatment at 600 °C for 20 h under the same manner as that for the **CoSiOAlpow** sample synthesis. This dip-coating-heat treatment sequence was repeated once to form a Co-doped SiO_2 thin film on the supported mesoporous γ-Al_2O_3 layer. Then, the Co-doped SiO_2 thin film was coated with γ-AlOOH sol (diluted as 0.5 mol L^{-1}) and heat-treated in air at 600 °C for 3 h by using the same manner as described above to give γ-Al_2O_3/Co-doped SiO_2/γ-Al_2O_3 three-layered composite membrane.

The sample was labelled **CoSiOAlmemb**.

4.2.2 Characterizations

X-ray diffraction (XRD) measurements were performed on powder samples (Model X'pert Pro 1, Philips Ltd., Amsterdam, Nederland).

X-ray photoelectron spectroscopic (XPS) analysis was performed on **CoSiOAlpow2** sample with an Al K*a* X-ray source operated at 14 kV and 14 mA (Model PHI-5000, Ulvac-phi, Kanagawa, Japan). An alignment on the C 1s peak (at 284.8 eV) was performed before survey scans. To investigate the reversible redox property of Co cation in the aluminosilicate, the **CoSiOAlpow2** sample was heat-treated at 350 °C for 1 h with a heating/cooling rate of 5 °C min^{-1} under H_2 flow. Then, under Ar flow, the sample was heat-treated at 350 °C for 10 h with a heating/cooling rate of 5 °C min^{-1}. The heat treatments were cyclically performed under flowing of H_2-Ar-H_2, or H_2-Ar-H_2-Ar using a catalyst analyzer (BELCAT-A, MicrotracBEL Corp., Osaka, Japan). Then, Co 2p spectrum was recorded for the heat-treated sample.

To investigate the distribution of Co cations within the **CoSiOAlcoat** sample, the depth-profiling XPS analysis was carried out by combining Ar ion gun etching cycles at 3 kV. The etching rate was calibrated as 3.73 nm min^{-1} by measuring that of the SiO_2 substrate.

Surface morphology of **CoSiOAlpow** and **CoSiOAlpow2** samples, and the cross-section of the **CoSiOAlmemb** sample were observed by a scanning electron microscope (SEM, model JSM-6010LA, JEOL Ltd., Tokyo Japan) operated at a voltage of 15 kV.

The BET surface area of the **CoSiOAlpow** and **CoSiOAlpow2** samples was evaluated by measuring N_2 adsorption and desorption isotherms at –196 °C under relative pressure ranging from 0 to 0.99 (Model Belsorp Max, BEL Japan Inc., Osaka, Japan).

Nanostructure of the **CoSiOAlpow** sample was characterized by transmission electron microscopy (TEM) using a high-angle annular dark-field-scanning transmission electron microscope (HAADF-STEM, Model JEM-ARM200F, JEOL Ltd., Tokyo, Japan, operated at an accelerating voltage of 200 kV). The distribution of the constituent elements of Si, Al, Co and O was measured and analyzed by the energy dispersive X-ray spectrometer (EDS, Model JED-2300, JEOL Ltd., Tokyo, Japan) mounted on JEM-ARM200F.

Local structure of γ-Al_2O_3 powder sample was studied by ^{27}Al solid-state magic angle spinning nuclear magnetic resonance (MAS NMR) spectroscopic analysis with 600 MHz NMR spectrometer (Model JNM-ECA600II, JEOL Ltd., Tokyo, Japan) operating at a static magnetic field of 14.01 T (155.4 MHz). Single gas permeances of the **CoSiOAlmemb** sample were

evaluated for He and H_2 by the constant-volume manometric method [14]. The evaluations were performed at 100 to 500 °C according to the procedure as reported elsewhere [15, 16]. The pressure on the gas feed side in this study was maintained at 120 kPa. On the gas permeate side, the gas line and the buffer tank with the total volume of 3.11 $x10^{-4}$ m^3 were completely evacuated by using an oil rotary vacuum pump. After the evacuation was terminated, the pressure increase rate at the inside of the buffer tank was measured totally three times. The average of the three measurements was used for calculation of permeance of gas-*i* (Q_i).

The hydrogenation/dehydrogenation reactions were in-situ monitored for the **CoSiOAlpow** sample by diffuse reflectance infrared Fourier transform spectroscopy (DRIFTS, Model Spectrum 100, Perkin Elmer, Waltham, MA, USA). The Co-doped SiO_2/γ-Al_2O_3 composite powder sample was loaded in a diffuse reflection cell (Model STJ900C Diffuse IR Heat Cham, S.T. JAPAN Inc., Tokyo, Japan), and IR spectrum was recorded after each treatment: i) Heat-treatment to remove adsorbed water at 500 °C for 8 h under a flow of Ar (4 mL min^{-1}), ii) subsequent heat treatment at 500 °C for 0.5 h under a flow of H_2 (4 mL min^{-1}) , and iii) final heat treatment at 500 °C for 8 h under a flow of Ar (4 mL min^{-1}).

Temperature-programmed reduction (TPR) and desorption (TPD) experiments were performed on the **CoSiOAlpow** sample using a catalyst analyzer (BELCAT-A, MicrotracBEL Corp., Osaka, Japan) fixed with a quadrupole mass spectrometer (BEL Mass, MicrotracBEL Corp., Osaka, Japan). The TPR profile was measured during heating from 100 to 500 °C (5 °C min^{-1}) under a flow of 10 % H_2/Ar (50 mL min^{-1}). Then, the sample powder was maintained under pure-H_2 flow (50 mL min^{-1}) for 1 h and cool down to room temperature. The subsequent TPD measurement was carried out by heating up to 500 °C (5 °C min^{-1}) under He flow (50 mL min^{-1}). This cyclic TPR/TPD measurement was repeated 3 times.

In-situ X-ray Adsorption Fine Structure (XAFS) spectroscopic analyses were conducted at the BL5S1 of Aichi Synchrotron Radiation Center (AichiSR, Aichi Science & Technology Foundation, Aichi, Japan). The experimental set up is shown in Fig. 4-3. The absorption spectrum can be obtained based on Eq. 4-4, where μ and t are absorption coefficient and sample thickness, respectively.

$$\mu t = -\ln(I_1/I_0) \qquad (4\text{-}4)$$

The **CoSiOAlpow** sample (3.1 mg) was diluted with hexagonal boron nitride powder (100 mg, provided by the AichiSR) using an agate mortar and pestle, then uniaxially pressed into a

disk with a diameter of 7 mm. The disk sample was loaded in a quartz cell equipped with an electric heater and gas lines (Model 2000-1431, Makuharikagaku Garasu Seisakusho Inc., Chiba, Japan) and maintained for 30 min under Ar flow. Then, under H_2 flow, the disk sample was heat-treated at 500 °C for 30 min with a heating rate of 8 °C min^{-1}. Subsequently, under Ar flow, the furnace was cooled down to RT with a cooling rate of 8 °C min^{-1} followed by maintaining at RT for additional 1 h. During this treatment, the spectrum was recorded stepwise at each measurement as follows: (1) at RT under initial Ar flow, (2) after H_2 treatment at 500 °C for 30 min, (3) at RT after cooling down from 500 °C under Ar flow, and (4) at RT after maintaining under Ar flow for 1 h. In this study, the measurements were also performed on Co_3O_4 (4N, Kojundo Chemical Laboratory Co., Ltd., Saitama, Japan), CoO and Co-foil (stored at AichiSR) at RT as reference samples. Then to investigate the reversible redox property of the **CoSiOAlpow** sample, X-ray Absorption Near Edge Structure (XANES) spectroscopic analyses were performed using a software (ATHENA/ Demeter [17]).

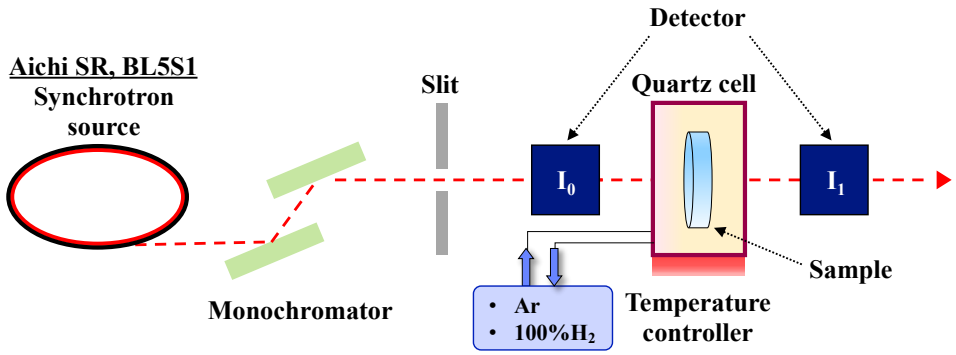

Fig. 4-3 Experimental set up for in situ XAFS spectroscopic analysis.

4.3 Results and Discussion

4.3.1 Distribution of Co cations within the Co-doped SiO_2/ γ-Al_2O_3 layered composite sample

To investigate the chemical composition at the hetero interface between the Co-doped SiO_2 and γ-Al_2O_3, a Co-doped SiO_2 thin layer was formed on a mesoporous γ-Al_2O_3 layer supported on a SiO_2 substrate. This sample labelled **CoSiOAlcoat** has been deposited by spin-coating of the Co-doped SiO_2 sol with Co/Si = 1/8 followed by heat treatment in air at 600 °C for 20 h as detailed in the experimental section. Figure 4-4 presents the results of depth-profiling XPS analysis for the constituent elements of Si, Co, and Al. The thickness of Co-doped SiO_2 top-

layer was approximately 37 nm estimated based on the Ar sputtering rate determined for SiO_2 substrate. Then, almost entire mesopore channels of the γ-Al_2O_3 layer with a thickness of about 85 nm were infiltrated by the Co-doped SiO_2. During spin-coating process, Co-doped SiO_2 sol solution easily penetrated into the mesoporous γ-Al_2O_3 layer. However, the depth profile of Co revealed that the Co/Si ratio of the top layer is approximately 1/37, much lower than the nominal composition of Co-doped SiO_2 coating sol (1/8). On the other hand, around the Co-doped SiO_2/γ-Al_2O_3 hetero interface (around 50 nm in depth), the Co content increased to approximately 3 at%, then within the mesoporous γ-Al_2O_3 layer at 60 to 100 nm in depth, the Co content is shown to be constant at a value of ca. 2 at% and the resulting Al:Si:Co ratio is 85:10:5.

The high Co concentration at the interface of γ-Al_2O_3 layer is consistent with the previous

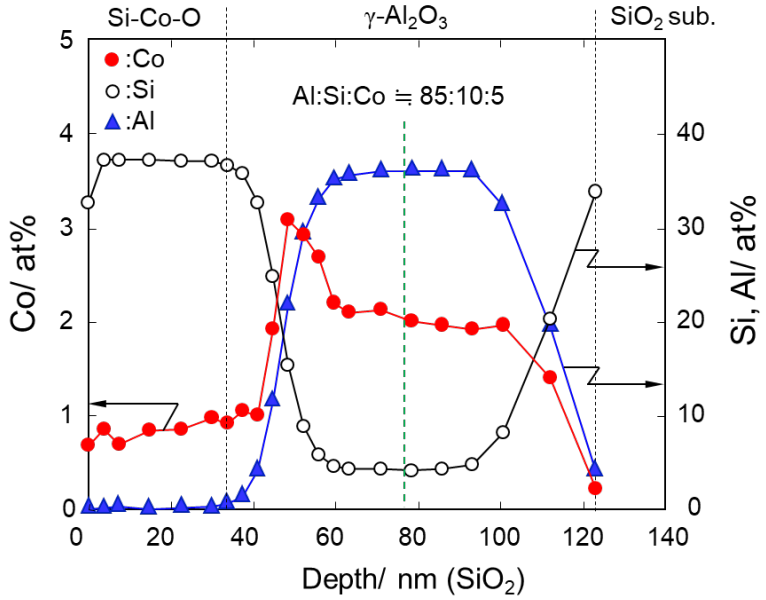

Fig. 4-4 Depth-profiling XPS analysis for Co, Si, and Al within the **CoSiOAlcoat** sample.

report on the synthesis of Co-doped SiO_2 membrane on a porous Al_2O_3 support by Diniz Da Costa *et al*. [18]. The observed high concentration of Co around the hetero interface revealed preferential diffusion of Co cation from SiO_2 matrix to γ-Al_2O_3 surface. As shown in Fig. 4-5, ^{27}Al solid-state MAS-NMR spectroscopic analysis reveals that γ-Al_2O_3 prepared in this study is composed of AlO_4 (at 66 ppm) and AlO_6 (at 1 ppm) units with the AlO_6/AlO_4 unit ratio of about 2.4, which is consistent with reported data [19]. Moreover, our previous study on the mesoporous γ-Al_2O_3 revealed that considerable amount of Al-OH group existed at the γ-Al_2O_3 surface which led to the highly hydrophilic property of γ-Al_2O_3 [11]. Accordingly, the driving force for the Co diffusion is due to the charge compensation for the AlO_4 site within the

amorphous aluminosilicate formed in-situ at the hetero interface (Fig. 4-6), m[(SiO_4)(AlO_4^-)]Co^{m+} (m = 2 or 3). Based on these results, the Al:Si:Co ratio of 85:10:5 was selected as an equilibrium chemical composition to investigate the redox property of Co cation at the SiO_2/γ-Al_2O_3 hetero interface.

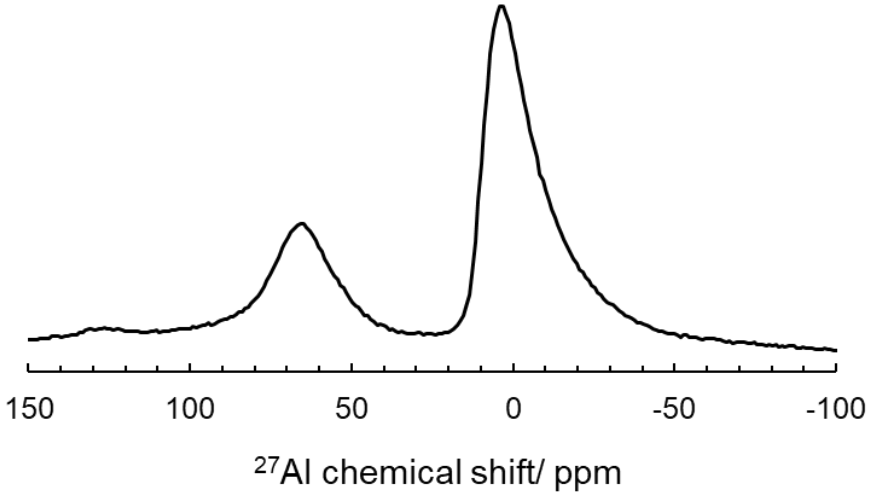

Fig. 4-5 ^{27}Al solid-state MAS-NMR spectrum of the γ-Al_2O_3 powder sample showing two peaks at 66 and 1 ppm assigned to AlO_4 and AlO_6 units, respectively.

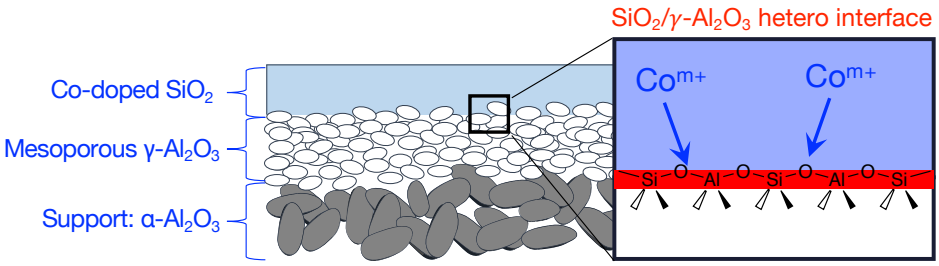

Fig. 4-6 Schematic illustration of diffusion of Co^{m+} cations to Co-doped SiO_2/γ-Al_2O_3 hetero interface for charge compensation at the AlO_4 sites.

4.3.2 Properties of Co-doped SiO_2/γ-Al_2O_3 composites

To investigate the later redox properties of Co cations at the SiO_2/γ-Al_2O_3 hetero interface, we prepared powders labelled **CoSiOAlpow** with the equilibrium chemical composition (Al:Si:Co = 85:10:5). We first investigated the structural and microstructural changes of the material after H_2 treatment (the reductive condition) at 500 °C. As shown in Fig. 4-7, the X-ray diffraction pattern of the **CoSiOAlpow** sample is composed of XRD peak of γ-Al_2O_3 indicating that the Co-doped SiO_2 layer is X-ray amorphous. Then, after the H_2 treatment at 500 °C, it retains the X-ray amorphous state of the Co-doped SiO_2 phase.

TEM observation of the 500 °C-H_2 treated **CoSiOAlpow** sample (Fig. 4-8) also results in the detection of γ-Al_2O_3 as a single crystalline phase by the selected area electron diffraction ring pattern analysis (inset in Fig. 4-8a), and the composite powder sample was composed of polycrystalline γ-Al_2O_3 of several nanometers in size (Fig. 4-8b). Then, STEM-EDS mapping for the constituent elements of Al, Si, Co and O within the area of the annular dark-field (ADF)-STEM image (Fig. 4-9a) revealed homogeneous distribution of Co and Si as well as Al and O (Figs. 4-9b–e). Accordingly, the composite sample powders are characterized as γ-Al_2O_3 polycrystalline homogeneously modified with Co-doped amorphous SiO_2.

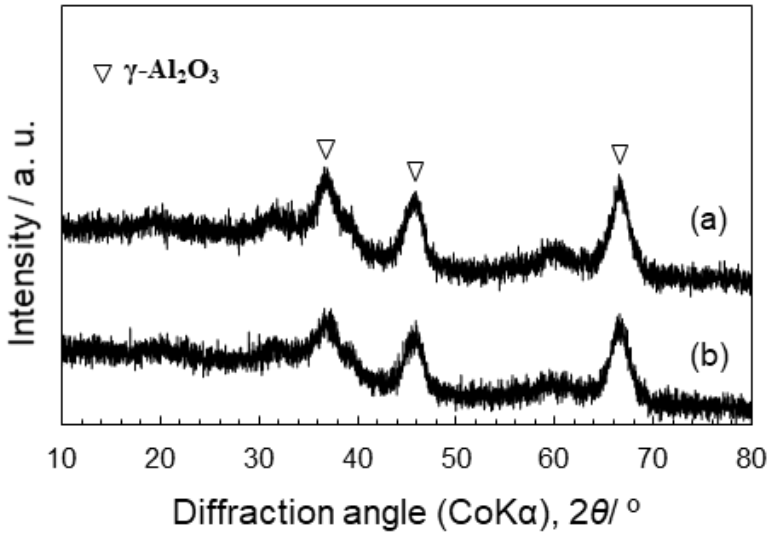

Fig. 4-7 XRD patterns of the **CoSiOAlpow** sample. (a) As synthesized and (b) after H_2 treatment at 500 °C for 1 h

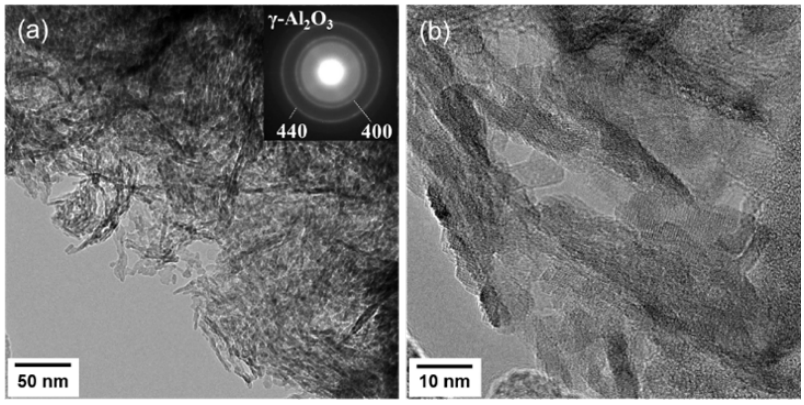

Fig. 4-8 (a) TEM image of the **CoSiOAlpow** sample and the corresponding selected area electron diffraction pattern obtained, and (b) HRTEM image showing γ-Al_2O_3 polycrystalline of several nanometers in size.

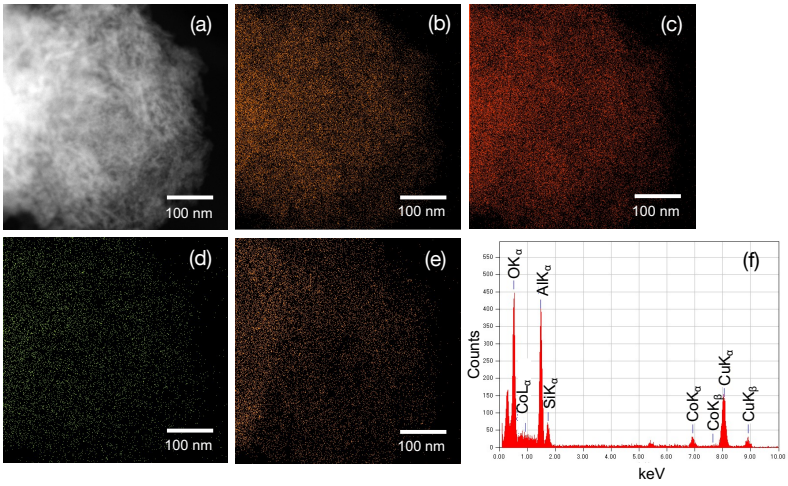

Fig. 4-9 STEM-EDS mapping analysis for the **CoSiOAlpow** sample. (a) Annular dark field (ADF)-STEM image and the results of EDS mapping of (b) Al, (c) O, (d) Co, and (e) Si. (f) Typical EDS spectra recorded for the mapping analyses.

4.3.3 Redox behavior of Co species

Redox properties of the Co cation in the **CoSiOAlpow** sample were assessed by in-situ using XAFS spectroscopic analyses. The **CoSiOAlpow** sample was heat-treated at 500 °C under H_2 flow followed by cooling to RT under Ar flow (Fig 4-10a). The spectra recorded at the measurement points shown in Fig. 4-10a are shown in Fig. 4-10b.

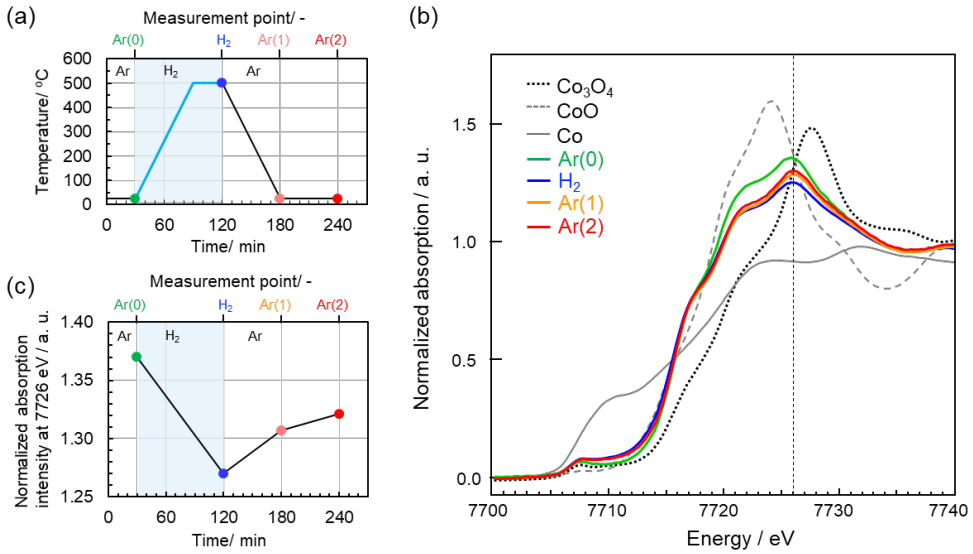

Fig. 4-10 Results of in-situ XAFS spectroscopic analysis for the **CoSiOAlpow** sample. (a) Heat treatment conditions and spectrum measurement points in this study, (b) XANES spectra of the **CoSiOAlpow** and reference samples, and (c) change in normalized absorption peak intensity at 7726 eV shown in (b).

The **CoSiOAlpow** sample at RT under the initial Ar flow (Ar(0) in Fig. 4-10a) exhibits a spectrum with a peak at 7726 eV, and this spectrum was different from those of references, Co_3O_4, CoO and Co-foil recorded at RT. The unique behavior is that the peak intensity at 7726 eV changes reversibly (Fig. 4-10c): after the 500 °C H_2-treatment (H_2 in Fig. 4-10a), the peak intensity decreases, *i.e.*, approaches the intensity level of the Co-foil at 7726 eV, then increases in a stepwise manner under Ar flow after cooling down to RT (Ar(1) in Fig. 4-10a) followed by being maintained at RT for 1 h (Ar(2) in Fig. 4-10a).

As discussed above, the metallic Co was not detected by our intensive HRTEM-STEM analyses. Thus, the spectra shown in Fig. 4-8b suggested that the Co species in the **CoSiOAlpow** sample were Co(III) and Co(II) with the Co(III)/Co(II) ratio lower than that in Co_3O_4 (Co(III)/Co(II) = 2/1). Moreover, the peak intensity change shown in Fig. 4-10c suggests the reversible redox property of Co cation species in the **CoSiOAlpow** sample under the present cyclic condition of Ar (RT)-H_2 (500 °C)-Ar (RT) treatment.

To investigate the nature of the Co-doped SiO_2/γ-Al_2O_3 hetero interface during the redox reactions of Co species, in-situ DRIFT spectroscopic analysis was performed on the **CoSiOAlpow** sample under a cyclic heat-treatment condition under Ar flow, followed by 10%H_2/Ar flow and subsequent Ar flow at 500 °C. The results are shown in Fig. 4-11. Due to the heterogeneous structure with the Co-doped SiO_2/γ-Al_2O_3 hetero interface, the **CoSiOAlpow** sample exhibits broad spectra of OH groups in the range of 3800–3200 cm^{-1}: the initial DRIFT spectrum under Ar flow at 500 °C exhibited a broad peak around 3736 cm^{-1} attributed to free Si-OH group [20, 21] together with a broader one from 3640 to 3300 cm^{-1}

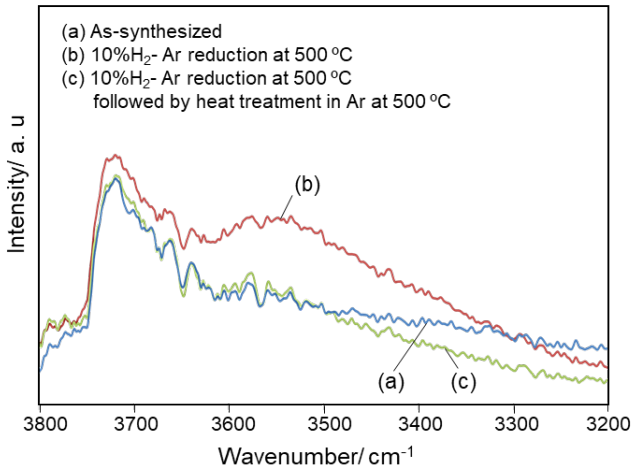

Fig. 4-11 In-situ DRIFT spectroscopic analysis for the Co-doped silica/γ-Al_2O_3 composite powder sample (**CoSiOAlpow** sample) with nominal composition of Al:Si:Co = 85:10:5. (a) As-synthesized, (b) after heat-treatment at 500 °C under 10% H_2–Ar flow for 8 h, and (c) after subsequent heat-treatment at 500 °C under Ar flow for 8 h.

assigned to hydrogen-bonded X-OH (X = Si or Al) group [6, 22] (Fig. 4-11a). After heat treatment under 10%H_2-Ar flow for 5 h at 500 °C, the intensity of the broader peak at 3640 to 3300 cm^{-1} increased (Fig. 4-11b), then decreased to be close to the initial intensity level after the subsequent Ar treatment at 500 °C (Fig. 4-11c). Accordingly, it is suggested that the reduction-oxidation of Co cation species in the **CoSiOAlpow** sample is associated with OH formation-deformation, *i.e.*, hydrogenation-dehydrogenation.

To identity the hydrogenation-dehydrogenation reactions, cyclic TPR/TPD analysis was performed on the **CoSiOAlpow** sample. In this attempt, the first TPR/TPD was conducted to initialize the oxidation state of the composite powder sample, then the TPR/TPD profiles were recorded for the 2nd and 3rd cycles. As shown in Fig. 4-12, both the 2nd and 3rd TPR profiles showed a weak broad peak for H_2 up-take at 250 to 300 °C, and a larger one at 400 to 500 °C, then the H_2-uptake continued to some extent under the isothermal H_2-treatment at 500 °C. Both the 2nd and 3rd TPD profiles show appropriate desorption peaks, a very weak peak at 250 to 350 °C and another larger one during the isothermal Ar-treatment at 500 °C. The simultaneous

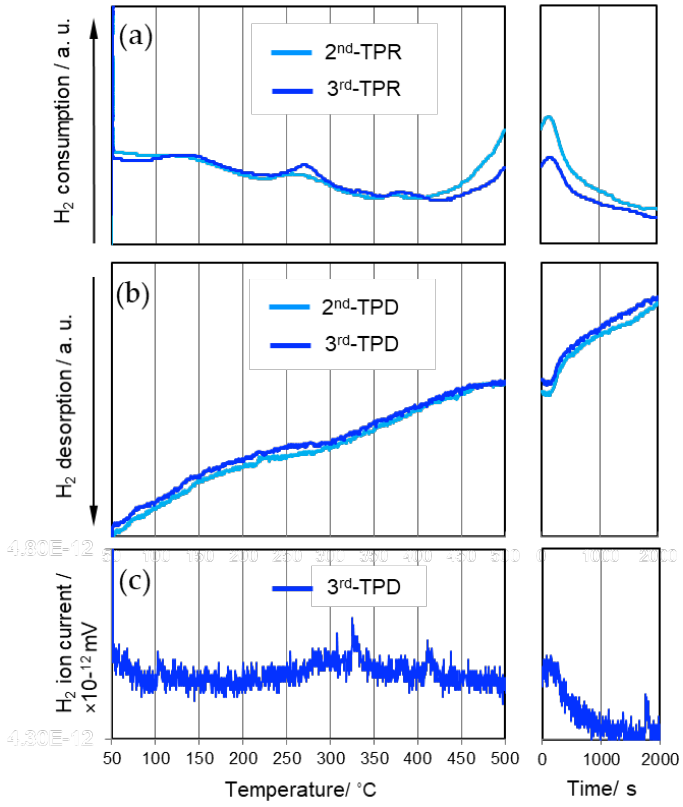

Fig. 4-12 Results of cyclic TPR/TPD analysis for the Co-doped silica/γ-Al_2O_3 composite powder sample (**CoSiOAlpow** sample) with nominal composition of Al:Si:Co = 85:10:5. (a) 2nd and 3rd TPR profiles, (b) 2nd and 3rd TPD profiles, and (c) H_2 ion current detected during the 3rd TPD profile measurement.

MS analysis resulted in the detection of a trace amount of H_2 as a single desorption component at the two temperature regions appropriate to the desorption peaks.

These results suggest the followings:

- The reduction-oxidation of Co cation species in the **CoSiOAlpow** sample proceeds associated with formation-deformation of OH groups.
- The redox reactions begin to proceed from relatively low temperatures around 250 to 350 °C.
- The redox reactions are reversible and governed by the H_2 partial pressure at $T \geq 250$ °C.

For further investigation on the redox reactions of the Co cation species that proceeded around 250 to 350 °C, we prepared another powder sample labelled **CoSiOAlpow2** with homogeneous structure having almost same Co content, but a higher Co/Al of 1/8 compared with that of **CoSiOAlpow** (1/17).

The redox behaviors of the Co cation species were investigated by the cyclic heat treatment up to 350 °C. The **CoSiOAlpow2** sample kept X-ray amorphous state after the cyclic heat treatment at 350 °C under flow of H_2-Ar-H_2 or H_2-Ar-H_2-Ar (Fig. 4-13A). As shown in Fig. 4-13B, the XPS spectrum of as-synthesized **CoSiOAlpow2** sample (green line) exhibited a broad peak centered at 782 eV attributed to Co^{2+} together with another broad peak around 788 eV correspond to a Co^{2+} satellite peak (labeled * in the graph) [23]. In addition, on the right side of the Co^{2+} peak, there was a peak shoulder at 779.9 eV assigned to Co^{3+} [23]. The Co^{3+} peak intensity at 779.9 eV apparently decreased after the second H_2 treatment of the H_2-Ar-H_2 run

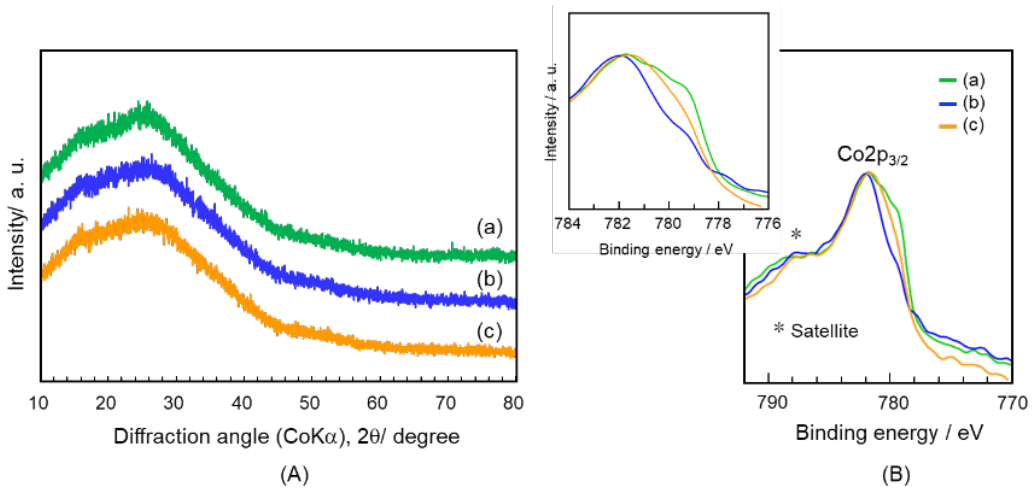

Fig. 4-13 (A) XRD patterns and (B) XPS spectra of the **CoSiOAlpow2** sample. (A) As-synthesized, after (B) heat treatment at 350 °C for 1 h under H_2 flow and the subsequent heat treatment at 350 °C for 10 h under Ar flow.

(blue line), while that due to metallic-Co (777.8 eV) [23] was not observed. Then, after the subsequent Ar treatment (H_2-Ar-H_2-Ar run), the Co^{3+} peak intensity increased to some extent (orange line).

The oxidation state of Co cation in the starting $Co(NO_3)_2 \cdot 6H_2O$ was divalent (II). Moreover, metallic Co was not formed under the present heat treatment conditions, and thus formation of Co(III) via the disproportionation reaction ($3Co^{2+} \rightarrow 2Co^{3+} + Co$) was excluded. It should be also noted that the oxidation state of the Co cation in the polymer-derived Co-doped amorphous SiO_2 was completely divalent [24].

It is well known that the Fenton reaction is the Fe(III/II)-catalyzed oxidation of organic compounds (RH) via generation of highly reactive radical specie (•OH) in the presence of H_2O_2 [25, 26]:

$$Fe^{2+}(aq) + H_2O_2 \rightarrow Fe^{3+}(aq) + OH^- + \bullet OH \qquad (4\text{-}5)$$

$$RH + \bullet OH \rightarrow \bullet R + H_2O \qquad (4\text{-}6)$$

Recently, Ling reported [27] that Co(II) analogously generates •OH in the presence of H_2O_2,

$$Co^{2+}(aq) + H_2O_2 \rightarrow Co^{3+}(aq) + OH^- + \bullet OH \qquad (4\text{-}7)$$

In this study, H_2O_2 was used to prepare the precursor solutions for the Co-doped SiO_2 system, which resulted in the partial formation of Co(III) cations within the sample powders via the Fenton reaction. The results obtained in the present study reveal that reversible Co(III)/Co(II) redox reactions are associated with OH formation-deformation, which is governed by the H_2 partial pressure at 250 to 500 °C:

$$2(Si{-}O{-}Al)_n{-}O^- + 2Co^{3+} \underset{-H_2 \text{ in Ar}}{\overset{+ H_2}{\rightleftharpoons}} 2(Si{-}O{-}Al)_n{-}OH + 2Co^{2+} \qquad (4\text{-}8)$$

The H_2 up-take/desorption of the **CoSiOAlpow** sample was mainly detected at higher temperatures around 500 °C (Fig. 4-12). This could be explained by the kinetic factor necessary for H_2 diffusion through the amorphous SiO_2 network between the top surface and the SiO_2/γ-Al_2O_3 hetero interface where Co cations mainly existed.

4.3.4 Gas permeation properties of γ-Al_2O_3/Co-doped SiO_2/γ-Al_2O_3 layered composite membrane

The cross-sectional SEM image of the layered composite membrane sample labelled **CoSiOAlmemb** is shown in Fig. 4-14. In this study, the initial Co content of the SiO_2 layer was reduced from Co/Si = 1/2 to 1/4, then the Co-doped SiO_2 layer (Co/Si = 1/4) was placed between the two mesoporous γ-Al_2O_3 layers to investigate the relationship between the Co(III)/(II) redox reactions at the SiO_2/γ-Al_2O_3 hetero interface and gas permeation properties. Initially, He permeance was measured at 100 to 500 °C. As shown in Fig. 4-15a, initial He permeance (Q_{He}-1st) at 100 °C was 3.1 x 10^{-6} mol m^{-2} s^{-1} Pa^{-1}, then it slightly increased with the permeation temperature. On other hand, after H_2-treatment at 500 °C, the H_2 permeance (Q_{H2}) at 500 °C was slightly higher than that of Q_{He}-1st, and the Q_{H2} showed an opposite temperature dependency, with decreasing temperature, the Q_{H2} increases. Finally, after the subsequent He-treatment at 500 °C for 8 h, the He permeance (Q_{He}-2nd) at 500 °C was close to Q_{He}-1st, then showed a positive temperature dependency similar to that observed for Q_{He}-1st.

The temperature dependency of the Q_{He}-1st and Q_{He} -2nd reveals that He dominantly permeates through micropore channels with a pore size close to the kinetic diameter of He (0.26 nm) [28], and both Q_{He}-1st and Q_{He} -2nd are governed by activated diffusion theoretically expressed as,

$$Q_i = Q_0 \exp\left(-\frac{Ea}{RT}\right) \tag{4-9}$$

where Q_i is the permeance of permeate gas-i, Q_0 is the pre-exponential factor (mol m^{-2} s^{-1} Pa^{-}

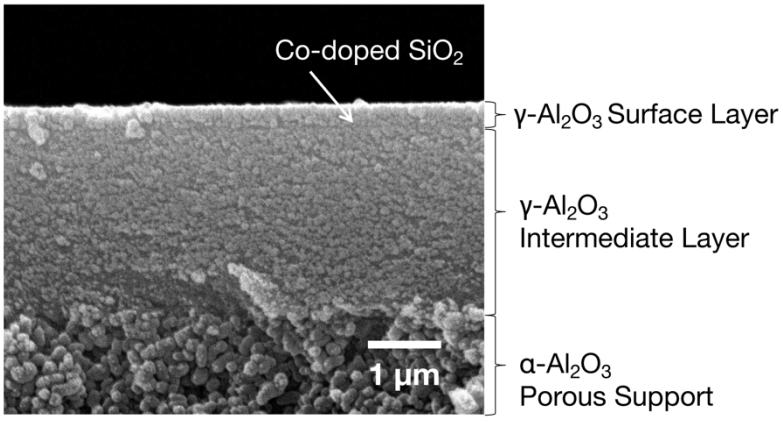

Fig. 4-14 Cross-sectional SEM image of the **CoSiOAlmemb** sample.

^{1}), *Ea* is the activation energy (J mol^{-1}), *R* is the gas constant (8.314 J mol^{-1} K^{-1}), and *T* is the temperature (K) [29, 30].

On the other hand, as shown in Fig. 4-15a, the Q_{H2} is proportional to the inverse square root of permeation temperature ($T^{-0.5}$) and is thus suggested to be governed by the Knudsen's diffusion mechanism. The theoretical gas permeance based on the Knudsen diffusion through a membrane having pore radius (d_p), porosity (ε), tortuosity (τ) and thickness (L) is formulated using the molecular weight of the permeating gas-i (M_i) and the permeation temperature (T) as follows,

$$Q_i = \frac{\varepsilon_i d_{p,i} \rho_i}{\tau_i L_i} \sqrt{\frac{8}{\pi M_i R T}} \qquad (4\text{-}10)$$

where ρ is the probability of diffusion through the pore channel, ρ_i, ε_i, $dp_{,i}$, τ_i, and L_i are membrane structural factors due to possible dependence on the size of permeate gas-i [31].

Knudsen diffusion occurs when the mean free path of the permeate gas molecule is relatively longer than the pore diameter, so the permeate gas molecules collide frequently with the pore wall. Generally, Knudsen diffusion is dominant for mesopores (2-50 nm) [11, 31]. Since the kinetic diameter of He (0.26 nm) is smaller than that of H_2 (0.289 nm) [28], prior to the activated diffusion through micropores, He molecules should exhibit Knudsen diffusion characteristics by permeating through the mesopore channels where H_2 molecules dominantly permeate. These results suggest that the size of the gas permeable channel pores alternatively changes from micropores under He flow to mesopores under H_2 flow, then back to micropores under He flow.

Time dependence of the Q_{He} was monitored after maintaining the **CoSiOAlmemb** sample under H_2 flow for 4h. In this attempt, H_2-treatment and subsequent Q_{He} measurements were performed at the lower temperature of 300 °C to highlight the time dependence. As shown in Fig. 4-15b, the initial Q_{He} of 3.53 x 10^{-6} mol m^{-2} s^{-1} Pa^{-1} slightly decreased with time and reached 3.45 x 10^{-6} mol m^{-2} s^{-1} Pa^{-1} after 24 h. Then, after the second H_2-treatment for 4 h, the Q_{He} regained close to its initial level. Accordingly, the size of pore channels under the H_2 flow became larger, and then reduced to be close to the initial size. This reversible change in pore size could be explained by the reversible redox of Co(III)/(II) associated with the OH group formation/deformation (Eq. 4-8) , *i.e.* bond cleavage-regeneration of the Si-O-Al amorphous network governed by the H_2 partial pressure at 300 to 500 °C (Fig4-16).

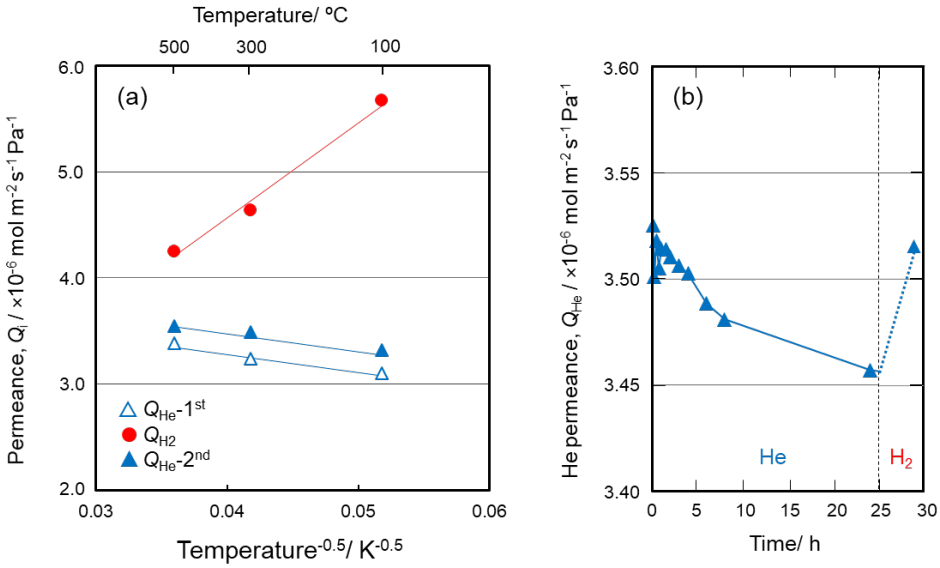

Fig. 4-15 (a) Single gas permeation behaviours through the **CoSiOAlmemb** sample, and (b) time dependence of Q_{He} after H_2 treatment at 300 °C for 4 h.

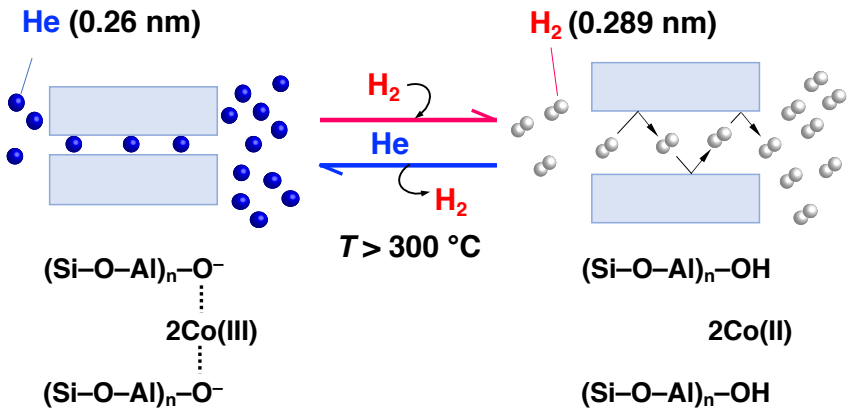

Fig.4-16 Schematic illustration of a suggested mechanism for effective enhancement of high-temperature hydrogen permeance of Co-doped amorphous SiO_2/γ-Al_2O_3 composite membrane: reversible change in pore size by the reversible redox of Co(III)/(II) associated with the OH group formation/deformation

4.4 Conclusions

In this study, Co-doped SiO_2/ γ-Al_2O_3 composite samples were synthesized by conventional sol-gel method using H_2O_2. The redox behaviors of the Co-cations in the composite samples were studied and the results can be summarized as follows:

(1) XPS depth profile analyses for the Co-doped SiO_2/mesoporous γ-Al_2O_3 layered composite sample revealed preferential Co diffusion from the SiO_2 top-layer matrix to the γ-Al_2O_3

surface, and the equilibrium chemical composition of the Al, Si and Co within the mesoporous γ-Al_2O_3 layer was determined as Al:Si:Co = 85:10:5.

(2) XRD, HRTEM and HAADF-STEM analyses revealed that the Co-doped SiO_2/γ-Al_2O_3 composite powder sample with the equilibrium composition of Al:Si:Co = 85:10:5 kept its amorphous state without crystallization of Co oxides after H_2 treatment at 500 °C.

(3) In-situ XANES spectroscopic analyses during the 500 °C-heat treatment under H_2 flow and subsequent cooling to RT under Ar flow exhibited reversible redox properties of Co cation in the Co-doped SiO_2/γ-Al_2O_3 composite powder sample.

(4) XPS and DRIFT spectroscopic analyses and cyclic TPR/TPD measurements concluded the reversible Co(III)/Co(II) redox reactions were associated with OH formation (hydrogenation)-deformation (dehydrogenation) within amorphous aluminosilicate, which was governed by the H_2 partial pressure at 250 to 500 °C.

(5) The Co(III) cations in the present composite samples formed via the Fenton reaction in the presence of H_2O_2 during the sample syntheses.

(6) Gas permeation measurements for the γ-Al_2O_3/Co-doped SiO_2/γ-Al_2O_3 layered composite membrane under the cyclic He-H_2-He flow suggested that a H_2-triggered chemical valve property: micropores under He flow (closure) and mesopores under H_2 flow (open), which could be explained by the reversible redox reactions of Co(III)/(II) associated with bond cleavage (hydrogenation)-regeneration (dehydrogenation) of the Si-O-Al amorphous network formed in-situ at the hetero interface of the Co-doped SiO_2/γ-Al_2O_3.

The observed H_2-triggered chemical valve response needs a long time to function, especially for closure that takes approximately 8 h at 500 °C under Ar flow. The relations between the relative amount of Co(III) in the Si-O-Al amorphous network, recyclability of the redox reactions and the valve response remain as a future subject.

References

[1] C. Estournès, T. Lutz and J. L. Guille, Reduction of nickel in soda-lime-silicate glass by hydrogen, *J. Non. Cryst. Solids*, 1996, **197**, 192–196.

[2] W. D. Johnston and A. J. Chelko, Reduction of Ions in Glass by Hydrogen, *J. Am. Ceram. Soc.*, 1970, **53**, 295–301.

[3] M. M. Smedskjaer, J. Deubener and Y. Yue, Inward cationic diffusion and formation of silica-rich surface nanolayer of glass, *Chem. Mater.*, 2009, **21**, 1242–1247.

[4] A. Chahadih, H. El Hamzaoui, O. Cristini, L. Bigot, R. Bernard, C. Kinowski, M.

Bouazaoui and B. Capoen, H_2-induced copper and silver nanoparticle precipitation inside sol-gel silica optical fiber preforms, *Nanoscale Res. Lett.*, 2012, **7**, 2–7.

[5] S. A. Bates, A. A. Verma, C. Paolucci, A. A. Parekh, T. Anggara, A. Yezerets, W. F. Schneider, J. T. Miller, W. N. Delgass and F. H. Ribeiro, Identification of the active Cu site in standard selective catalytic reduction with ammonia on Cu-SSZ-13, *J. Catal.*, 2014, **312**, 87–97.

[6] M. Nogami, Reduction mechanism for Eu ions in Al_2O_3-containing glasses by heat treatment in H_2 gas, *J. Phys. Chem. B*, 2015, **119**, 1778–1784.

[7] P. T. M. Chau, N. T. Q. Hai, V. X. Quang, H. Van Tuyen and M. Nogami, Control Valence and Luminescence Properties of Cerium Ions in Al_2O_3-SiO_2 Glasses Prepared by Sol–Gel Method, *J. Electron. Mater.*, 2019, **48**, 6972–6977.

[8] H. Van Tuyen, T. Nonaka, K. Yamanaka, P. M. Chau, N. T. Quy Hai, V. X. Quang and M. Nogami, Fluorescence properties of valence-controlled Eu^{2+} and Mn^{2+} ions in aluminosilicate glasses, *J. Lumin.*, 2017, **184**, 83–88.

[9] H. Van Tuyen, M. Nogami and L. X. Hung, Reduction of Sm^{3+} and Eu^{3+} ions-co-doped Al_2O_3–SiO_2 glasses and photoluminescence properties, *Opt. Mater. (Amst).*, 2020, **100**, 109639.

[10] P. T. M. Chau, N. T. Q. Hai, V. X. Quang, H. Van Tuyen and M. Nogami, Control Valence and Luminescence Properties of Cerium Ions in Al_2O_3-SiO_2 Glasses Prepared by Sol–Gel Method, *J. Electron. Mater.*, 2019, **48**, 6972–6977.

[11] M. Kubo, M. Kojima, R. Mano, Y. Daiko, S. Honda and Y. Iwamoto, A hydrostable mesoporous γ-Al_2O_3 membrane modified with Si–C–H organic-inorganic hybrid derived from polycarbosilane, *J. Memb. Sci.*, 2020, **598**, 117799.

[12] K.S.W. Sing, Reporting physisorption data for gas/solid systems with special reference to the determination of surface area and porosity (Recommendations 1984). *Pure Appl. Chem.*,1985, **57**, 603–619.

[13] E. P. Barrett, L. G. Joyner and P. P. Halenda, The Determination of Pore Volume and Area Distributions in Porous Substances. I. Computations from Nitrogen Isotherms, *J. Am. Chem. Soc.*, 1951, **73**, 373–380.

[14] C. Eric and K. Rideal, Permeation, diffusion and solution of gases in organic polymers., 1939, **35**, 628–643.

[15] Y. Iwamoto, K. Sato, T. Kato, T. Inada and Y. Kubo, A hydrogen-permselective amorphous silica membrane derived from polysilazane, *J. Eur. Ceram. Soc.*, 2005, **25**,

257–264.

[16] T. Inada, N. Uno, T. Kato and Y. Iwamoto, Meso-Porous Alumina Capillary Tube as a Support for High-Temperature Gas Separation Membranes by Novel Pulse Sequential Anodic Oxidation Technique, *J. Mater. Res.*, 2005, **20**, 114–120.

[17] B. Ravel and M. Newville, ATHENA, ARTEMIS, HEPHAESTUS: Data analysis for X-ray absorption spectroscopy using IFEFFIT, *J. Synchrotron Radiat.*, 2005, **12**, 537–541.

[18] C. R. Miller, D. K. Wang, S. Smart and J. C. Diniz da Costa, Reversible Redox Effect on Gas Permeation of Cobalt Doped Ethoxy Polysiloxane (ES40) Membranes, *Sci. Rep.*, 2013, **3**, 1648.

[19] N. S. Barrow, A. Scullard and N. Collis, Surface Selective 1H and 27Al MAS NMR Observations of Strontium Oxide Doped γ-Alumina Surface binding sites of strontium oxide on γ-alumina identifi ed for the fi rst time, *Johnson Matthey Technol. Rev.*, 2016, **60**, 90–97.

[20] R. W. Silverstein and G. C. Bassler, Spectrometric identification of organic compounds, *J. Chem. Educ.*, 1962, **39**, 546–553.

[21] Z. Mouline, K. Asai, Y. Daiko, S. Honda, S. Bernard and Y. Iwamoto, Amine-functionalized polycarbosilane hybrids for CO_2-selective membranes, *J. Eur. Ceram. Soc.*, 2017, **37**, 5213–5221.

[22] K. Chakarova, N. Drenchev, M. Mihaylov, P. Nikolov and K. Hadjiivanov, OH/OD isotopic shift factors of isolated and H-bonded surface silanol groups, *J. Phys. Chem. C*, 2013, **117**, 5242–5248.

[23] B. A. F. Kengne, A. M. Alayat, G. Luo, A. G. McDonald, J. Brown, H. Smotherman and D. N. McIlroy, Preparation, surface characterization and performance of a Fischer-Tropsch catalyst of cobalt supported on silica nanosprings, *Appl. Surf. Sci.*, 2015, **359**, 508–514.

[24] S. Tada, S. Ando, T. Asaka, Y. Daiko, S. Honda, S. Bernard and Y. Iwamoto, Hydrogen transport property of polymer-derived cobalt cation-doped amorphous silica, *Inorg. Chem. Front.*, 2021, **8**, 90–99.

[25] H. J. H. Fenton, LXXIII.—Oxidation of tartaric acid in presence of iron, *J. Chem. Soc., Trans.*, 1894, **65**, 899–910.

[26] A. Puppo and B. Halliwell, Formation of hydroxyl radicals from hydrogen peroxide in the presence of iron. Is haemoglobin a biological Fenton reagent?, *Biochem. J.*, 1988, **249**, 185–190.

[27] S. K. Ling, S. Wang and Y. Peng, Oxidative degradation of dyes in water using Co^{2+}/H_2O_2 and Co^{2+}/peroxymonosulfate, *J. Hazard. Mater.*, 2010, **178**, 385–389.

[28] D.W. Breck, Zeolite Molecular Sieves: Structure, Chemistry, and Use; JohnWiley & Sons: New York, NY, USA,1974; pp. 634–636. ISBN 978-0471099857.

[29] T. Yoshioka, T. Tsuru and M. Asaeda, Molecular dynamics study of gas permeation through amorphous silica network and inter-particle pores on microporous silica membranes, *Mol. Phys.*, 2004, **102**, 191–202.

[30] T. Yoshioka, M. Kanezashi and T. Tsuru, Micropore size estimation on gas separation membranes: A study in experimental and molecular dynamics, *AIChE J.*, 2013, **59**, 2179–2194.

[31] K. Malek and M.-O. Coppens, Knudsen self- and Fickian diffusion in rough nanoporous media, *J. Chem. Phys.*, 2003, **119**, 2801–2811.

Chapter 5

Novel hydrogen chemisorption properties of amorphous ceramic compounds consisting of p-block elements: exploring Lewis acid-base Al–N pair site formed in-situ within polymer-derived silicon-aluminum-nitrogen-based system

5.1 Introduction

This chapter describes a first demonstration of unique hydrogen chemisorption properties on Lewis acid-base Al–N pair site formed in-situ within metal-free polymer-derived ceramics based on the silicon-aluminum-nitrogen-based system.

The behavior of molecular hydrogen (H_2) on solid surface covers fundamental surface phenomena such as adsorption, diffusion, transformation, and desorption. In the simplest case, therefore, the main studies demonstrated the interactions of H_2 with solid surfaces in many chemical processes such as catalytic hydrogenation [1-4].

For decades, a major system known to react with H_2 is transition metals (TMs) [1] because of their electronic properties which allow a H_2 molecule to easily adsorb and dissociate onto the metallic surface. The TMs have partially occupied *d*-orbitals, which can accept σ electrons of H_2, while donating the *d*-electrons to σ^* antibonding orbital of H_2. Consequently, the H–H bond is weakened and cleaved—the so called homolytic dissociation of H_2. This paradigm shifted in 2006 [5,6], when a nonmetallic system was discovered to reversibly dissociate H_2 across Lewis acidic boron and Lewis basic phosphorous sites. Thereafter, similar reactions were reported as a system called "Frustrated Lewis Pairs (FLPs)" that were derived from simple combination of electron donors and acceptors in which steric demands precluded the Lewis acid-base adduct [6]. According to the theoretical study on the PR_3 / $B(C_6F_5)_3$ pair (R = *t*Bu and $C_6H_2Me_3$) [7], the reaction between the FLP and H_2 starts via the polarization of a H_2 molecule induced by coordination of a H_2 molecule along the B–P axis. Molecular H_2 polarization along the FLP occurs in the direction of P→B ($P\cdots H^{\delta+}\cdots H^{\delta-}\cdots B$). The binary polarization effect acts associated with reduction of the repulsion forces on both sides of the H_2 molecule. The electron transfer occurs through simultaneous $P\rightarrow\sigma^*(H_2)$ and $\sigma(H_2)\rightarrow B$ donation in a push-pull manner and implies a progressive weakening of the H–H bond and

following heterolytic H_2 dissociation into a proton (H^+) and a hydride ion (H^-). In addition, as an extreme case of hydrogen chemisorption on inorganic compounds consisting of *p*-block elements, the H_2 dissociation adsorption by III-V nanostructured materials in the form of nanosheet and nanotube have been predicted for novel hydrogen storage materials [8–12]. Indeed, the group III-V of nanostructured materials—an unsaturated electron-deficient group III element (electron acceptor site) and an electron-rich group V element (electron donor site)—can be categorized as Lewis acid-base components. Thus, the heterolytic H_2 dissociation and adsorption occur as the same manner as FLPs case. Especially, nanostructured aluminum nitride (AlN) materials have been suggested mainly theoretically as attractive compounds to offer a specific active site for the polarization of a H_2 molecule on the materials surface and subsequent heterolytic dissociation into H^+/H^- pairs.

Through the PDCs route [13–22], we recently demonstrated [19] the in-situ growth of nanostructured AlN into a robust, protecting silicon carbide (SiC) matrix to form amorphous single-phase Si-Al-C-N ceramics at low temperatures and an AlN/SiC solid solution at high temperatures. By changing the nature of the atmosphere (ammonia instead of nitrogen) and considering the same commercially available poly(vinylmethyl-co-methyl)silazane (Durazane® 1800, silicon nitride precursor) chemically crosslinked with *N,N*-dimethylethylamine alane ($EtNMe_2 \cdot AlH_3$), we have designed a novel amorphous single-phase ceramic based on the Si-Al-N system at low temperatures. This inorganic compound consisting of p-block elements has been characterized in detail. Then, we demonstrate that it displays a reversible H_2 adsorption-desorption properties governed by a possible Lewis acid-base pair site formed in-situ within the amorphous surface network. Thus, the active acid sites of the amorphous surface network were investigated by X-ray photoelectron spectroscopy (XPS) and Infra-Red spectroscopy analyses whereas the H_2 adsorption and desorption behavior on the polymer-derived amorphous SiAlN was investigated by measuring a profile of temperature-programmed desorption of hydrogen (H_2-TPD). The local molecular structure was monitored in detail by ^{27}Al solid-state magic-angle spinning Nuclear Magnetic Resonance (MAS NMR) before and after H_2 treatment. In addition, for further proof of hydrogen chemisorption properties of this ceramic, CO_2-hydrogenation reactions were demonstrated by TPD measurement.

5.2 Experimental procedures

5.2.1 Sample synthesis

A single-source precursor was first synthesized by chemical modification of a commercially available Durazane® 1800, poly(vinylmethyl-co-methyl)silazane (PSZ, Merck KGaA, Darmstadt, Germany) with alane *N,N*-dimethylethylamine ($EtNMe_2 \cdot AlH_3$—ADMEA, 0.5M in toluene, Sigma-Aldrich Japan, Tokyo, Japan). The reaction of PSZ and ADMEA relies on both dehydrocoupling and hydroalumination reactions (Fig. 5-1). For the present investigations, we applied the nominal atomic Al/Si ratio of 0.33 corresponding to a molar ratio between the monomeric units of PSZ and ADMEA. The handling of the chemicals and reagents was performed under an inert atmosphere of pure argon (Ar) using standard Schlenk techniques and vacuum/Ar lines. The PSZ (4 mL, 63 mmol) was dissolved into 16 mL of anhydrous toluene at room temperature followed by cooling down to 0 °C. Then, 42 mL (21 mmol) of ADMEA was added dropwise to the PSZ solution under stirring. When the addition was completed, the temperature was naturally increased up to room temperature and the stirring was kept for 24 h. Then, the solvent was distilled off under vacuum at 60 °C to afford the Al-modified PSZ (Al-PSZ).

The chemical modification was monitored by attenuated total reflection flourier transform

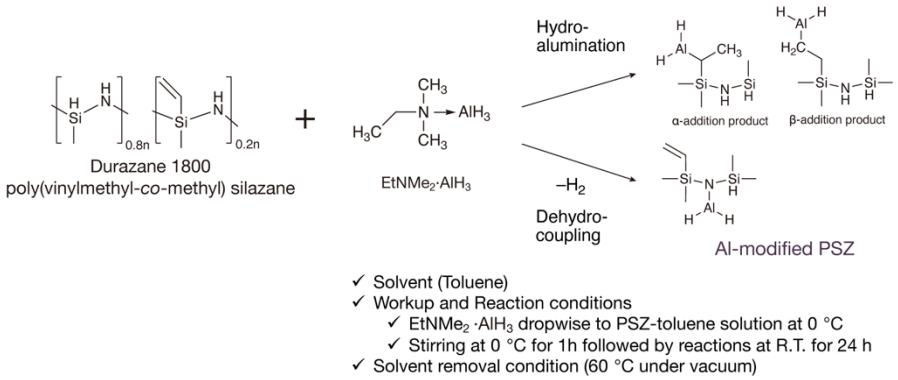

Fig. 5-1 Schematic representation of the synthesis of Al-modified PSZ through PDCs route.

infra-red (ATR-FTIR) spectroscopy using FTIR spectrometer (FT/IR-4200IF, JASCO Corporation, Tokyo, Japan) with attachment of ATR equipment (ATR PRO 550S-S/570S-H, JASCO Corporation, Tokyo, Japan) at a resolution of 4 cm^{-1}. The typical ATR-FTIR spectra of Al-PSZ samples with different Al/Si atomic ratios shows in Fig. 5-2. The FTIR spectra shows that the intensity of the bands corresponding to the C_{sp2}–H band at 3048 and 1402 cm^{-1} slightly

reduces. In parallel, the intensity of the bands assigned to N–H bands at 3381 and 1173 cm^{-1} reduces more significantly. These changes indicate both hydroalumination and dehydrocoupling reaction occur in parallel. FTIR (ATR/cm^{-1}): ν(N–H) = 3350 (m); ν(C_{sp2}–H) = 3048 (w); ν(C_{sp3}–H) = 2950 (m), 2900 (vw); ν(Si–H) = 2130 (vs); ν(Al–H) = 1820 (m); ν(C=C) = 1596 (vw); δ(C–C, vinyl) = 1402 (w); δ(Si–CH_3) = 1250 (vs); δ(Si_2N–H) = 1175 (vs); δ(Si–N) = 840–1020 (vs); and δ(Si–C) = 700–850 (m).

The Al-PSZ was placed in a quartz crucible loaded in a quartz tube in which the

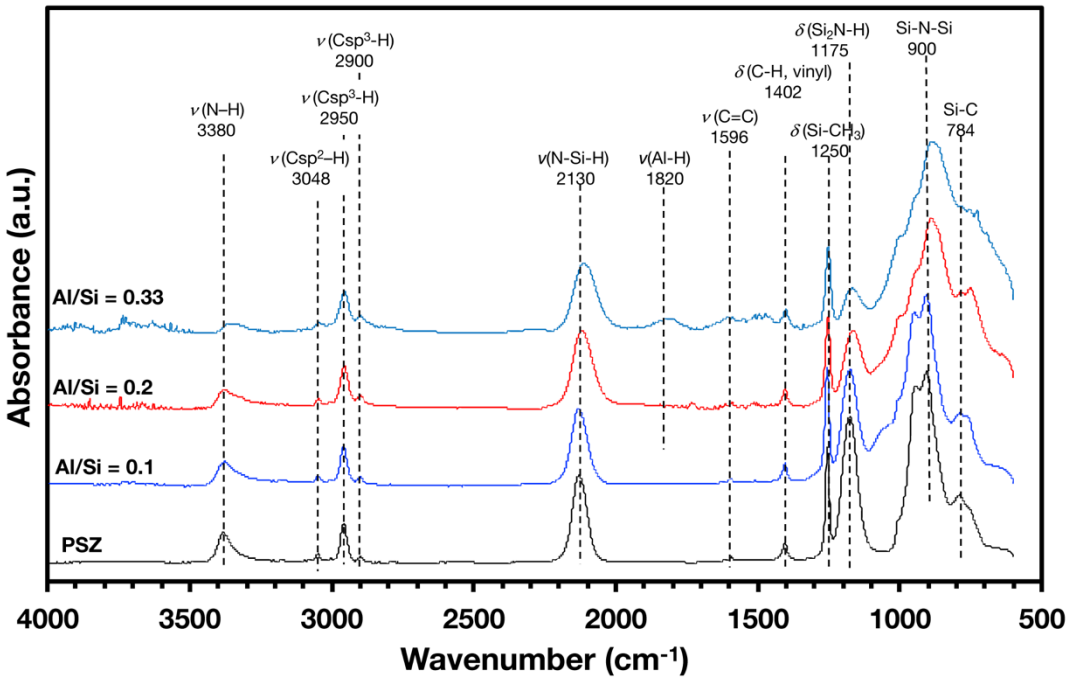

Fig. 5-2 ATR-FT-IR spectra for as-received PSZ and Al-modified PSZ.

atmospheric conditions can be varied between NH_3 and N_2 gasses during pyrolysis. Then, the synthesized single source precursor was pyrolyzed to afford SiAlN ceramic material under flowing NH_3 at 1000 °C for 2 h with a heating rate of 3 °C min^{-1} and subsequently flushed by N_2 and cooled down to room temperature with the same rate of 3 °C min^{-1}. As-pyrolyzed samples were labelled as **SiAlN**. According to the same pyrolysis route, a reference sample free of aluminum and derived from the as-received PSZ was prepared. It was labelled as **SiN**.

5.2.2 Characterizations

Transmission electron microscope (TEM) observations and high-angle annular dark-field-scanning transmission microscope (HAADF-STEM) observations were performed on as-pyrolyzed SiAlN sample using an atomic-resolution analytical microscope, JEOL JEM-

ARM200F (JEOL Ltd., Tokyo, Japan) operated at an accelerating voltage of 200 kV.

Powder X-ray diffraction (XRD) patterns of the pyrolyzed samples were measured on a flat sample stage, using Ni-filtered CuKα radiation (Model X'pert, Philips, Amsterdam, The Netherlands).

Textural properties of pyrolyzed samples were evaluated by measuring N_2 adsorption and desorption isotherms at –196 °C under the relative pressures ranging from 0 to 0.99 (Model Belsorp Max, BEL Japan Inc., Osaka, Japan). The pore size distribution was analyzed by MP [23] and BJH [24] methods. H_2 adsorption-desorption measurement at –193 °C was performed by the same outgassing procedure mentioned for N_2 adsorption-desorption isotherm measurement as described above. As a reference samples, commercially available crystalline AlN (99.9 %, Kojundo Chemical Laboratory Co.,Ltd., Japan,) and zeolite (type HY, HSZ-320HOA, Tosoh Co., Ltd., Tokyo, Japan) were evaluated under the same manner.

Chemical composition of the pyrolyzed samples was determined as follows:

$$\text{wt\%(Si+Al)} = 100\% - \text{wt\%(C)} - \text{wt\%(N)} - \text{wt\%(O)} \qquad (5\text{-}1)$$

The carbon content was analyzed by a carbon analyzer (non-dispersive infrared method, Model CS844, LECO Corporation, Michigan, USA); the oxygen and nitrogen content were measured by an oxygen nitrogen hydrogen analyzer (inert-gas fusion method, Model EMGA-930, HORIBA, Ltd., Kyoto, Japan). The Al/Si ratio was determined by energy dispersive X-ray spectrometry (EDS, Model JSM-6010LA, JEOL Ltd., Tokyo, Japan) mounted on a scanning electron microscope (SEM, Model JSM-6010LA, JEOL Ltd., Tokyo, Japan).

To investigate the chemical bonding-state of the **SiAlN** sample, X-ray photoelectron spectroscopic (XPS) measurements were performed using X-ray Photoelectron Spectrometer (PHI 5000, ULVAC-PHI, Inc., Japan) with an Al Kα X-ray source operated at 14 kV and 14 mA. An alignment on the C 1s peak was performed before survey scans. Deconvolution of each spectrum was performed by Igor pro 7 fitting engine. A program package of X-ray Photoelectron Spectroscopy Tools (XPST) was used in this study. Non-linear curve-fittings were performed using Pseudo-Voigt function [25] with Gauss-Lorentz ratio of 0.3.

To investigate the surface bonding nature of the **SiAlN** sample, diffuse reflectance infrared Fourier transform (DRIFT) spectroscopic analysis was performed. The sample was diluted to be 5 wt% by mixing with nano-diamonds (NDs, IRM 5-12, Tomei Diamond Co.,Ltd, Tokyo, Japan). The diluted sample was filled in an alumina cup and was loaded in the measurement

chamber. DRIFT spectra were recorded at specific temperatures of 150, 250, 300, 350, 400, 450, 500, and 600 °C under flowing Ar. Pyridine adsorption was monitored in-situ for the sample loaded in a potassium bromide (KBr) pellet by measuring FTIR spectra at a resolution of 4 cm^{-1} (Model JASCO FT/IR 4200, JASCO., Tokyo, Japan). The signal-to-noise ratio was improved by averaging 64 scans. The measurement was conducted by using a custom designed IR cell which allowed heat-treatment of the sample in-situ as well as the introduction of various gasses and/or pyridine vapor through a precise valve system. Prior to the measurement, the **SiAlN** sample was maintained at 400 °C under vacuum. Then, the pyridine sorption IR data were recorded after introduction of 10 Torr of pyridine vapor and subsequent removal of the vapor under vacuum at R.T.

5.2.3 Hydrogen adsorption and desorption properties of polymer-derived SiAlN ceramics

To study the H_2 adsorption and desorption properties, temperature-programmed-desorption of hydrogen (H_2-TPD) was performed using a catalyst analyzer (Model BELCAT-A, MicrotracBEL Corp., Osaka, Japan) fixed with a quadrupole mass spectrometer (Model BELMASS, MicrotracBEL Corp., Osaka, Japan). The setup of career-gas flow was 50 cc min^{-1}. The 250 mg of sample was placed in a channel-shape quartz tube with initial diameter of 6 mm. The quartz tube was hermetically connected to the system with the aid of O-rings. Temperature-programmed heating was always managed with a thermocouple in which inserted to the bottom of quartz tube. The **SiAlN** sample was maintained under Ar at 800 °C and subsequently exposed to pure H_2 for 5 min at the specific temperatures (100 °C and 150 °C). After cooling to 50 °C, the gas was changed from H_2 to Ar and maintained for 60 min at 50 °C. TPD-curve was recorded under Ar up to 600 °C with a heating rate of 5 °C min^{-1}.

The local structure around the Al atoms in the **SiAlN** sample before and after H_2 treatment at 150 °C was intensively studied by ^{27}Al solid-state MAS NMR spectroscopic analysis with 600 MHz NMR spectrometer (Model JNM-ECA600II, JEOL Ltd., Tokyo, Japan) operating at a static magnetic field of 14.01 T (155.4 MHz). The diameter of the rotor used in MAS probe was 3.2 mm. All experiments were performed at R.T. with spinning rate of 20 kHz. The typical ^{27}Al resonance was acquired using a single pulse of 90 ° (1.2 *m* s width in this study) with a recycle delay of 2 s. Deconvolution of each spectrum was performed by using Igor pro 7 fitting engine. Non-linear curve-fittings were carried out using Lorentzian-type profile.

For further proof of the presence of chemisorbed hydrogen on the **SiAlN** sample, TPD

measurement was performed on the **SiAlN** sample after exposure to a mixed gas with a 4:1 molar ratio of H_2 and CO_2 or pure CO_2 at 400 °C for 60 min. The post-reaction TPD-MS profile of CO_2 (m/z = 44) was recorded.

5.3 Results and discussion

5.3.1 General characterizations of polymer-derived SiAlN

As shown in the XRD patterns presented in Fig. 5-3, the pyrolysis of the Al-modified PSZ under flowing NH_3 leads to an X-ray amorphous **SiAlN** sample. To investigate the nanostructure and the crystallinity of the **SiAlN** sample in more detail, TEM has been investigated. The High-Resolution TEM (HRTEM) images depicted in Figs. 5-4a and b show contrast between adjacent areas without grain boundaries while the selected area electron diffraction (SAED) as inset in Fig. 5-4b exhibits a typical amorphous halo pattern, which highlights the conclusions made by X-ray diffraction. For further analysis of the observed contrasts shown in Fig. 5-4a, scanning TEM (STEM) imaging has been investigated (Figs. 5-4c and 5-4d). The spot with bright contrast observed in the bright-field (BF) image (Fig. 5-4c) turned to black spots in the dark-field (DF) mode with High Angle Annular Dark Field detector—HAADF (Fig. 1d). Thus, the line scanning result for the selected spot with relatively clear dark contrast in the DF-image (Fig. 5-4d) indicates the presence of voids of approximately 3.3 nm in diameter size as shown Fig. 5-4e.

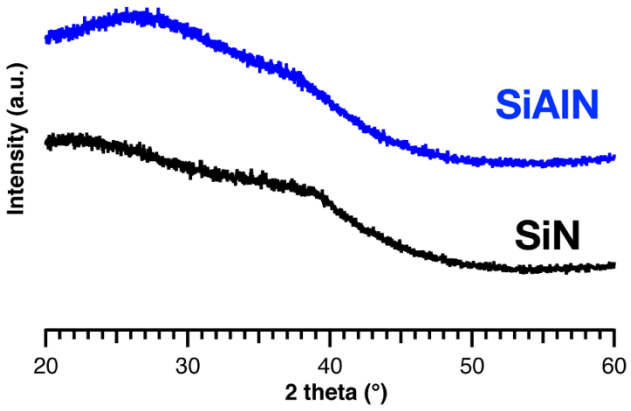

Fig. 5-3 Typical XRD patterns of samples after pyrolysis at 1000 °C under flowing NH_3.

To confirm the presence of pores in the sample, we have investigated porosity at the micro and mesoscopic length scale by N_2 adsorption-desorption isotherm measurement at –196 °C. As reference data, the **SiN** sample and another SiAlN sample which was pyrolyzed under flowing N_2 at 1000 °C (labelled **SiAlN@N_2**) have been investigated for comparison. The results are shown in Figs. 5-5 and 5-6. The **SiAlN** sample at –196 °C exhibited a type I+IV isotherms according to the IUPAC classifications [26, 27], while the **SiN** (Fig. 5-5a) and **SiAlN@N_2** samples (Fig. 5-6a) showed no interaction with N_2. The Brunauer-Emmett-Teller (BET) surface area ($S_{BET}^{N_2}$) of the **SiAlN** sample has been measured to be 165 m^2 g^{-1}. The pore size distribution curve (PSD) in the micropore range characterized by the MP meshod [23] exhibited a peak centered at 1.2 nm (Fig. 5-5b), whereas there was no distinct peak in the

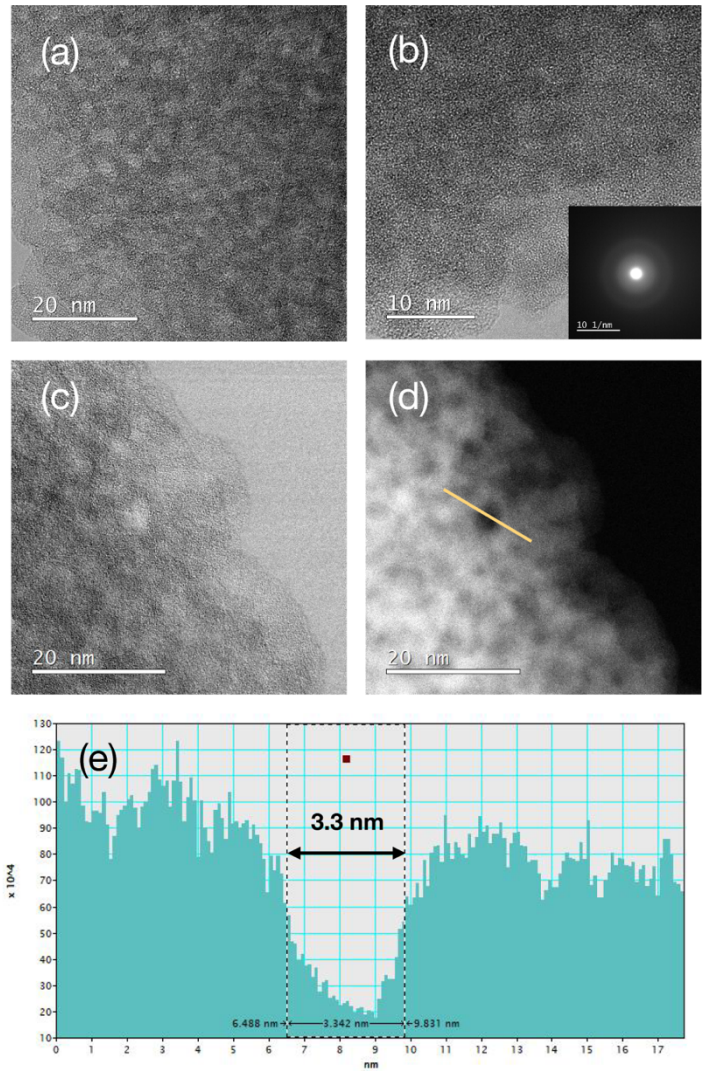

Fig. 5-4 TEM observation of polymer-derived amorphous SiAlN. (a) HRTEM image, (b) High magnification TEM image and the corresponding SAED pattern obtained, (c) BF-STEM image, (d) HAADF-STEM image and (e) Line scanning result for the spot with dark contrast in (d).

mesopore range by the BJH plot [24] although we can identify the existence of a certain porosity with a pore size range of approximately 2 to 4 nm (Fig. 5-5c). This result is consistent with the observed mesopores in the STEM images and highlights that the **SiAlN** sample displays a bimodal porosity which is expected to provide nano-spatial reactions and promote particular chemical reactions of molecules.

It is generally recognized that the formation of micro/mesopores in PDCs is due to the release of gaseous by-products during the polymer-to-ceramic conversion process because of reactions such as transamination, condensation and dehydrocoupling reactions. However, such

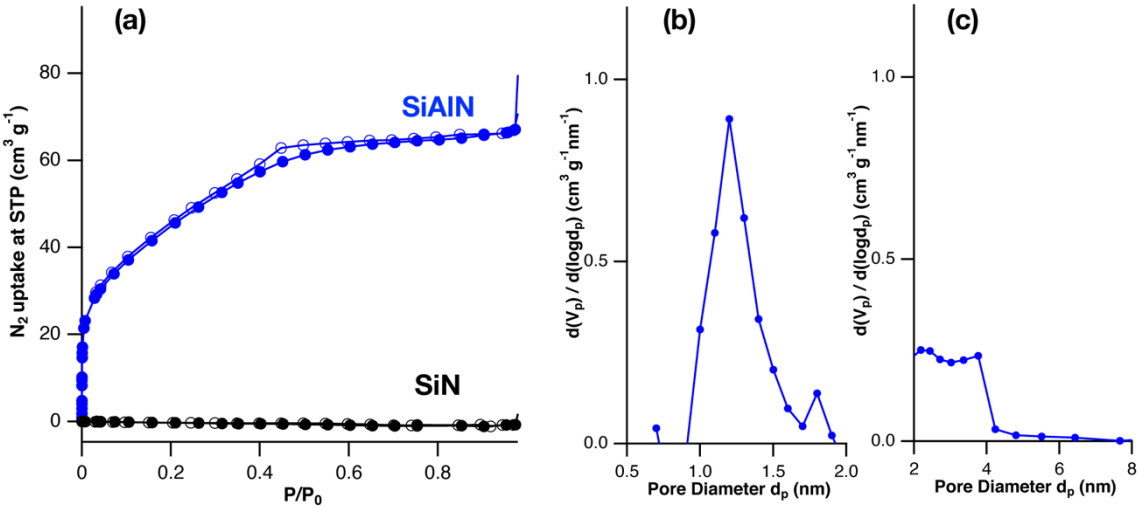

Fig. 5-5 (a) N_2 adsorption-desorption isotherms at –196 °C for the polymer-derived amorphous SiAlN and SiN samples, and pore size distribution curves of the SiAlN sample characterized by (b) MP plot and (c) BJH plot.

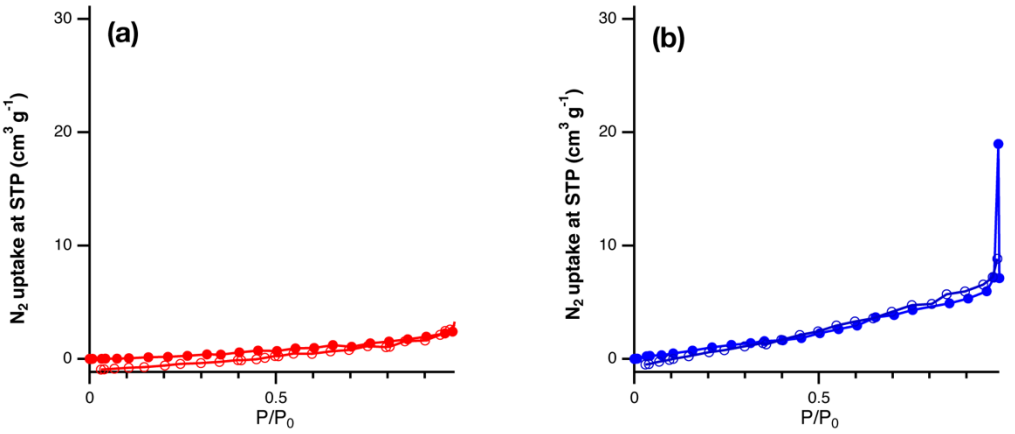

Fig. 5-6 Reference data of N_2 adsorption and desorption isotherms at –196 °C. Polymer-derived SiAlN pyrolyzed (a) at 1000 °C under N_2 and (b) at 700 °C under NH_3.

a micro-/mesoporosity—which is formed in-situ— is in general unstable in the high temperature regime of the polymer-to-ceramic conversion, *i.e.*, 700–800 °C, and therefore collapses[28]. Therefore, the **SiN** sample—formed by pyrolysis of PSZ at 1000 °C under NH_3—is nonporous (Fig. 5-5a). In contrast, it turns out that the micro/mesoporosity stays stable in the **SiAlN** sample in the temperature range 700–1000 °C under flowing NH_3 (Figs. 5-5 and 5-6b) most probably because reactions still occur in the high temperature regime of the polymer-to-ceramic conversion, *e.g.*, reactions of the **SiAlN** samples with hydrogen which is generated by dissociation of NH_3, *i.e.*, partial cleavage of the amorphous network. This is confirmed through TG experiments which have been performed under flowing NH_3-N_2 (60:40 in flow ratio) mixed gas and He. The results are shown in Fig 5-7. A continuous weight loss above 700 °C was identified during the conversion of the Al-modified PSZ under NH_3-N_2 gas flow leading to the **SiAlN** sample whereas no weight loss is identified above 800 °C during the conversion of PSZ into the **SiN** sample (Fig. 5-7a). In addition, such the difference above 800 °C was not observed when the conversions of Al-modified PSZ and PSZ were monitored under He (Fig. 5-7b). Indeed, **SiAlN@N_2** was nonporous (Fig. 5-6a). Therefore, the micro/mesoporosity formation was governed by the reaction with hydrogen derived formed in-situ due to the thermal decomposition of NH_3.

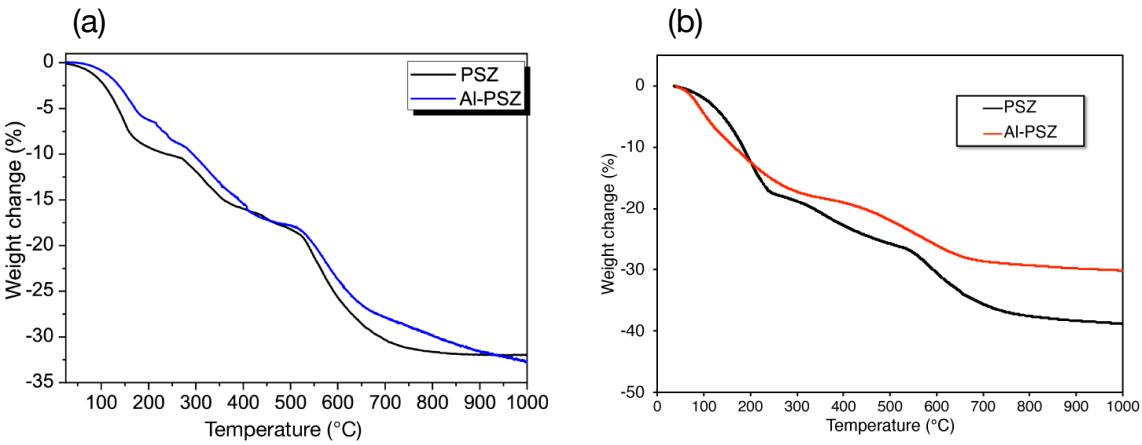

Fig. 5-7 TG-curves of PSZ and Al-PSZ (a) under flowing NH_3-N_2 (60:40 in flow ratio) mixed gas and (b) He.

Table 5-1 lists the chemical composition of the as-pyrolyzed samples. The measured Al/Si atomic ratio of the **SiAlN** sample is 0.35 which is consistent with the nominal atomic Al/Si ratio of 0.33 fixed at the polymer level. In addition, the residual carbon content in the **SiAlN** sample is as low as 0.1 wt% because of the use of ammonia as an atmosphere [29], while the oxygen content is relatively high (9.0 wt%) most probably because of the general procedure of elemental analyses in air for a few minutes.

Table 5-1 Chemical composition of 1000 °C-pyrolyzed samples.

Name	Composition (wt%)					Composition (at%)
	EDS (Al/Si ratio)		Elemental analysis (wt%)			Atomic ratio to Si
	Si	Al	C	N	(O)	
SiN	65.0	0	1.6	32.5	0.9	$Si_1C_{0.06}N_{1.00}$ ($O_{0.02}$)
SiAlN	51.9	17.3	0.1	21.8	9.0	$Si_1Al_{0.35}N_{0.84}$ ($O_{0.30}$)

The bonding nature at the surface of **SiAlN** sample was assessed by the XPS analysis. The wide scan spectrum of **SiAlN** sample is shown in Fig. 5-8. Besides the intense lines of the constituent elements (N 1s, Si 2p and Al 2p) and unavoidable carbon contaminant, strong line of O 1s is observed. This indicates a certain amount of oxygen is present at the surface of the **SiAlN** sample. Figures 5-9a and 5-9b shows the high-resolution Si 2p and Al 2p peaks, respectively. The deconvolution of the Si 2p spectrum (Fig. 5-9a) yields a major peak at 101.6 eV and a minor peak at 103.2 eV assigned to Si–N and Si–O bonds, respectively [30,31]. The deconvolution of Al 2p spectrum (Fig. 5-9b) also yields two peaks at 73.6 and 74.4 eV assigned to Al–N and Al–O bonds, respectively [32]. However, the relative peak area ratio A_{Al-O}/A_{Al-N} is much higher than that of A_{Si-O}/A_{Si-N} in the Si 2p spectrum as shown in Table 5-2.

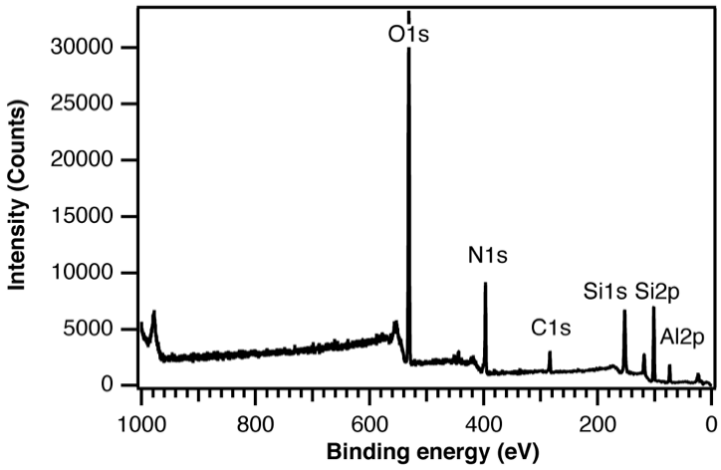

Fig 5-8 Wide scan x-ray photoelectron spectrum of polymer-derived SiAlN.

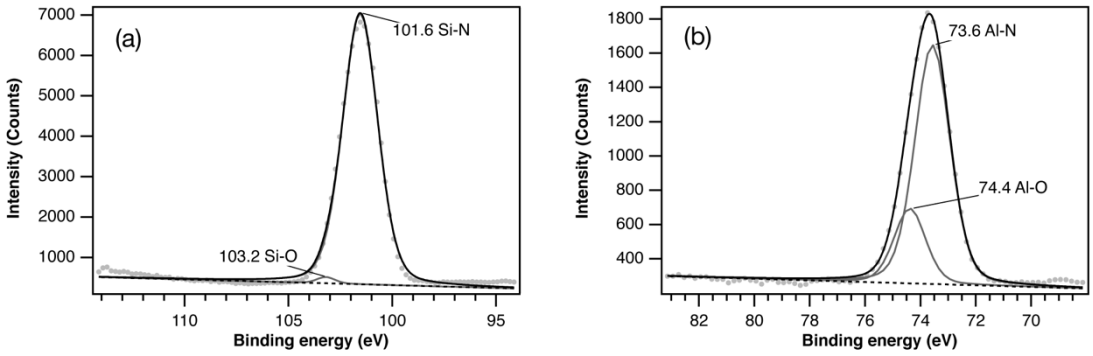

Fig. 5-9 High-resolution X-ray photoelectron spectra of amorphous SiAlN: (a) Si 2p and (b) Al 2p line.

Table 5-2 Summary of XPS characterization for amorphous SiAlN sample. (a) Al 2p and (b) Si 2p.

(a)

Band (Al 2p)	Binding energy (eV)	Area (%)
Al-N	73.5	78.0
Al-O	74.7	22.0

(b)

Band (Si 2p)	Binding energy (eV)	Area (%)
Si-N	73.5	98.8
Si-O	74.7	1.2

To identify the origin of oxygen contaminant in more detail, diffuse reflectance infrared Fourier transform (DRIFT) spectroscopic analysis was performed. Typical DRIFT spectra of the **SiAlN** sample recorded at different temperatures under Ar flow are shown in Fig. 3-10. The **SiAlN** sample exhibits broad absorption bands around 3550 cm^{-1} (νO–H) and 3300 cm^{-1} (νN–H). With increasing temperature from 150 to 600 °C, the absorption band intensity around 3550 cm^{-1} apparently decreases. Accordingly, the absorption band around 3550 cm^{-1} is attributed to O–H groups of chemisorbed water. These results revealed, in addition to the presence of a certain form of porosity, the existence of a certain number of highly reactive Al sites which can be easily occupied with water molecules under ambient moisture.

Based on the high reactivity of Al sites formed in-situ within the amorphous **SiAlN** surface, we used pyridine as a probe molecule for the quantitative analysis of the surface acidity of the **SiAlN** sample by FTIR spectroscopy. Prior to the measurements, the **SiAlN** sample was pre-treated at 400 °C under vacuum to remove the chemisorbed water. The differential spectrum after pyridine adsorption on the pre-treated **SiAlN** sample at RT is presented in Fig. 5-11. It

highlights the characteristic bands attributed to pyridine coordinated on Lewis acid sites (Py-L) at 1629 and 1455 cm^{-1} [33], thus revealing that the highly reactive Al sites in the **SiAlN** sample work as surface Lewis acid sites. As a consequence, we suggested that Al sites located at the surface of the **SiAlN** sample are expected to serve as preferential chemisorption sites for gas molecules such as hydrogen molecule (H_2) as predicted for nanostructured AlN [8–12]. Before the investigation, a pre-treatment was performed on the **SiAlN** sample by heat-treatment under inert atmosphere at sufficiently high temperature of 400-800 °C to allow removing the chemisorbed water from the sample surface. The pre-treated SiAlN sample was labelled as ***PTSiAlN***.

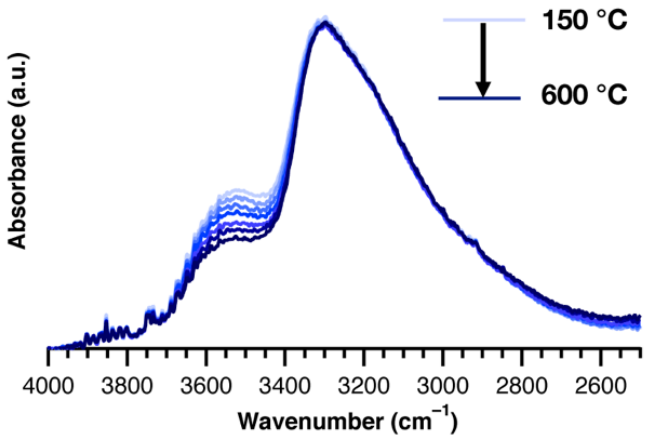

Fig. 5-10 DRIFT spectra for amorphous SiAlN recorded at specific temperatures ranging from 150 to 600 °C under Ar.

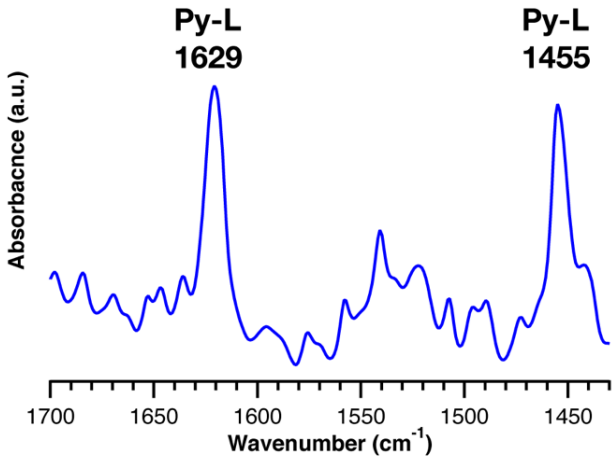

Fig. 5-11 Differential FTIR spectrum of pre-treated SiAlN sample after pyridine adsorption at room temperature.

5.3.2 Hydrogen adsorption and desorption properties of polymer-derived SiAlN

At first, volumetric H_2 adsorption and desorption isotherms at –193 °C of ***PTSiAlN*** sample were recorded over the relative pressures range 0 to 0.99 and were compared with those of commercially available crystalline AlN (measured $S_{BET}^{N_2}$= 3.3 m^2 g^{-1}) and zeolite (type HY, measured $S_{BET}^{N_2}$= 807 m^2 g^{-1}) as shown in Fig. 5-12a. The H_2 adsorption-desorption at –193 °C of the ***PTSiAlN*** sample was fully reversible. In addition, the H_2 uptake at 1 atm increased along their BET surface areas of ***PTSiAlN*** sample and reference samples (Fig. 5-12b). These results indicate that the ***PTSiAlN*** sample exhibits typical H_2 physisorption behavior at –193 °C.

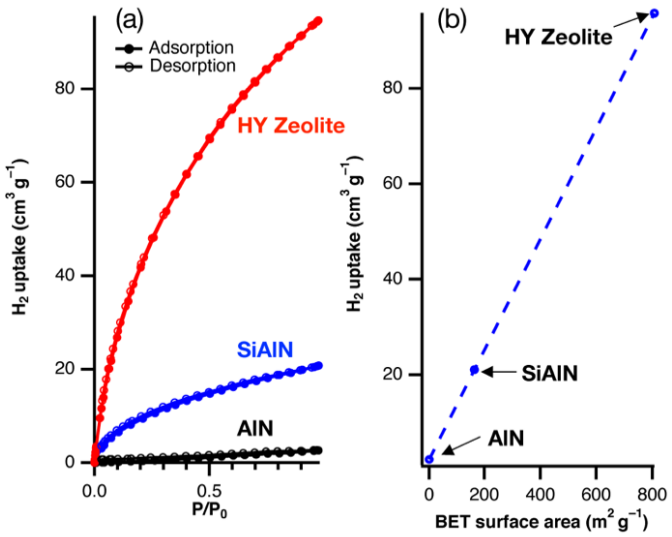

Fig. 5-12 (a) Volumetric H_2 adsorption and desorption isotherms at –193 °C for ***PTSiAlN*** and commercially available crystalline AlN and zeolite samples. (b) The correlation between the H_2 uptake and measured BET surface area.

Then, temperature-programmed-desorption of hydrogen (H_2-TPD) was performed on the ***PTSiAlN*** sample to study the hydrogen chemisorption properties. Prior to the measurement, the ***PTSiAlN*** sample was maintained under Ar at 800 °C and was subsequently exposed to H_2 at specific temperatures (T_{H2} = 100, 150 °C) for 5 min (labelled as ***H_2PTSiAlN*** sample). Typical H_2-TPD profiles of the ***H_2PTSiAlN*** samples are shown in Fig. 5-13a. The H_2-TPD profile after the H_2-treatment at 100 °C (T_{H2} =100 °C) exhibited a single peak at approximately 100 to 350 °C. The peak intensity apparently increased for a H_2-treatment performed at 150 °C (T_{H2} = 150 °C) whereas no peaks were detected without H_2 exposure (***PTSiAlN*** sample, black-line in Fig. 5-13a). Simultaneous in-situ mass analysis during the peak detection (Fig. 5-13b) confirmed the presence of a single desorbed H_2 component. It should be noted that H_2-TPD

profiles of reference samples, *i.e.*, commercial crystalline AlN and HY zeolite samples (Fig. 5-14), show no desorption peak under the same measurement condition (T_{H2} = 150 °C). The activation energy for the H_2 desorption was estimated by the Redhead analysis: the activation energy for desorption of component *i* ($\Delta E_{d,i}$) can be calculated from the slope of the straight line obtained by plotting ln (β / T_p^2) vs. $1/T_p$ where β and T_p are temperature ramping rate and absolute peak temperature, respectively [34,35]. In this study, a T_{H2} = 150 °C was applied, and the H_2-TPD profiles were measured by varying β from 3 to 10 °C min^{-1} (Fig. 5-13c). Both the H_2 desorption peak intensity and T_p increase consistently with β, and the resulting plot successfully provides a straight line with a specific slope to give the $\Delta E_{d,\,H2}$ as 44 kJ mol^{-1} (Fig. 5-13d) which is sufficiently high to be assigned as hydrogen chemisorption.

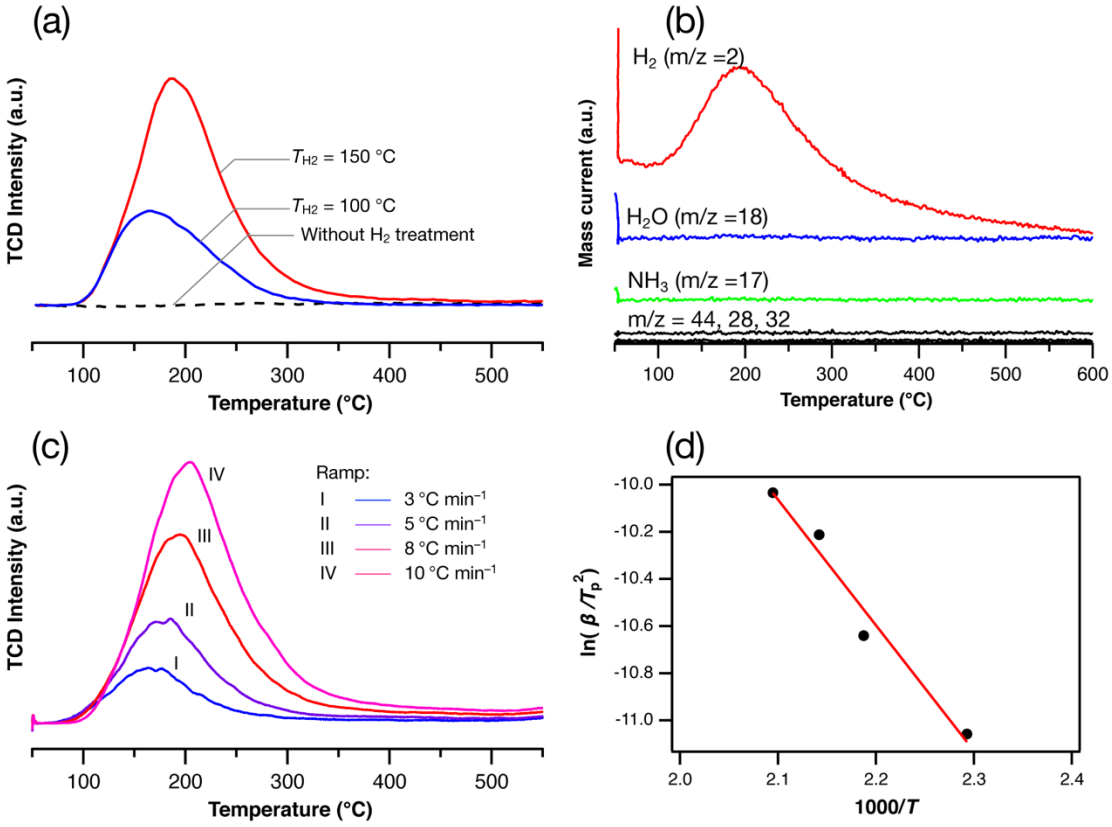

Fig. 5-13 (a) H_2-TPD profiles for ***PTSiAlN*** sample: blue and red solid lines represented H_2 exposure temperature (T_{H2}) of 100 and 150 °C for 5 min, respectively. The dashed line represented TPD profile without H_2 treatment. (b) H_2-TPD Mass profiles for ***PTSiAlN*** after H_2 exposure at 150 °C for 5 min. (c) Variation of the H_2-TPD profiles for the sample after the H_2 exposure at 150 °C by varying temperature ramping rate β from 3 to 10 °C. (d) plot of ln (β / T_{Peak}^2) against $1000/T_{Peak}$ .The activation energy for H_2-desorption was estimated from the slope of the straight line (44 kJ mol^{-1}).

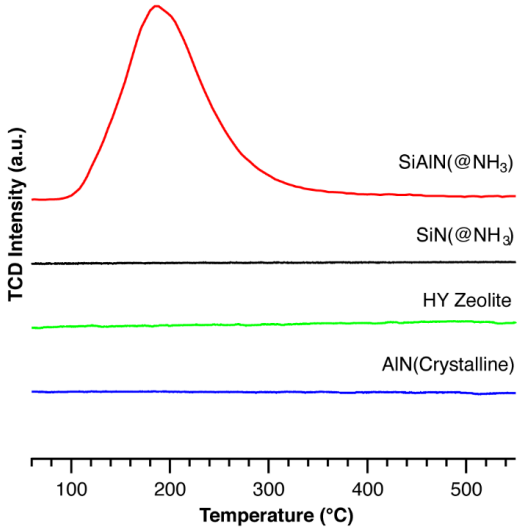

Fig. 5-14 Comparison of H_2-TPD profiles of ***PTSiAlN*** sample with those of reference samples of **SiN** sample, commercially available crystalline AlN and zeolite samples.

To understand such a behavior, the local structure around the Al atoms in the ***PTSiAlN*** sample before (***PTSiAlN***) and after (***H₂PTSiAlN***) H_2 treatment at 150 °C was studied by ^{27}Al solid-state MAS NMR spectroscopy. The ^{27}Al MAS NMR spectra are recorded for the ***PTSiAlN*** sample stepwise after each treatment as follows: the ***PTSiAlN*** sample is exposed to H_2 at 150 °C for 6 h (***H₂PTSiAlN*** sample), and then the ***H₂PTSiAlN*** sample is post heat-treated at 450 °C for 1 h under Ar (labelled as ***H₂PTSiAlNAr***). The ^{27}Al MAS NMR signal in the spectrum of the ***PTSiAlN*** sample is shown in Fig. 5-15a. The deconvolution of the broad ^{27}Al MAS NMR signal provides major signals around 95 and 65 ppm assigned to highly distorted tetrahedral Al (Al_{IV}) units [36,37] represented as $AlN_{4-x}L_x$ (L = N, O and H, x = 1 ~ 3), and five-fold coordinated Al (Al_V) units [36,38,39] represented as $AlN_{5-x}L_x$ (x=1~4), respectively. Minor signals detected around 35 and 6 ppm are assigned to highly distorted octahedral Al (Al_{VI}) units and normal Al_{VI} units, respectively [36]. By comparing the spectra of the ***PTSiAlN*** and ***H₂PTSiAlN*** samples (Fig. 5-15b), the relative intensity of the signal around 65 ppm apparently increases (red signal) compared to the initial one (black signal). Then, after post-treatment under Ar at 450 °C for 1 h (***H₂PTSiAlNAr*** sample), the relative intensity of the blue signal around 65 ppm is observed to decrease in the spectrum of the ***H₂PTSiAlNAr*** sample to an intensity close to the black signal. The increase in the signal intensity around 65 ppm after H_2 treatment at 150 °C (***H₂PTSiAl*** sample) clearly indicates the chemical interaction of the guest molecules with Al. Then, the decrease of the peak around 65 ppm after the post-treatment at 450 °C (***H₂PTSiAlNAr*** sample) indicates the desorption of guest molecules chemisorbed to the Al. This behavior is in good agreement with the H_2-desorption behavior in H_2-TPD profiles

described above. The changes of line-shape in the ^{27}Al MAS NMR spectra and the H_2-TPD profiles suggest that the local structure reorientation reversibly occurs around active Al nuclei, formation and deformation of Al_V units, by adsorption and desorption of H_2 gas molecules, respectively. The formation of Al_V unit in ***H_2PTSiAlN*** indicates the 5-fold coordinated local structure formation is more favorable.

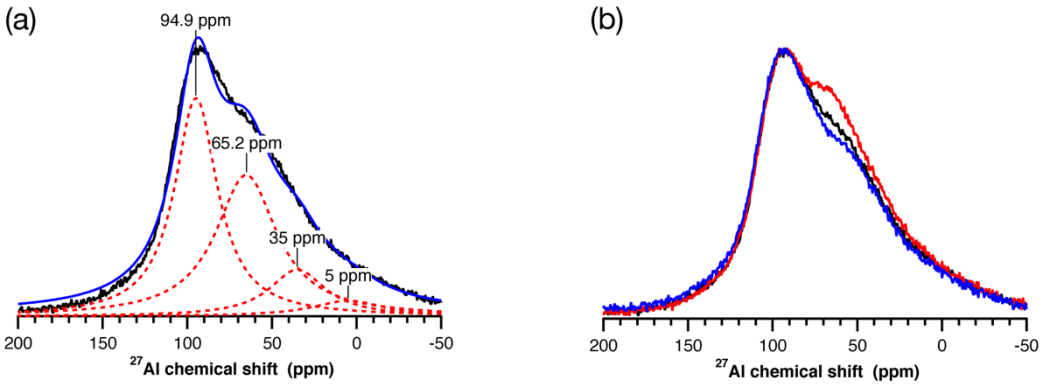

Fig. 5-15 (a) A typical ^{27}Al MAS NMR spectrum for ***PTSiAlN*** sample. The black line represented experimental data, the blue line represented curve-fitting results indicated by Lorentzian curves and red dashed line represented sub-peaks. (b) ^{27}Al MAS NMR spectra recorded for ***PTSiAlN*** stepwise after each treatment as follows: ***PTSiAlN*** sample (Black line) was exposed to H_2 at 150 °C for 6 h (***H_2PTSiAlN*** sample, Red line), and then the ***H_2PTSiAlN*** was post heat-treated at 450 °C for 1 h under Ar (Blue line).

In the case of crystalline AlN, the ^{27}Al MAS NMR spectrum exhibits a sharp signal near 110 ppm[35] due to the highly symmetric AlN_4 unit consisting of three covalent bonds together with one dative bond formed as a Lewis acid-base adduct (sp_3 hybridization). Thus, there is no site for H_2 chemisorption on the crystalline AlN. In addition, the peak intensity of the Al_{IV} units at 95 ppm after H_2 treatment has not changed at all (Fig. 5-15b). Thus, these fully occupied tetrahedral sites detected for the crystalline AlN and ***PTSiAlN*** samples do not serve as H_2 chemisorption sites. Moreover, the signal peak intensity of the Al_{IV} units around 35 and 6 ppm has not changed after the H_2 treatment. These results indicate that the preferential H_2 chemisorption sites of the ***PTSiAlN*** are undetectable by the ^{27}Al MAS NMR spectroscopy.

As reported previously [40], Al sites with a strong distortion of the symmetry are “NMR-invisible”. The preferential H_2 chemisorption sites are thought to be unoccupied H_2-accesible asymmetric sites having the coordination number lower than 4. In addition, the Al sites are intensively distorted compared with the NMR-visible Al_x units (x = IV, V and VI), and thus

preferentially stabilized via the H_2-chemisorption to form Al_V units.

As one possible highly distorted unoccupied site (denoted as Al_{un}), we suggest existence of a pseudo three-coordinated Al site stabilized by the weekly coordinated two N≡ ligands within the SiAlN amorphous network shown in the following proposed reaction scheme for H_2 chemisorption (Fig. 5-16): the starting coordination of Al as monomer precursor is three-coordinated (Fig. 5-16, **1**). After the chemical modification of PSZ with **1** followed by crosslinking of polymer network, the Al in the Al-PSZ is converted to mainly 4-fold coordination to afford mixed $AlN_{4-x}C_x$ (x = 1, 2) tetrahedral units via the hydroalumination as well as dehydrocoupling reactions (Fig. 5-16, **2** as AlN_3C and **3** as AlN_2C_2) [19]. Then, the pyrolysis under NH_3 up to 1000 °C leads to the formation of distorted Al_{IV} units (Fig. 5-16, **4**) accompanied with a certain fraction of unoccupied Al_{un} units (Fig. 5-16, **5**) due to Al–C bond cleavage by the hydrogen formed in-situ above 500 °C under NH_3 flow as discussed above. The fraction of Al_{un} units in ***PTSiAlN*** served as a Lewis acid site to give A_V units via the coordination of nucleophiles such as H_2O or pyridine (sp_2p_z hybridization [41, 42]), which is observed at 65 ppm in Fig. 5-15a. In addition, the H_2 chemisorption at $T > 100$ °C detected by the H_2-TPD analysis was thought to be promoted by Lewis acid-base Al–N pair site in a push-pull manner analogous to that of FLPs as mentioned above: molecular H_2 polarization starts on partially unoccupied p_z orbital of Al_{un} and sp_3 lone pair of nitrogen. This promotes the electron transfer through simultaneous $\sigma(H_2) \rightarrow$Al and N$\rightarrow\sigma^*(H_2)$ and donation in a push-pull manner

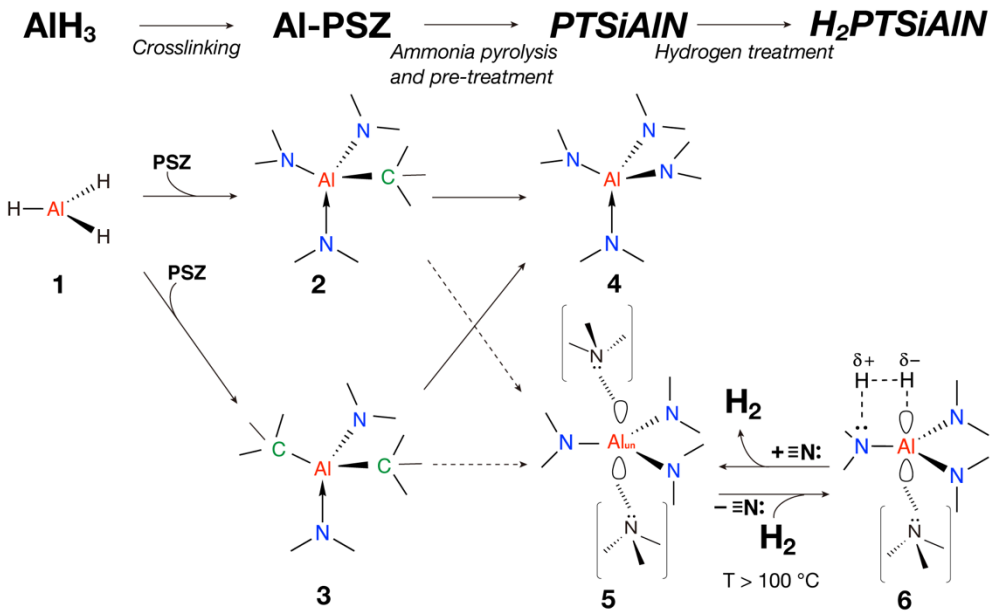

Fig. 5-16 Proposed scheme for the formation of Al_V units by the hydrogenation of Al_{un} units.

and implying a progressive weakening of the H–H bond, which results in the formation of hydrogenated Al unit having 5-fold coordination (Fig. 5-16, **6**).

According to the previous report on the DFT calculations for H_2 adsorption to nanostructured AlN, the energy barrier between the initial state and transition state of H_2 molecule was estimated as 86 kJ mol^{-1}, while that one for the transition from physisorption to chemisorption of H_2 molecule was –10.6 kJ mol^{-1} [12]. The $\Delta E_{d,\,H2}$ of ***H$_2$PTSiAlN*** sample (44 kJ mol^{-1}) in this study is lower than that the one predicted for nanostructured AlN (approximately 97 kJ mol^{-1}). This was thought to be explained by the following difference in the chemical bond formations as discussed above: the nanostructured AlN is predicted to form a Al_{IV} unit (sp_3 hybridization) via the strong Al–H and N–H σ-bond formations [12], whereas the **SiAlN** sample is suggested to form a Al_V unit (sp_2p_z hybridization) *i.e.* formation of slightly elongated and weak hydrogenated structure along the p_z axis as **6** in Fig. 5-16 [41,42].

For further experimental proof of the presence of chemisorbed hydrogen on the **SiAlN** sample, CO_2 hydrogenation reaction on the ***PTSiAlN*** sample was demonstrated by TPD measurement after exposure to a mixed gas with 4:1 molar ratio of H_2 and CO_2 or pure CO_2 at 400 °C. The post-reaction TPD-MS profiles of CO_2 (m/z = 44) are shown in Fig. 5-17. The TPD-MS profile after pure CO_2 treatment exhibits a very weak and broad peak around 100 °C. In contrast, the profile after the H_2-CO_2 mixed gas treatment exhibits a broad but distinct CO_2 desorption peak from 350 to 650 °C. The temperature range above 300 °C found for the CO_2 desorption corresponds to the reported thermal decomposition of formic acid (HCOOH) or formate ($HCOO^-$) to release CO_2 and H_2 [43, 44]. Figure 5-18 shows a possible reaction scheme

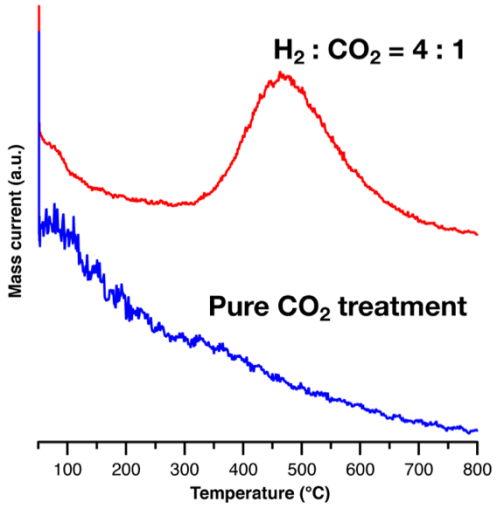

Fig. 5-17 Post reaction TPD-MS profiles of CO_2 (m/z = 44) under Ar flow. The measurement was performed after exposure to a mixed gas with 4:1 molar ratio of H_2 and CO_2 (Red) and pure CO_2 at 400 °C (Blue).

for CO_2 hydrogenation. As discussed above, the ***PTSiAlN*** sample exposure to H_2 leads to the formation of ***H_2PTSiAlN*** (**6**) which can be coordinated with CO_2 via the dipole-induced dipole interaction to give the adduct intermediate H_2 (**7**). Then, CO_2 hydrogenation proceeds to yield HCOO(H) which subsequently decomposes to release CO_2 and H_2 at $T \sim 500$ °C.

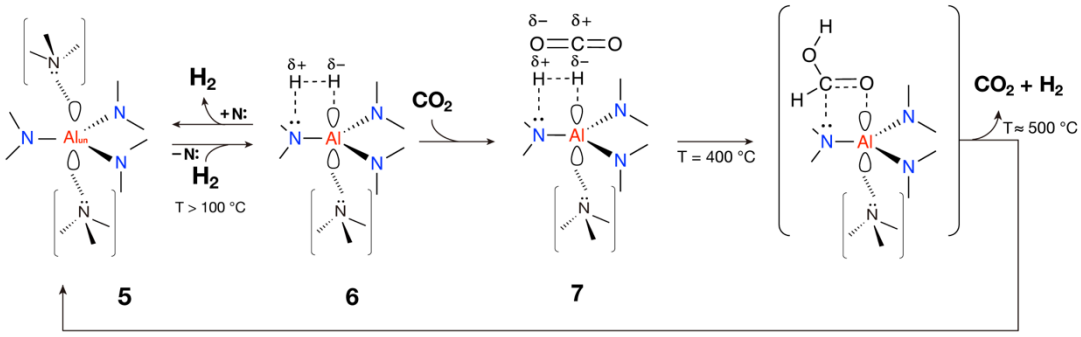

Fig. 5-18 Possible reaction scheme for CO_2 hydrogenation on polymer-derived amorphous SiAlN.

5.4 Conclusions

In this study, an inorganic compound consisting of *p*-block elements, namely silicon, aluminum and nitrogen elements distributed within an amorphous network and displaying novel hydrogen chemisorption properties was synthesized by pyrolysis of an aluminum-modified polysilazane as a ceramic precursor at 1000 °C under flowing NH_3. We experimentally demonstrated the relationship between the H_2 chemisorption properties and structural reorientation of the active Al sites formed in-situ within the polymer-derived amorphous SiAlN surface network. The results can be summarized as follows:

1. HRTEM and STEM analyses and N_2 adsorption-desorption isotherm measurement at –196 °C revealed micro/mesoporosity formation in the SiAlN sample in the high temperature regime of the pyrolysis (700–1000 °C) under NH_3.
2. Chemical composition analyses, DRIFTS and XPS measurements revealed that the incorporation of Al into the amorphous silicon nitride matrix resulted in the formation of Lewis acidic Al characterized by pyridine sorption FTIR.
3. H_2-TPD measurements revealed that the unique reversible H_2 adsorption and desorption properties of the titled compound. The measured activation energy for H_2-desorption ($\Delta E_{d, H2}$) was approximately 44 kJ mol^{-1}, which was sufficiently high to be assigned as hydrogen

chemisorption.

4. The reversible H_2 chemisorption and desorption was successfully identified by ^{27}Al MAS NMR spectroscopic analyses: the results strongly suggested that the local structural reorientation reversibly occurs between undetectable highly distorted Al sites and clearly detectable Al_V units by H_2 adsorption and desorption.
5. The highly distorted Al sites served as a Lewis acid-base Al–N pair site which was suggested as a possible H_2 chemisorption site, and a pseudo three-coordinated Al site was proposed for the one possible H_2 chemisorption site.
6. CO_2 hydrogenation on the amorphous SiAlN sample surface was successfully demonstrated by TPD measurement after sample exposure to a mixed gas with 4:1 ratio of H_2 and CO_2 at 400 °C. The results are clear evidence that H_2 chemisorbed on the Lewis acid-base Al–N pair site.

Although, there is still room for further study on optimizing the hydrogen adsorption-desorption property by controlling several material parameters such as chemical composition and micro/mesoporosity. Moreover, the unique H_2-affinity of the present SiAlN suggests other applications such as a novel non-oxide catalysis support which is recently highlighted for the impressive catalytic activities in hydrogenation of the polymer derived transition metal/Si-based non-oxide ceramic nanocomposites of palladium silicide containing SiCN by Motz and Kempe *et al.* [20], and Ni-SiOC by Wilhelm and Rezwana *et al.* [21], or Pt-TiN/Si_3N_4 nanocomposites which in our very recent study [22] showed enhanced catalytic performance for dehydrogenation of sodium borohydride in water. Therefore, the polymer-derived amorphous SiAlN ceramics are expected to have an impact on catalytic process as a transition or noble metal-free advanced material and significant interest for clean energy applications such as advanced hydrogen production, storage and transportation systems.

References

[1] L. Zhang, M. Zhou, A. Wang and T. Zhang, Selective Hydrogenation over Supported Metal Catalysts: From Nanoparticles to Single Atoms, *Chem. Rev.*, 2020, **120**, 683–733.

[2] F. Zaera, The Surface Chemistry of Metal-Based Hydrogenation Catalysis, *ACS Catal.*, 2017, **7**, 4947–4967.

[3] J. M. Asensio, D. Bouzouita, P. W. N. M. Van Leeuwen and B. Chaudret, σ-H-H, σ-C-H, and σ-Si-H Bond Activation Catalyzed by Metal Nanoparticles, *Chem. Rev.*, 2019, **120**, 1042–1084.

[4] S. Kattel, P. Liu and J. G. Chen, Tuning Selectivity of CO_2 Hydrogenation Reactions at the Metal/Oxide Interface, *J. Am. Chem. Soc.*, 2017, **139**, 9739–9754.

[5] R. M. Kellogg, Reversible metal-free hydrogen activation, *Chemtracts*, 2007, **19**, 152–156.

[6] D. W. Stephan, The broadening reach of frustrated Lewis pair chemistry, *Science*, 2016, **354**, aaf7229.

[7] D. M. Camaioni, B. Ginovska-Pangovska, G. K. Schenter, S. M. Kathmann and T. Autrey, Analysis of the activation and heterolytic dissociation of H2 by frustrated Lewis pairs: NH_3/BX_3 (X = H, F, and Cl), *J. Phys. Chem. A*, 2012, **116**, 7228–7237.

[8] Q. Wang, Q. Sun, P. Jena and Y. Kawazoe, Potential of AlN nanostructures as hydrogen storage materials, *ACS Nano*, 2009, **3**, 621–626.

[9] P. Strak, K. Sakowski, P. Kempisty, I. Grzegory and S. Krukowski, Adsorption of N_2 and H_2 at AlN(0001) Surface: Ab Initio Assessment of the Initial Stage of Ammonia Catalytic Synthesis, *J. Phys. Chem. C*, 2018, **122**, 20301–20311.

[10] S. H. Lim and J. Lin, Ab initio study of the hydrogen chemisorption of single-walled aluminum nitride nanotubes, *Chem. Phys. Lett.*, 2008, **466**, 197–204.

[11] J. Beheshtian, H. Soleymanabadi, M. Kamfiroozi and A. Ahmadi, The H 2 dissociation on the BN, AlN, BP and AlP nanotubes: A comparative study, *J. Mol. Model.*, 2012, **18**, 2343–2348.

[12] M. Moradi and N. Naderi, First principle study of hydrogen storage on the graphene-like aluminum nitride nanosheet, *Struct. Chem.*, 2014, **25**, 1289–1296.

[13] P. Colombo, G. Mera, R. Riedel and G. D. Sorarù, Polymer-derived ceramics: 40 Years of research and innovation in advanced ceramics, *J. Am. Ceram. Soc.*, 2010, **93**, 1805–1837.

[14] S. Bernard, F. Chassagneux, M. P. Berthet, D. Cornu and P. Miele, Crystallinity, crystalline quality, and microstructural ordering in boron nitride fibers, *J. Am. Ceram. Soc.*, 2005, **88**, 1607–1614.

[15] S. Koyama, H. Takeda, Y. Saito, Y. Sugahara and K. Kuroda, Preparation of AlN from poly(ethyliminoalane) via pyrolysis, *J. Mater. Chem.*, 1996, **6**, 1055–1058

[16] Y. Iwamoto, W. Völger, E. Kroke, R. Riedel, T. Saitou and K. Matsunaga, Crystallization Behavior of Amorphous Silicon Carbonitride Ceramics Derived from Organometallic Precursors, *J. Am. Ceram. Soc.*, 2001, **84**, 2170–78

[17] M. C. Bechelany, C. Salameh, A. Viard, L. Guichaoua, F. Rossignol, T. Chartier, S.

Bernard and P. Miele, Preparation of polymer-derived Si–B–C–N monoliths by spark plasma sintering technique, *J. Eur. Ceram. Soc.*, 2015, **35**, 1361–1374.

[18] O. Majoulet, C. Salameh, M. E. Schuster, U. B. Demirci, Y. Sugahara, S. Bernard and P. Miele, Preparation, characterization, and surface modification of periodic mesoporous silicon-aluminum-carbon-nitrogen frameworks, *Chem. Mater.*, 2013, **25**, 3957–3970.

[19] D. Fonblanc, D. Lopez-Ferber, M. Wynn, A. Lale, A. Soleilhavoup, A. Leriche, Y. Iwamoto, F. Rossignol, C. Gervais and S. Bernard, Crosslinking chemistry of poly(vinylmethyl-co-methyl)silazanes toward low-temperature formable preceramic polymers as precursors of functional aluminium-modified Si-C-N ceramics, *Dalton Trans.*, 2018, **47**, 14580–14593.

[20] M. Zaheer, T. Schmalz, G. Motz and R. Kempe, Polymer derived non-oxide ceramics modified with late transition metals, *Chem. Soc. Rev.*, 2012, **41**, 5102.

[21] D. Schumacher, M. Wilhelm and K. Rezwan, Porous SiOC monoliths with catalytic activity by in situ formation of Ni nanoparticles in solution-based freeze casting, *J. Am. Ceram. Soc.*, 2020, **103**, 2991–3001.

[22] A. Lale, M. D. Mallmann, S. Tada, A. Bruma, S. Özkar, R. Kumar, M. Haneda, R. A. Francisco Machado, Y. Iwamoto, U. B. Demirci and S. Bernard, Highly active, robust and reusable micro-/mesoporous TiN/Si_3N_4 nanocomposite-based catalysts for clean energy: Understanding the key role of TiN nanoclusters and amorphous Si_3N_4 matrix in the performance of the catalyst system, *Appl. Catal. B Environ.*, 2020, **272**, 118975.

[23] R. S. Mikhail, S. Brunauer and E. E. Bodor, Investigations of a complete pore structure analysis. I. Analysis of micropores, *J. Colloid Interface Sci.*, 1968, **26**, 45–53.

[24] E. P. Barrett, L. G. Joyner and P. P. Halenda, The Determination of Pore Volume and Area Distributions in Porous Substances. I. Computations from Nitrogen Isotherms, *J. Am. Chem. Soc.*, 1951, **73**, 373–380.

[25] M. Schmid, H. P. Steinrück and J. M. Gottfried, A new asymmetric Pseudo-Voigt function for more efficient fitting of XPS lines, *Surf. Interface Anal.*, 2014, **46**, 505–511.

[26] K. S. W. Sing, D. H. Everett, R. A. W. Haul, L. Moscou, R. A. Pierotti, J. Rouquerol and T. Siemieniewska, Reporting Physisorption Data for Gas/Solid Systems with Special Reference to the Determination of Surface Area and Porosity, *Pure Appl. Chem.*, 1985, **57**, 603–619.

[27] S. Lowell, J. E. Shields, M. A. Thomas and M. Thommes, Springer, Dordrecht, 2004, pp. 129–156.

[28] C. Schitco, M. S. Bazarjani, R. Riedel and A. Gurlo, NH_3-assisted synthesis of microporous silicon oxycarbonitride ceramics from preceramic polymers: A combined N_2 and CO_2 adsorption and small angle X-ray scattering study, *J. Mater. Chem. A*, 2015, **3**, 805–818.

[29] S. Duperrier, C. Gervais, S. Bernard, D. Cornu, F. Babonneau and P. Miele, Controlling the chemistry, morphology and structure of boron nitride-based ceramic fibers through a comprehensive mechanistic study of the reactivity of spinnable polymers with ammonia, *J. Mater. Chem.*, 2006, **16**, 3126–3138.

[30] G. Petzow and R. Sersale, Characterization of Si_3N_4 powders, *Pure Appl. Chem.*, 1987, **59**, 1673–1680.

[31] K. Yamamoto, Y. Koga and S. Fujiwara, Binding Energies of Amorphous CN and SiCN Films on X-Ray Photoelectron Spectroscopy, *Jpn. J. Appl. Phys.*, 2001, **40**, L123–L126.

[32] L. Rosenberger, R. Baird, E. McCullen, G. Auner and G. Shreve, XPS analysis of aluminum nitride films deposited by plasma source molecular beam epitaxy, *Surf. Interface Anal.*, 2008, **40**, 1254–1261.

[33] Y. Li, W. Zhang, L. Zhang, Q. Yang, Z. Wei, Z. Feng and C. Li, Direct Synthesis of Al−SBA-15 Mesoporous Materials via Hydrolysis-Controlled Approach, *J. Phys. Chem. B*, 2004, **108**, 9739–9744.

[34] R. J. Madix, The application of flash desorption spectroscopy to chemical reactions on surfaces: Temperature programmed reaction spectroscopy. *Crit. Rev. Solid State Mater. Sci.*, 1978, **7**, 143–152.

[35] E. Tal-Gutelmacher, D. Eliezer and E. Abramov, Thermal desorption spectroscopy (TDS)-Application in quantitative study of hydrogen evolution and trapping in crystalline and non-crystalline materials, *Mater. Sci. Eng. A*, 2007, **445**–**446**, 625–631.

[36] G. Verdecia, K. L. O'Brien, W. R. Schmidt and T. M. Apple, Aluminum-27 and Silicon-29 Solid-State Nuclear Magnetic Resonance Study of Silicon Carbide/Aluminum Nitride Systems: Effect of Silicon/Aluminum Ratio and Pyrolysis Temperature, *Chem. Mater.*, 1998, **10**, 1003–1009.

[37] Z. Xiong, G. Wu, J. Hu, Y. Liu, P. Chen, W. Luo and J. Wang, Reversible hydrogen storage by a Li-AI-N-H complex, *Adv. Funct. Mater.*, 2007, **17**, 1137–1142.

[38] F. Cheng, S. M. Kelly, F. Lefebvre, S. Clark, R. Supplit and J. S. Bradley, Preparation of a mesoporous silicon aluminium nitride via a non-aqueous sol-gel route, *J. Mater. Chem.*, 2005, **15**, 772–777.

[39] Y. Ren, O. Jiang, H. Zeng, Q. Mao and H. Jiang, Lewis acid-base bifunctional aluminum-salen catalysts: synthesis of cyclic carbonates from carbon dioxide and epoxides, *RSC Adv.*, 2016, **6**, 3243–3249.

[40] J. Haase, D. Freude, T. Fröhlich, G. Himpel, F. Kerbe, E. Lippmaa, H. Pfeifer, P. Sarv, H. Schäfer and B. Seiffert, ^{27}Al magic-angle-spinning NMR studies of aluminum nitride ceramics, *Chem. Phys. Lett.*, 1989, **156**, 328–332.

[41] A. Haaland, Covalent versus Dative Bonds to Main Group Metals, a Useful Distinction, *Angew. Chemie Int. Ed. English*, 1989, **28**, 992–1007.

[42] E. Magnusson, Hypercoordinate Molecules of Second-Row Elements: D Functions or d Orbitals, *J. Am. Chem. Soc.*, 1990, **112**, 7940–7951.

[43] W. L. Nelson and C. J. Engelder, The Thermal Decomposition of Formic Acid, *J. Phys. Chem.*, 1926, **30**, 470–475.

[44] T. Meisel, Z. Halmos, K. Seybold and E. Pungor, The thermal decomposition of alkali metal formates, *J. Therm. Anal.*, 1975, **7**, 73–80.

Chapter 6

Conclusions

This thesis consists of three main parts. Chapter 2: Single-step in-situ formation of Co/Si_3N_4 toward functional metal nanocrystallites/Si-based nitride nanocomposite; Chapters 3 and 4: Clarifying dominant mechanisms for effective enhancement of high-temperature hydrogen permeance through Co-doped amorphous silica-based membranes; and Chapter 5: Exploring novel hydrogen chemisorption properties of amorphous nitride compound consisting of p-block elements, namely Si, Al and N. In these research works, in-situ formation of metal-organic precursor-derived local structures at molecular size to several nanometer-sized composite structures and their functional properties were investigated based on in-situ local structural analyses. Especially, in this thesis, chemical interactions between the detailed structures and hydrogen including surface diffusion, hydrogenation/dehydrogenation (reversible redox reaction), and hydrogen chemisorption were intensively studied and discussed for the Si-based amorphous compounds with tailored chemical composition and the local or nanostructures which were synthesized through molecular precursor design. The results can be summarized as follows:

In Chapter 2, the addition of $CoCl_2$ on PHPS in toluene led to form homogeneously distributed $CoCl_2$ coordinated on PHPS. The low temperature Co nucleation proceeded via in-situ formation of Co_2N by the reaction of $CoCl_2$ with the Si center and NH group of PHPS during pyrolysis under NH_3 at the temperature range of 220–350 °C. The Co started growing at temperature as low as 400 °C via the thermal decomposition of Co_2N. In addition, unusual low-temperature crystallization of the amorphous silicon nitride matrix proceeded at 800 °C.

In Chapter 3, Co(II)-doped amorphous silica with Co/Si atomic ratios ranging from 0.01 to 0.18 were successfully synthesized through PDCs route. The molecular structure of Si–O–Co provided Co(II) induced H-bonded Si–OH. The number of the H-bonded Si–OH has an important effect for enhancing self-diffusion coefficient (D) of deuterium at the sample surface measured by OH/OD conversion. The evaluated D value at 500 °C in this work was 15.6×10^{-15} m^2 s^{-1} which was approximately one order of magnitude higher than the reported D value of sodium aluminosilicate glass. In addition, the polarity of H-bonded OH was consistently increased with the concentration of H-bonded OH. These results can offer an additional hydrogen facilitate transport property at the surface of the micropore channel wall composed

of the Co-doped amorphous silica, i.e., enhancing hydrogen permeance via the surface diffusion mechanism even at the high temperature of 500 °C.

In Chapter 4, the Co-doped SiO_2/γ-Al_2O_3 composites were synthesized by conventional sol–gel method using H_2O_2. The Fenton reaction during the H_2O_2-catalyzed sol–gel process successfully provided Co(III) at Co-doped SiO_2/γ-Al_2O_3 hetero interface. Then, the redox property of the Co(III) partly formed in-situ within the composite samples was intensively studied. In-situ XANES spectroscopic analysis revealed that Co(III) in the Co-doped SiO_2/γ-Al_2O_3 layered composite sample exhibited reversible redox behavior duing heat-treatment at 500 °C under H_2 and subsequently cooling at R.T. under Ar. XPS and DRIFT spectroscopic analyses and cyclic TPR/TPD measurements concluded the reversible Co(III)/Co(II) redox reactions were associated with OH formation (hydrogenation)-deformation (dehydrogenation) within amorphous aluminosilicate by the partial H_2 pressure at 250–350 °C. Moreover, gas permeation measurements for the γ-Al_2O_3/Co-doped SiO_2/γ-Al_2O_3 layered composite membrane exhibited H_2-triggered chemical valve property: mesopores under H_2 flow (open) and micropores under He flow (closure) at 300–500 °C.

In Chapter 5, an inorganic compound consisting of p-block elements, Si, Al and N elements within an amorphous network was synthesized by pyrolysis of an Al-modified polysilazane at 1000 °C under flowing NH_3. Then the relationships between the local structures and hydrogen chemisorption properties were intensively studied. The incorporation of Al was successfully achieved, and the material exhibited single phase ternary Si-Al-N system. Lewis acidic Al sites were formed on micro/mesopore wall surface and characterized by XPS and pyridine sorption FTIR. H_2-TPD measurement revealed that the unique reversible H_2 adsorption and desorption properties. The measured activation energy for the H_2-desorption was approximately 44 kJ mol^{-1} which is sufficiently high to be assigned as chemisorption. The reversible H_2 adsorption and desorption was detected by ^{27}Al MAS NMR spectroscopic analysis: the results strongly suggested that the local structural reorientation reversibly occurs between undetectable highly distorted Al site and clearly detectable 5-fold coordinated Al units by H_2 adsorption and desorption. The highly distorted Al sites served as a Lewis acid-base Al–N pair site which was suggested as a possible H_2 chemisorption site, and a pseudo threecoordinated Al site was proposed as one possible H_2 chemisorption site. In addition, as a further experimental proof of the presence of chemisorbed hydrogen on the SiAlN sample, CO_2 hydrogenation reaction on SiAlN sample was demonstrated by TPD measurement after exposure to a mixed gas with 4:1 molar ratio of H_2 and CO_2 or pure CO_2 at 400 °C.

Acknowledgements

I would like to extend my sincere gratitude to my supervisor Prof. Yuji Iwamoto for giving me the opportunity to research with his group, for his continuous guidance and support for my research work, and for his motivation and enormous knowledge.

I also would like to thank Associate Professor Yusuke Daiko and Assistant Professor Sawao Honda for useful discussions and continuous support for my experiments.

I am grateful to Dr. Samuel Bernard and Prof. Ralf Riedel for their research collaboration with us, and for guiding my technical writing. Moreover, I would like to special thanks to Prof. Masaaki Haneda who helped me to measure materials properties with a special equipment in his lab, and Associate Professor Toru Asaka who performed nanostructural characterizations by using transmission electron microscopy.

My sincere thanks to my colleagues who participated in the research works: Akito Mori, Hideki Mizuno, Shota Saito, Shiori Ando, Junya Iihama, Haruna Takagi, Norifumi Asakuma, whose valuable contributions made those works. I also would like to thank Yuma Matsuda, Sakurako Takazawa for all the fruitful discussions. And last, I thank my family for their unconditional support; my friends Sho Matsuo, Kana Matsuo and Naoki Sakoda for cheering me always.

Shotaro Tada
January 2021

List of publications

List of publications related to this research works:

- S. Tada, M. D. Mallmann, H. Takagi, J. Iihama, N. Asakuma, T. Asaka, Y. Daiko, S. Honda, R. K. Nishihora, R. A. F. Machado, S. Bernard and Y. Iwamoto, Low temperature in-situ formation of cobalt in silicon nitride toward functional nitride nanocomposites, *Chem. Commun.,* (under review).

. . . . . .Chapter 2

- S. Tada, S. Ando, T. Asaka, Y. Daiko, S. Honda, S. Bernard and Y. Iwamoto, Hydrogen transport property of polymer-derived cobalt cation-doped amorphous silica, *Inorg. Chem. Front.*, 2021, **8**, 90–99.

. . . . . .Chapter 3

- S. Tada, S. Saito, A. Mori, H. Mizuno, S. Ando, T. Asaka, Y. Daiko, S. Honda, S. Bernard and Y. Iwamoto, Reversible Redox Property of Co(III) in Amorphous Co-doped SiO_2/γ-Al_2O_3 Layered Composites, *Materials (Basel).*, 2020, **13**, 5345.

. . . . . .Chapter 4

- S. Tada, N. Asakuma, S. Ando, T. Asaka, Y. Daiko, S. Honda, M. Haneda, S. Bernard, R. Riedel and Y. Iwamoto, Novel hydrogen chemisorption properties of amorphous ceramic compounds consisting of p-block elements: exploring Lewis acid-base Al–N pair site formed in-situ within polymer-derived silicon-aluminum-nitrogen-based system, *J. Mater. Chem. A,* 2021, Accepted Manuscript. doi.org/10.1039/D0TA10271G

. . . . . .Chapter 5